Quantitative Measurement of Muscle Oxygen Saturation Using 5-Wavelength Near-Infrared Spectroscopy with Fault Diagnostic

Shuang Ni

A Thesis

in

The Department

of

Electrical and Computer Engineering

Presented in Partial Fulfillment of the Requirements

for the Degree of Master of Applied Science at

Concordia University

Montreal, Quebec, Canada

December 2020

CONCORDIA UNIVERSITY
School of Graduate Studies

This is to certify that the thesis prepared

By: **Shuang Ni**

Entitled: **Quantitative Measurement of Muscle Oxygen Saturation Using 5-Wavelength Near-Infrared Spectroscopy with Fault Diagnostic**

and submitted in partial fulfillment of the requirements for the degree of

Master of Applied Science

complies with the regulations of this University and meets the accepted standards with respect to originality and quality.

Signed by the final examining committee:

_____ Chair and Examiner
Dr. Hassan Rivaz

_____ Examiner
Dr. Emad Shihab

_____ Supervisor
Dr. Jun Cai

Approved _____
Dr. Yousef R. Shayan, Chair of Department of Electrical and Computer Engineering

_____ _____ _____
Dr. Mourad Debbabi, Dean
Gina Cody School of Engineering and Computer Science

Abstract

Quantitative Measurement of Muscle Oxygen Saturation Using 5-Wavelength Near-Infrared Spectroscopy with Fault Diagnostic

Shuang Ni

Regular physical activity can help people improve both physical and mental health. As people pay more attention on their health, fitness has become a popular activity. For individuals who have specific training goals, such as losing fat, gaining weight, and preparing to participate in competitions, it is important to avoid injury during exercise and improve the efficiency of training. Physiological monitoring during exercise, such as heart rate, blood lactate, oxygen uptake, and tissue oxygenation, is helpful for improve the effectiveness and safety of training. Many researchers are devoting their efforts to propose methodology and invent instruments of measuring these metrics. It is well known that heart rate is a commonly used measurement indicator, which can be measured on many fitness equipment and wearable devices. However, heart rate is a global parameter of the trainer's body and cannot represent the training intensity of a specific muscle. Because the muscles are directly affected by the exercise, it is necessary to measure the metrics of muscles to determine whether a specific muscle can tolerate the exercise load or not. If the muscles are overworked, there is a high probability of injury, which must be avoided. Hence, it is imperative to measure local muscles.

Muscle oxygen saturation (SmO_2) is an indicator of the altering between oxygen delivery and consumption in the muscles. The more intense the exercise, the more oxygen is consumed by the muscles. So SmO_2 is a good indicator to assess how fatigued a specific muscle is. In sports science, it is usually measured non-invasively by near-infrared spectroscopy (NIRS). Many instruments were developed by researchers previously based on different NIRS techniques and algorithms. In this thesis, a methodology of measuring absolue value of SmO_2 was proposed for a wearable measurement device with one source and two detectors using 5-wavelength NIRS. The algorithm

of fitting the light attenuation to the Taylor expansion model by bound-constrained non-linear least squares fitting was evaluated with simulated tissues. For *in vivo* measurement, an orthogonalization technique was introduced to reduce the effect of the absorption and scattering of overlying tissues. With comparison and analysis, the measuring SmO_2 values of two designed running procedures were reasonable.

During exercise, the trainer may not always wear the device correctly and the device may move or fall off. And some of the individuals may not exercise as the designed training procedures. So the measured data will be unreliable in these cases. In order to remind users to wear the device properly and to train as the designed procedures, a fault diagnostic method was proposed by machine learning approach in this thesis. With labelling data by its reliability and splitting data into different training status, a support vector machines (SVM) model with Gaussian radial basis function kernel was trained. According to two evaluation curves, ROC curve and cross-validation learning curve, the SVM classifiers in both training states can achieve an accuracy of over 97%. These trained models can be applied as a fault diagnostic for the measurement device.

There is no screen on the device, so the results need to be displayed on a computer or mobile phone. In this thesis, an application that integrated the SmO_2 calculation and fault diagnostic was developed in Matlab App Designer. With this application, after three clicks by users, the SmO_2 curve during training and the absolute values could be displayed in the interface. Since the device didn't have the feature of real-time wireless transmission, a simulation of real-time mode was done to show the possibility of real-time measurement in the future.

Acknowledgments

The work in this thesis was completed with the support and help from many individuals. I would like to extend my thankfulness to all of them.

First, I would like to show my deepest gratitude to my supervisor, Prof. Jun Cai, for his continuous guidance and support in each stage of writing this thesis. His valuable suggestions were very useful and were one of the main reasons that enabled me to pursue my research. Studying under his supervision and working within his group was a golden opportunity for me.

Then, I would also like to thank my research lab NI^{2}Lab colleagues, Gang Li, Xinbo Li, Changyan Yi, Jiefei Ding, Huijin Cao and Shiwei Huang. It was a great pleasure working with them and I appreciate their advices and help. They were a great source of energy and hope to me and NI^{2}Lab was my second family during my study and research. Special thanks to Gang Li for providing me with technical insights and knowledge on signal processing and machine learning. I sincerely hope that he can successfully obtain his Ph.D. degree.

Finally, Special thanks to my parents, Yan Wang and Wenzhi Ni, and my cousins, Kang Wang and Yujia Zhai, for their love, encouragement and support. They were always available in times of need and eased the hardships of my life.

Contents

List of Figures

List of Tables

Chapter 1

Thesis Overview

1.1 Introduction

Exercise provides oxygen and nutrients to tissues and helps the cardiovascular system work more efficiently. The common goal of everyone involved in sports is to improve their muscle strength and enhance endurance. And for athletes, another goal is to enhance their performance in the competition. However, there are two situations, under-reaching and over-training, which often occur that hinder people from achieving their goals. On the one hand, individuals who are under-reaching cannot elicit any physical improvement from their insufficient exercise. Especially for people who have specific training goals, such as losing fat, gaining weight, and preparing to participate in competitions, they cannot achieve their goals with the situation of under-reaching. On the other hand, over-training occurs when individuals exceed their body's ability to recover from strenuous exercise. Usually, it happens when non-elite athletes do high-intensity and high-volume training for long periods, which can lead to inadequate or incomplete recovery. If over-trained for long enough, an individual can completely crash, become chronically ill and fatigued, which is the result that no one wants. Athletes and fitness enthusiasts should try their best to avoid under-reaching and over-training. Therefore, how to work out scientifically and reasonably has become a major concern for trainers.

To prevent these two situations from occurring and to achieve training in the most effective way, not only is it necessary to train harder, but also to train smarter. For the effectiveness and safety of training, physiological monitoring is essential during exercise. There exist several evaluation

metrics to monitor the status during training, such as heart rate, blood lactate, oxygen uptake, and tissue oxygenation. These monitoring have the goal to determine whether the trainer is able to tolerate work out load or not. Trainers need to combine these metrics with professional advice from experts to conduct an effective and safe training.

In the body of a well-trained athlete, the exercised muscle consumes approximately 80% of oxygen. Muscle oxygen saturation (SmO_2) indicates the altering between oxygen delivery and consumption in the muscles. It is a real-time measurement metric of how the muscle utilizes oxygen progressively, which can assist athletes to comprehend how efficiently their muscles are using oxygen during a workout. The non-invasive SmO_2 measurement techniques are usually based on near-infrared spectroscopy (NIRS), an optical strategy for enlightening muscle tissues which penetrate, absorb, reflect, and scatter light coordinated at the tissue. When measuring oxygen saturation, the attenuation of NIR light is mainly caused by the absorption of chromophores and melanin and light scattering. Hemoglobin (Hb) and myoglobin (Mb) are chromophores in human muscle, which are also substances that transport and store oxygen in muscle tissues. Hemoglobin is an iron-containing protein in red blood cells and it can exist in two forms, oxygenated hemoglobin (O_2Hb) and deoxygenated hemoglobin (HHb). By measuring the attenuation of NIR light and excluding the influence of absorption and scattering by other tissues, the ratio of O_2Hb to the total Hb can be calculated, which is the absolute value of SmO_2.

NIRS can be divided into four categories, including continuous-wave spectroscopy(CWS), spatially resolved spectroscopy (SRS), time-resolved spectroscopy (TRS), and phase-modulated spectroscopy (PMS). All of these methods can be used to measure oxygen saturation. There are many instruments in the industry that using NIRS to measure *in vivo* tissue oxygenation. Some of these instruments use PMS and TRS, which are highly accurate but usually expensive and bulky, and are generally used in laboratories and hospitals. The instruments using CWS and SRS can be made into wearable or portable devices, but the accuracy and precision are relatively low.

1.2 Objective of the Research

According to the discussion in the previous section, monitoring during exercise has great benefits for athletes to improve training efficiency and safety. The most common is the monitoring of

heart rate, which is also a metric used by many wearable devices. However, heart rate is a global parameter of the individual's body, which is unable to represent the training intensity of specific muscles. Although blood lactate can provide a very accurate measurement of the effect of training intensity, it is usually measured invasively. Measurement of muscle oxygen saturation can be both representative of the intensity of training in a specific muscle and measured non-invasively.

Even though there are some wearable SmO_2 measuring devices on the market, their prices are very expensive. For example, the price of a Moxy monitor [1] invented by Fortiori Design LLC is more than a thousand Canadian dollars. For sports enthusiasts, few people would spend so much money on a measuring device. Therefore, an affordable measuring device was designed by Getwell Health Technology Co., Ltd. The company designed the hardware [2] but the algorithms of calculating the value of SmO_2 needed to be worked on.

The objective of my research is to design algorithms that suitable for this newly invented device to calculate SmO_2. More specifically, a method to quantitatively measuring SmO_2 using 5-wavelength NIRS with two source-detector distances was proposed in this thesis. Besides, in order to reduce the incorrect guidance to users from the unreliable results, a fault diagnostic methodology was introduced based on data reliability classification and prediction by the machine learning approach. Moreover, since there was no screen on the device, a user-friendly computer application that integrates SmO_2 calculation functions and fault diagnostic was designed using Matlab App Designer and introduced in this thesis.

1.3 Contributions

For the newly invented 5-wavelength near-infrared spectroscopy measurement device, We have customized a SmO_2 calculation algorithm and a fault diagnosis method based on the limited measured data given by Getwell Health Technology Co., Ltd. The main contributions of this thesis are highlighted as follows:

1. For the newly invented SmO_2 measurement device, we applied bound-constrained non-linear least squares fitting to the Taylor extension model to estimate SmO_2 value. Boundaries of each parameter in the least squares fitting were appropriately selected based on their physical meaning.

2. The accuracy of this algorithm was evaluated using 5 wavelengths in three aspects with the simulated attenuation spectra under three light scattering conditions, including non-scattering medium, forearm, and calf.
3. For the *in vivo* measurement, according to the original hexadecimal data read from the device, the light attenuation of five wavelengths at each sampling point was generated.
4. We modified the orthogonalization technique to apply to our measurement device. This technique was applied to the *in vivo* measured light attenuation from both main and auxiliary measurement distances to reduce the absorption and scattering in skin and fat.
5. The measurement algorithm were applied to the orthogonal light attenuation of 5 wavelengths to calculate the values of SmO_2 at each sampling point.
6. The SmO_2 results of 33 *in vivo* tests of different subjects were estimated and analyzed. Some of the results were compared with the results generated from Moxy monitor to prove the rationality of the results.
7. The results of each *in vivo* test was split by training process and labelled by their reliability. A fault diagnostic methodology was introduced based on data reliability classification and prediction by machine learning approach.
8. A user-friendly application was developed by Matlab App Designer, which integrated all algorithms described in this thesis.

1.4 Organization of the Thesis

The rest of this thesis is organized as follows.

In chapter 2, the background knowledge used in this thesis for measuring SmO_2 using NIRS and literature review are presented. First, the theorems and formulas of light absorption and scattering in tissue are given. Then, the biological responses to electromagnetic radiation and the absorption coefficients of water, oxygenated hemoglobin (O_2Hb), and deoxygenated hemoglobin (HHb) are explained. Next, four categories of near-infrared spectra that commonly used to measure tissue oxygenation are presented. Besides, the principles and four metrics of measuring athletes' training in sports science are presented. Finally, the definition of oxygen saturation and existing measurement techniques are introduced.

In chapter 3, a method to quantitatively measuring SmO_2 using 5-wavelength NIRS with two source-detector distances is proposed. First, the structure and principle of the measuring device is described. Then, an algorithm for calculating the absolute value of SmO_2 from the measured data of the main measurement distance is explained in detail. Besides, an accuracy evaluation of this algorithm is done in three aspects with the simulated attenuation spectra under three light scattering conditions, including non-scattering medium, forearm, and calf. Next, an orthogonalization technique is applied to the measured data from two measurement distances to reduce the absorption and scattering in skin and fat. Moreover, two training procedures are introduced to collect the useful data from detectors and the data processing process is explained in a flowchart. Finally, the numerical results of the *in vivo* measurement are shown and explained to prove the usability of the algorithms.

In chapter 4, the content is mainly divided into two parts. Firstly, a fault diagnostic methodology based on data quality classification and prediction by machine learning approach is introduced. Secondly, an application that integrated all these algorithms described in this thesis designed by Matlab App Designer is presented.

In chapter 5, the work of this thesis is concluded and some directions for future research is provided.

Chapter 2

Background and Literature Review

The measurement of muscle oxygen saturation involves knowledge of many disciplines, including biology, clinical medicine, optics, and sports science. To better understand the principles and methods of muscle oxygen saturation measurement, the knowledge of these related subjects should be known.

In this chapter, the background knowledge of many subjects and literature review of tissue oxygen saturation measurement were elaborated. First, the theorems and formulas of light absorption and scattering are presented. Then, the optical properties of tissues related to hemoglobin in human tissues, especially for near-infrared light, is explained in detail. Next, four kinds of near-infrared spectroscopy usually used in clinical medicine are introduced. Besides, the principles of measuring athlete's training in sports science are described. Finally, the definition and existed measurement technologies of tissue oxygen saturation are presented.

2.1 Light Absorption and Light Scattering

For pure absorption without scattering, Beer-Lambert's law [3–5] was introduced to describe the relationship between chromophore concentration and the attenuation. In 1760, Johann Heinrich Lambert proposed the relationship of the absorption of light to the amount of absorbent [5], which is called Lambert's law. Lambert's law states that the light absorbed by each successive layer of the absorbent is independent of the intensity of the radiation, and they all absorb an equal proportion of light [5]. Then, in 1852, the fact that the concentration of an absorbent is proportional to its

absorption of light was investigated by August Beer, which is called Beer's Law [4].

2.1.1 Beer-Lambert's Law

In the case of light transmission through a non-scattering medium, as shown in Fig. 1, the absorption coefficient μ_a can be defined as

$$dI = -\mu_a \, I \, dl \tag{1}$$

where I is the intensity of the light and l is the thickness of the medium. In a homogeneous

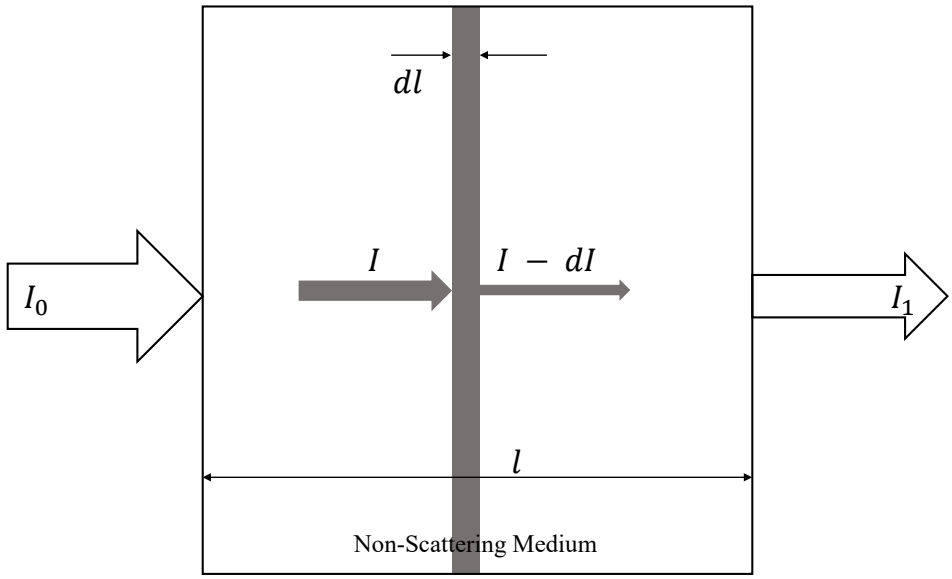

Figure 1: Light transmission through a non-scattering medium

medium, dI is the change in the intensity of light moving along an infinitesimal path dl. Integration over a thickness l (mm), the formula becomes as follows

$$I_1 = I_0 \exp\left(-\mu_a l\right) \tag{2}$$

where I_0 is the incident light intensity. In this case, the thickness l represents the pathlength of the light through the non-scattering medium, which is also equal to the source-detector distance d. The absorption coefficient μ_a can be described as

$$\mu_a = c \cdot \varepsilon \cdot \ln 10 \tag{3}$$

Therefore, equation (2) can also be expressed as a logarithm to base 10 as follows

$$I_1 = I_0 \, 10^{-c \cdot \varepsilon \cdot l} \tag{4}$$

where c is the molar concentration of the compound, and ε is the extinction coefficient and its SI unit is the square metre per mole $(OD \cdot cm^{-1} \cdot mM^{-1})$.

The attenuation spectrum in optical density (OD) units measures the optical attenuation per centimeter of material, which is defined as natural logarithm of the ratio of the incident light intensity to the transmitted light intensity, given by

$$A = -\ln\left(\frac{I_1}{I_0}\right) \tag{5}$$

When measured light attenuation spectrum and ε are expressed as logarithms with base 10, from equations (2), (4) and (5) we can obtain

$$A = \mu_a l = c \cdot \varepsilon \cdot l \cdot \ln 10 \tag{6}$$

2.1.2 Modified Beer-Lambert's Law

The Beer–Lambert's law is only valid in non-scattering media and cannot be applied to biological tissues. In media with scattering, such as tissue, multiple-scattering effects can cause the physical pathlength of light through the tissue to be longer than the geometric distance between the light source and the detector [6]. The differential pathlength has come to be used to refer to this physical pathlength, which can be expressed in equation (7) as a differential pathlength factor (DPF) multiplied by the source-detector separation distance d [7], as shown in the following formula

$$L = \mathrm{DPF} \cdot d \tag{7}$$

In the modified Beer-Lambert's law proposed by D.T. Delpy et al. [7], light scattering was taken into account, as shown in Fig. 2. A term G is added to describe the effect of scattering on the spectrum, which is an unknown geometrically related factor. Therefore, the attenuation spectrum can be expressed as

$$A = -\ln\left(\frac{I_1}{I_0}\right) = L \cdot \mu_a + G = \mathrm{DPF} \cdot d \cdot \mu_a + G \tag{8}$$

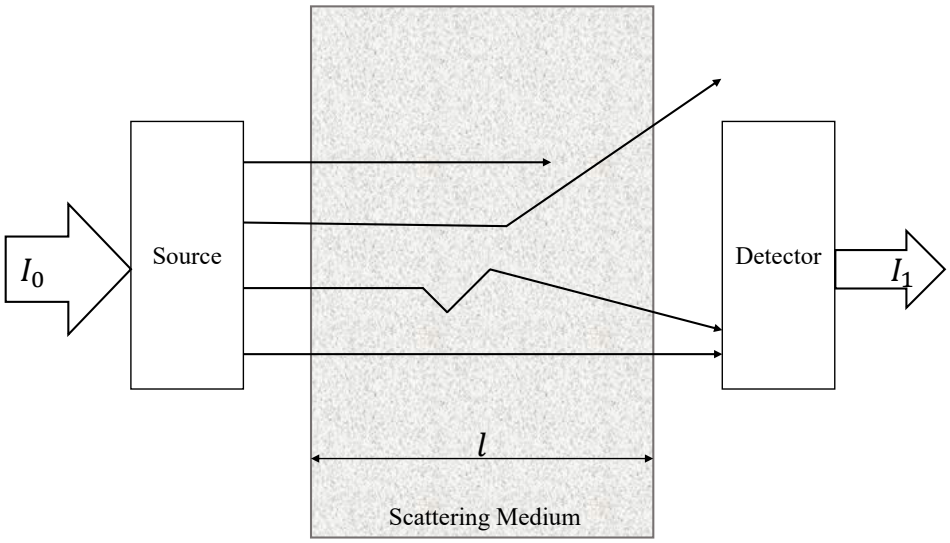

Figure 2: Light transmission through a scattering medium

2.1.3 Light Scattering in Tissue

In tissues, the refractive index mismatches at boundaries causes light scattering. The area that contributes to scattering is called effective cross-section. The scattering coefficient μ_s (mm^{-1}) is expressed as the cross-sectional area (mm^2) per unit volume of the medium (mm^3) [8]. Assuming scattered photons don't return to the incident axis, μ_s can be defined as

$$I_1 = I_0 \exp\left(-\mu_s l\right) \tag{9}$$

Another parameter called reduced scattering coefficient μ_s' is commonly used for *in vivo* measurements, which is defined as

$$\mu_s' = \mu_s \left(1 - g\right) \tag{10}$$

where the parameter g is the anisotropy factor, which can be represented as

$$g = \int_{-1}^{1} \cos\theta f\left(\cos\theta\right) \;\; d\cos\theta \tag{11}$$

When $g = 0$, scattering is isotropic. When $g = 1$, the incident light doesn't scatter in tissues. When $g = -1$, the incident light scatters complete backward to the source. The value of g in biological tissues is $0.69 \leq g \leq 0.99$, which means that forward scattering usually occurs in the tissues [8].

2.2 Optical Properties of Tissue

When measuring *in vivo* tissue by optical techniques, it is important to consider the biological responses to electromagnetic radiation. There are three main reasons for the attenuation of NIR light in tissue: (i) O_2-dependent absorption from chromophores of variable concentration, i.e., hemoglobin (Hb), myoglobin (Mb) (in muscles only), and cytochrome oxidase; (ii) absorption from chromophores of fixed concentration, i.e., skin melanin; (iii) light scattering [9]. Hemoglobin is an iron-containing protein in red blood cells and can exist in two forms, oxygenated hemoglobin (O_2Hb) and deoxygenated hemoglobin (HHb). One mole of HHb combines with four moles of oxygen to form O_2Hb [8].

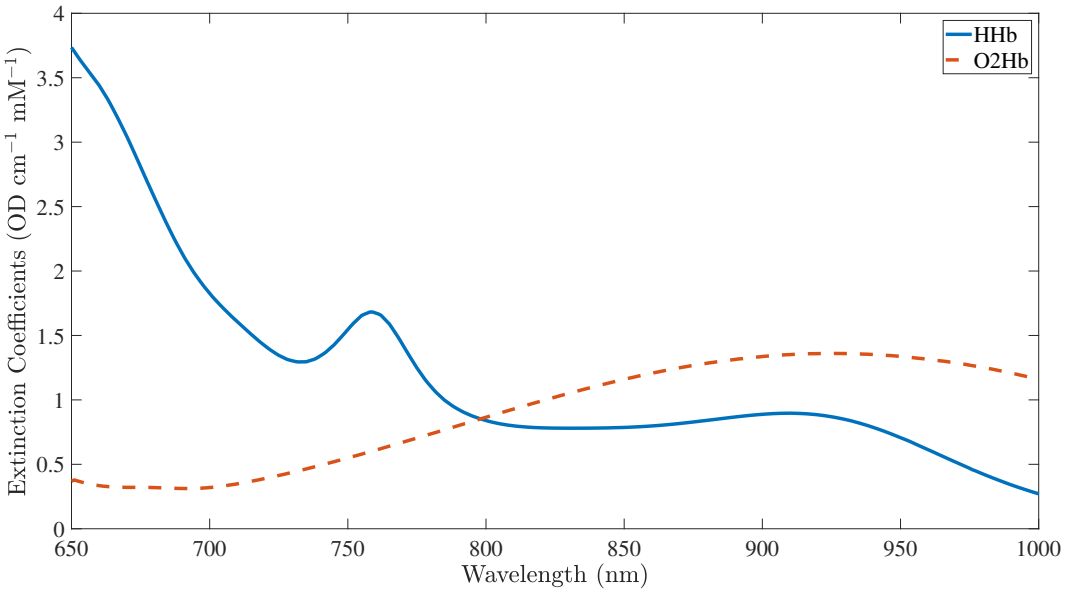

Figure 3: Absorption spectra of O_2Hb and HHb

As early as in the 19th century, continuous light has been used to non-invasively investigate human tissue by transmitting the light through the tissue such as breast and head [10]. In 1860s, Hoppe-Seyler from Germany and Stoke from the United Kingdom described the spectrum of O_2Hb and HHb [11]. The absorption coefficient determines how far light of a particular wavelength can penetrate a material before being absorbed. And it depends on the wavelength of the absorbed light and the material. There is very little light absorption in a medium with a low absorption coefficient, and it will show as transparent to that wavelength if the medium is thin enough. The optical

absorption characteristics of O_2Hb and HHb are different, and the absorption spectra of O_2Hb and HHb [12] are shown in Fig. 3. In this figure, the isosbestic point, which is the intersection of the curves of the two hemoglobins, is at approximately 800 nm.

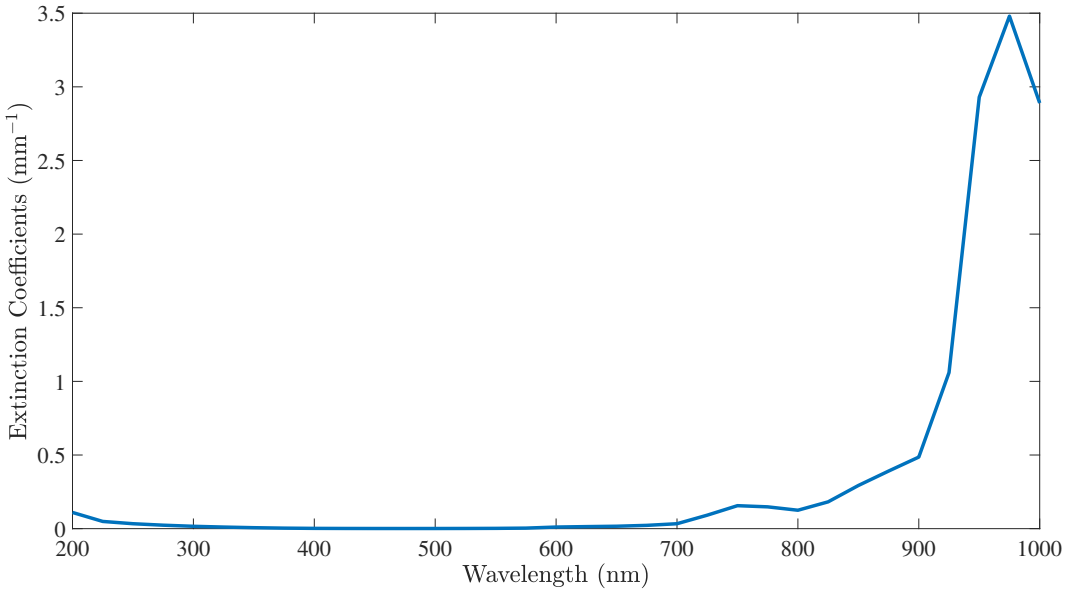

Figure 4: Absorption spectra of water

The absorption spectra of water [13] is shown in Fig. 4. In order to reduce the influence of water absorption, the wavelength with small water extinction coefficient should be selected, which is between about 200 nm and about 950 nm. Taking into account the absorption spectra of main components in tissues, *in vivo* measurements by spectroscopy with wavelengths between 650 nm and 950 nm are especially reasonable.

2.3 Near-Infrared Spectroscopy in Clinical Medicine

With the development of science and technology, near-infrared (NIR) spectroscopy (NIRS) has became a popular technique for a wide range of quantitative and qualitative analysis in various fields, such as agriculture, food, medicine, materials, etc. Across the full electromagnetic spectrum of light, visible light lies in the mid-spectrum range of 400 nanometers (nm) to 700 nm and the NIR light spectrum ranges from 700 nm to 2500 nm. Light below 650 nm is strongly absorbed

by hemoglobin, while light above 950 nm is strongly absorbed by water. In clinical applications of NIRS, the wavelength between 650 nm and 9500 nm are commonly used. For *in vivo* tissue measurement, visible light can only penetrate the tissue no more than 1 centimeters (cm), while NIR light can access the tissue depth up to 8 cm [14]. As a spectroscopic method, NIRS examines the change in absorbance of the electromagnetic spectrum.

In 1932, Nicolai et al. completed the first study on the spectroscopic measurement of *in vivo* tissue, which examined the optical characteristics of hemoglobin [15]. Ten years later, Millikan developed the first practical ear oximeter for aviation [16]. The most important follow-up work in ear oximetry began in 1948 by the laboratory of Earl H. Wood. Millikan's earpiece was modified by Wood et al. to obtain the absolute oxygen saturation of arterial blood [17]. Due to their device are based on many extraneous assumptions, it was not sufficiently stable for continuous monitoring of oxygen saturation. Therefore, their idea was used to manufacture ear oximeters for clinical use for twenty years, until Aoyagi et al. [18] proposed a new instrument named pulse oximetry in 1974, which uses arterial pulsation. This kind of device can accurately measure the oxygen saturation of arterial blood without being affected by factors other than arterial blood. Nowadays, pulse oximetry is widely used in clinical medicine all over the world. Although it is important to measure oxygen saturation of arterial blood to reflect gas exchange occurring in the lungs, measurement of blood oxygenation in the capillaries of each tissue is also desirable.

In NIRS, reflected or transmitted light intensity is usually used for determining the tissue oxygenation. However, it is difficult to detect transmitted light in adult tissues, such as the brain, thigh, calf, forearm, etc., so NIRS using transmitted light is not suitable for clinical measurement. Therefore, reflection light intensity is most commonly used in clinical medicine nowadays.

There are four major categories of NIRS techniques that have been used to measure tissue oxygenation: continuous-wave spectroscopy(CWS), spatially resolved spectroscopy (SRS), time-resolved spectroscopy (TRS), and phase-modulated spectroscopy (PMS).

2.3.1 Continuous-Wave Spectroscopy

The term "continuous wave" refers to a measurement technology based only on the light intensity, regardless of the phase, time, etc. In continuous-wave spectroscopy (CWS), a constant intensity of

light is incident into the tissue, and then the attenuated light signal is measured at a certain distance from the light source, as shown in Fig. 5. Most commonly, in CWS instruments, the source and detector are connected to the tissue using optical fibers, but there are also some devices that use LEDs as light source and photodiode as the detector, which is placed directly on the skin.

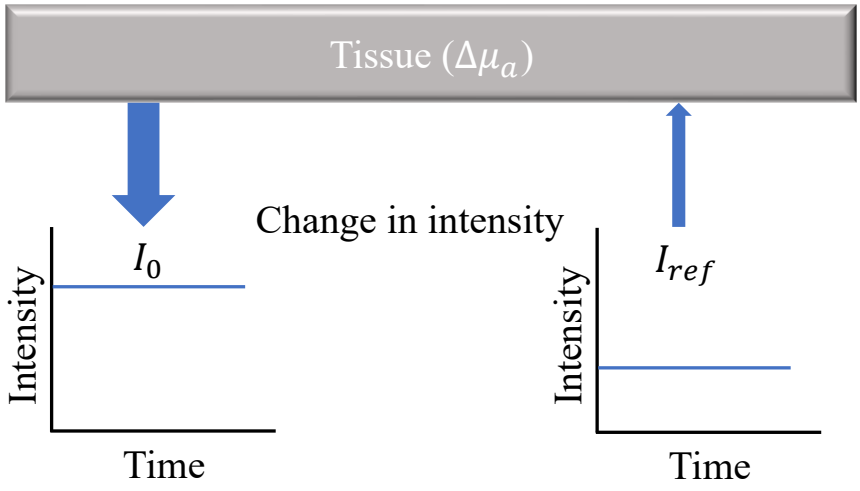

Figure 5: Continuous-Wave Spectroscopy Technique

The change in tissue oxygenation can be determined from the change in absorption coefficients of a tissue. Assuming that the changes in light absorption are mainly due to oxygenation or volume changes in the blood. According to equation (3), the change of absorption coefficient of a tissue under a specific wavelength can be defined as

$$\Delta\mu_a(\lambda) = (\varepsilon_{O_2Hb}(\lambda)\,\Delta c_{O_2Hb} + \varepsilon_{HHb}(\lambda)\,\Delta c_{HHb})\ln(10) \tag{12}$$

where $\varepsilon_{O_2Hb}(\lambda)$ and $\varepsilon_{HHb}(\lambda)$ represent the extinction coefficients of O_2Hb and HHb at wavelength λ, and Δc_{O_2Hb} and Δc_{HHb} are the changes of O_2Hb and HHb concentrations.

In order to get the value of Δc_{O_2Hb} and Δc_{HHb}, $\Delta\mu_a$ should be obtained from measurements at least two wavelengths. A combination of wavelengths between 650 and 950 nm is commonly used by the NIRS techniques. These wavelengths are usually chosen on both side of the isosbestic point of O_2Hb and HHb absorption spectra, which is shown in Fig. 3. The larger the difference between two wavelengths, the easier to obtain the intensity change due to the wavelength, but the change in the optical path length should not be ignored. Assuming that the path lengths of each wavelength

are same, the changes in concentration of O_2Hb and HHb can be expressed as

$$\Delta c_{O_2Hb} = \frac{\varepsilon_{HHb}(\lambda_2)\,\Delta\mu_a(\lambda_1) - \varepsilon_{HHb}(\lambda_1)\,\Delta\mu_a(\lambda_2)}{\varepsilon_{O_2Hb}(\lambda_1)\,\varepsilon_{HHb}(\lambda_2) - \varepsilon_{HHb}(\lambda_1)\,\varepsilon_{O_2Hb}(\lambda_2)} \tag{13}$$

$$\Delta c_{HHb} = -\frac{\varepsilon_{O_2Hb}(\lambda_2)\,\Delta\mu_a(\lambda_1) - \varepsilon_{O_2Hb}(\lambda_1)\,\Delta\mu_a(\lambda_2)}{\varepsilon_{O_2Hb}(\lambda_1)\,\varepsilon_{HHb}(\lambda_2) - \varepsilon_{HHb}(\lambda_1)\,\varepsilon_{O_2Hb}(\lambda_2)} \tag{14}$$

In Continuous-Wave NIRS (CW-NIRS), assuming that the scattering coefficient doesn't change during measurement, the change of attenuation spectrum can be generated from equation (8). Assuming that the parameter G has the same value for all chromophores in the medium, G can be cancelled by using the differential equation. Therefore, the change of attenuation spectrum in optical density (OD) units is defined as

$$\Delta A = -\ln\left(\frac{I_1}{I_0}\right) = L \cdot \Delta\mu_a = \mathrm{DPF} \cdot d \cdot \Delta\mu_a \tag{15}$$

When DPF and source-detector distance are known, $\Delta\mu_a$ can be calculated from this formula because ΔA can be measured by CW-NIRS devices. Although the DPF information of a specific tissue at a specific wavelength could be found in some priori studies, such as Duncan's paper [19], the actual pathlength of light L would never be known.

The CWS technique has advantages that it is very sensitive and it enables a data sampling rate of less than one second. However, it has the disadvantage that it cannot fully determine the optical properties of tissue, such as light absorption and scattering coefficients, and therefore it cannot obtain the absolute value of O_2Hb and HHb [8].

2.3.2 Spatially Resolved Spectroscopy

Spatially resolved spectroscopy (SRS) [20] is an improvement to the original on source-detector device in CW-NIRS technology, as shown in Fig. 6. The estimation precision of attenuation spectrum A can be improved by measuring at multiple distances from the source. In addition, the SRS technology enhances the detection of deeper tissues while reducing the contribution of shallower tissues [21]. Moreover, when measuring tissues with multi-layer by SRS, the light received at shorter distances almost only contains the information of the top layer, such as skin and fat, while at longer distances, both information of the top layer and underlying tissue, such as muscles, is

contained in the collected light. In addition, unlike the TRS (described below), the SRS instrument can process a larger number of photons at the detector, and thus with less noise. Therefore, it is possible to be transported and commercialized.

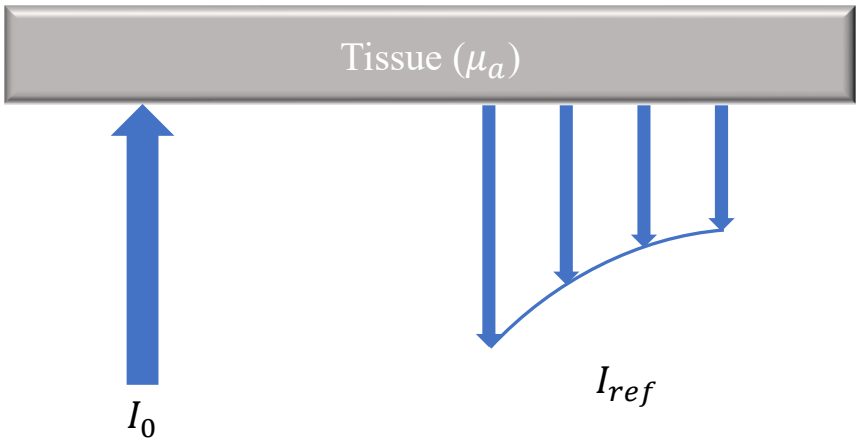

Figure 6: Spatially Resolved Spectroscopy Technique

Spatially resolved NIRS also can't be used to calculate absolute concentrations of chromophores in tissues because the pathlength of light L is unknown. However, the changes in the concentrations of O_2Hb and HHb, relative to the initial baseline value, can be determined by the SRS instrument.

2.3.3 Time-Resolved Spectroscopy

Time-resolved spectroscopy (TRS), as shown in Fig. 7, uses a picosecond pulsed light as incident light and a detection equipment with temporal resolution in the subnanosecond scale to get the reflected light intensity. A recording system that can detect and calculate the delay between pulse transmission and reception is also required in TRS devices. In a TRS device, a single pulse is split into two parts, a part of the laser output is taken directly to the streak camera for time reference, while another part of the beam traverses the tissue [22]. Both the time reference and the signals reflecting or penetrating the tissue are recorded simultaneously. Due to scattering in the tissues, the received signal is delayed. Therefore, the time difference between the light entering and exiting the tissue can be measured, which can be used for calculating DPF by

$$\mathrm{DPF} = \frac{L}{d} = \frac{c_v t}{d} n_t \tag{16}$$

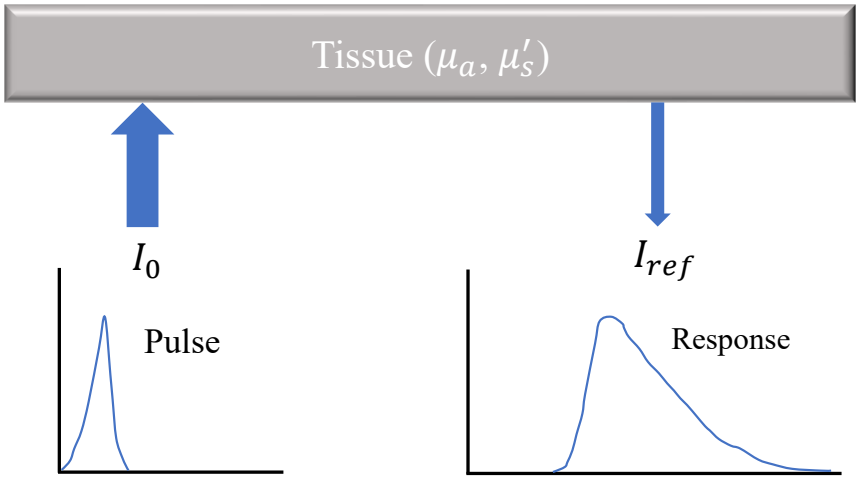

Figure 7: Time-Resolved Spectroscopy Technique

where L represents the differential pathlength, d is the source-detector distance, c_v means the light speed in vacuum, and n_t is the refractive index of the tissue, which is assumed to be 1.4, an empirical value [23].

TRS technology is considered to have the highest accuracy in the quantitative distinction between absorption and scattering, and is considered to be the best technique for measuring the optical properties of tissues [24]. This technique can be used to determine the absorption coefficient, the reduced scattering coefficient of tissues, etc. Since the actual pathlength of light in tissue can be determined by TRS, it is possible to generate the absolute value of O_2Hb and HHb concentrations.

However, there are also several disadvantage of TRS technique. First, it requires complicated instruments which are expensive. Besides, there exists a high level of noise due to the low number of photons [24]. Some advanced instrument, such as glass fibers and the photomultiplier tubes, can reduce the noise, but they are in large size and in danger of being destroyed. Therefore, TRS technique usually only implements on laboratory-based devices.

2.3.4 Phase-Modulated Spectroscopy

In 1949, frequency domain measurement, also known as phase-modulated spectroscopy (PMS), was first proposed by Chance et al. in [25]. PMS instruments modulate a continuous light source at a given frequency and there exists a phase shift between the light entering and leaving the tissue,

as shown in Fig. 8. This phase shift can be used to calculate the time interval between light incident

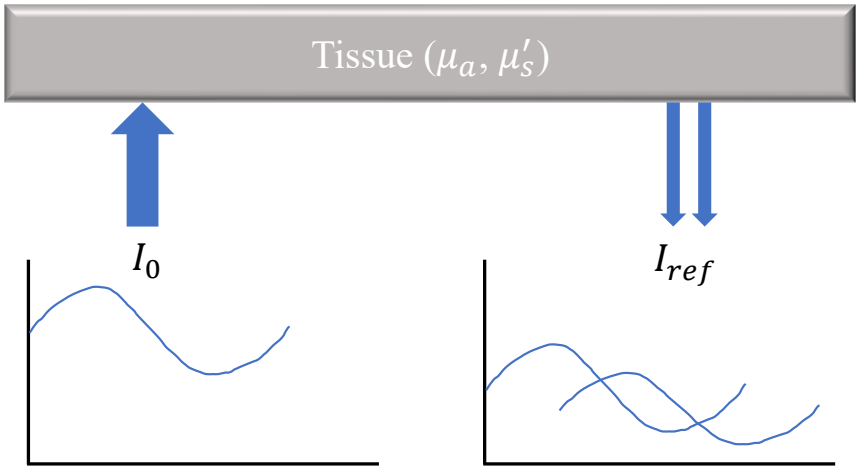

Figure 8: Phase-Modulated Spectroscopy Technique

and light detection. Then, the corresponding DPF can be calculated using different wavelengths and modulating frequencies within the radio frequency range, as shown below

$$\mathrm{DPF} = \frac{L}{d} = \frac{\phi c_v}{2\pi f n_t d} \tag{17}$$

where ϕ represents the phase shift, and f represents the modulation frequency.

In PMS instruments, the attenuation of light should also be recorded. With the information of attenuation and DPF, it can be used to generate the absolute value of the concentrations of O_2Hb and HHb.

The basic components in the PMS experimental device include laser, oscillator, phase modulator, sample, detector and recorder. PMS requires a lot of hardware and becomes more complicated due to its conversion technique. Therefore, PMS is not suitable for wearable devices.

2.3.5 Conclusion

According to the principles of four measurement technologies introduced above, the comparison of advantages and disadvantages of CWS, SRS, TRS and PMS [8] are listed in table 1.

Parameters	**CWS**	**SRS**	**TRS**	**PMS**
C_{O_2Hb}, C_{HHb}	Changes	Changes	Absolute	Absolute
SO_2	No	No	Yes	Yes
μ_a	No	No	Yes	Yes
μ_s	No	No	Yes	Yes
DPF	No	No	Yes	Yes
Sampling Rate	≤ 100	≤ 100	≤ 1	≤ 10
Portability	Wearable	Wearable	Portable	Portable
Cost	Low	Low	High	Moderate
Light Source	LED or laser diode	LED or laser diode	laser diode	laser diode
Detector	Silicon photodiode	Silicon photodiode	Photomultiplier tube	Avalanche photodiode

Table 1: Comparison of CWS, SRS, TRS and PMS

2.4 Monitoring and Evaluation of Training

Training is a complex behavior and workouts vary between sports. Commonly, training can be classified into four categories: endurance, interval, strength and skill. In general, endurance training can train the aerobic power system, interval training can train the anaerobic glycolytic system, strength training can train the phosphagen system, and skill training can train the central nervous system [26].

It is necessary for athletes to practice with a properly executed training program, since scientific training methods can not only improve endurance, strength and skill, but also optimize metabolic efficiency and adaptability. On the contrary, an improper training plan may lead to injuries and illness, which are something athletes need to avoid. In order to maximize efficiency and adaptability and avoid injuries and illness, athletes must be able to accurately measure training intensity and duration. Physiological monitoring is important in training, such as monitoring of heart rate, blood lactate, oxygen uptake, and tissue oxygenation, and it is suitable for measuring training intensity that maintains at a stable intensity for at least a few minutes.

2.4.1 Heart Rate

Heart rate is the most widely-used metric of measuring training intensity. It can be measured by an electrocardiograph in the laboratory or a series of miniaturized electrocardiographs for fieldwork. The most reliable method is to detect the electrical activity of the heart and use it to calculate the heart rate [26]. Athletes can also directly measure the heart rate by palpation of an artery in the wrist or neck, but exercise has to be temporarily stopped for the measurement and the resulting estimate is not accurate. Heart rate is a global parameter of the athlete's body, which is unable to represent the training intensity of specific muscles.

2.4.2 Blood Lactate

Blood lactate concentration is measured by many athletes and trainers to determine the lactate threshold. During strenuous exercise, muscles produce lactate which diffuses into the blood by the anaerobic glycolytic pathway. Therefore, the concentration of blood lactate will increase 1 - 2 $mmol \cdot L^{-1}$ above the resting value. Anaerobic threshold, also called lactate threshold, is defined as the highest intensity of lactate stability, which corresponds to a blood lactate concentration of approximately 4 $mmol \cdot L^{-1}$. Exercise at this intensity can last 30-60 minutes until fatigue occurs. Low intensity workouts can not cause an increase in blood lactate, while at high intensity, blood lactate will not reach a stable value before the athlete fatigues. During the training process, athletes measure the blood lactate mainly to determine the anaerobic threshold and then arrange a training intensity plan relative to the threshold.

Although measuring blood lactate can provide a very accurate measurement of the effect of training intensity, there still exist some disadvantages. First, the value of lactate threshold varies from person to person. Even within the same athlete, the anaerobic threshold will change due to changes in muscle glycogen content caused by recent training or diet. Besides, the measurement of blood lactate test is usually done with a finger or earlobe prick, which is invasive.

2.4.3 Oxygen Uptake

Oxygen in the human body can oxidize glucose into adenosine triphosphate (ATP) to provide energy. During the workout, the demand for oxygen increases due to human muscles work harder

than usual. As a result, the heart rate rises and breathing increases to provide more oxygen to the working muscles. Oxygen uptake (VO_2) is the amount of oxygen taken in and consumed by the body per minute, which is a good measure of the intensity of steady-state workout. Maximal oxygen uptake($VO_2\,\max$) is the maximum value of VO_2 during an endurance exercise. It reflects cardio-respiratory adaptability and endurance during exercise.

In practice, the measurement of VO_2 and $VO_2\,\max$ requires athletes to breathe into special equipment in order to collect or analyze expired gas. This requirement restricts monitored training to only be performed in laboratories or professional locations. Therefore, long-term monitoring of VO_2 and $VO_2\,\max$ is difficult to achieve. And the measurement of $VO_2\,\max$ cannot be used for precise intensity training, because it measures volume rather than intensity.

2.4.4 Muscle Oxygen Saturation

In a well-trained athlete's body, the exercising muscle consumes approximately 80% of oxygen. Muscle oxygen saturation (SmO_2) is a direct measure of the amount of oxygen in the muscle tissue. If the supply exceeds the demand, oxygenation will be high and the muscles will be in a state of aerobic metabolism, while if demand exceeds supply, oxygenation will be low and muscles will be in a state of anaerobic metabolism. SmO_2 can accurately and continuously measure the intensity level and duration of specific muscles, enabling athletes and coaches to adjust training in real-time to better adapt to training.

Currently, there are three methods of measuring muscle oxygen: electrochemical, transcutaneous PO_2, and near-infrared spectroscopy (NIRS). In electrochemical, there are various invasive methods for measuring dissolved oxygen in medium. The transcutaneous PO_2 measurement method only measures dissolved oxygen in skin, but not in muscle tissues. Although these two methods are used in medicine, there are currently no sports science uses. For monitoring SmO_2 in human body, NIRS is the principal technology. It is a non-invasive method that uses light in the near-infrared spectrum to measure oxygenated and deoxygenated hemoglobin.

2.5 Tissue Oxygen Saturation Measurement

2.5.1 Definition

In general, oxygen saturation (SO_2) is a measure of the relative concentration of oxygen dissolved or carried in a specific medium. The standard unit of SO_2 is percentage. In clinical medicine, tissue oxygen saturation (StO_2) refers to the degree of oxygenation of blood cells, which is a measure of the percentage of hemoglobin binding sites of oxygen in the blood [27]. StO_2 can be expressed as the ratio of blood oxygen concentration to total hemoglobin concentration (tHb), as shown below

$$StO_2 = \frac{c_{O_2Hb}}{c_{O_2Hb} + c_{HHb}} \times 100\% \tag{18}$$

$$tHb = c_{O_2Hb} + c_{HHb} \tag{19}$$

where c_{O_2Hb} and c_{HHb} are concentrations of oxygenated hemoglobin (O_2Hb) and deoxygenated hemoglobin (HHb).

Muscle oxygen saturation (SmO_2) is the local SO_2 value in a specific muscle. Due to the exist of myoglobin in muscles, SmO_2 can be defined by

$$SmO_2 = \frac{c_{(O_2Hb+O_2Mb)}}{c_{(O_2Hb+O_2Mb)} + c_{(HHb+Mb)}} \times 100\% \tag{20}$$

where $c_{(O_2Hb+O_2Mb)}$ is the concentration of oxygenated heme, including O_2Hb and oxymyoglobin (O_2Mb), and $c_{(HHb+Mb)}$ is the concentration of deoxygenated heme, including HHB and deoxymyoglobin (Mb). And the total concentration of heme in the muscle is described as

$$tHb = c_{(O_2Hb+O_2Mb)} + c_{(HHb+Mb)} \tag{21}$$

In muscle tissue, myoglobin (Mb) accounts for approximately 10% of the NIRS light absorption signal [28]. Since the absorption spectra of myoglobin and hemoglobin are very similar in the NIR wavelength range, it is difficult to distinguish the role of myoglobin and hemoglobin in *in vivo* measurements [6].

2.5.2 Measurement Technologies

There is growing interest in measuring human tissue oxygen saturation (StO_2), especially using NIRS for continuous and non-invasive measurement. In 1894, the absolute and relative amounts of

O_2Hb and HHb was first measured *in vitro* by spectroscopy technology [29]. In 1938, Matthes and Gross from Germany determined O_2Hb and HHb in human tissue using two wavelength, one is in red and another in near-infrared region [30–32]. In terms of quantitative measurement, modified Beer-Lambert's law [7] was proposed in 1988. It describes light attenuation with scattering as equation (8), which is often used in many studies. In 1977, Jöbsis first introduced the application of NIRS on measuring attenuation spectra across the head of a cat to non-invasively monitor changes in oxygenation saturation in the brain [33]. Jöbsis is the pioneer of using NIRS and a lot of NIRS instruments and methods were designed and built after that.

Continuous-wave spectroscopy (CWS) is the most economic and simplest technique for real-time monitoring human tissue oxygenation. Although the traditional CWS method can only calculate the change values of tissue oxygenation, many researcher have proposed new methods to generate the absolute values. The study of Myers et al. [34] proposed a second derivative spectroscopic method for quantifying hemoglobin oxygen saturation in tissue. They used four wavelengths with a 40nm interval and applied a second derivative spectroscopic method to remove the effect of scattering [34]. A StO_2 calibration curve was generated in the *in vitro* measurement by scaled second derivative attenuation at 720 nm. The limitation of this method is caused by the difference between the *in vitro* and *in vivo* measurements. Two Russian scientists, Stratonnikov and Loschenov, proposed a CWS technique in the visible wavelength range (510 nm - 590 nm) to measure the hemoglobin oxygen saturation and relative hemoglobin concentration [35]. It was assumed that except the attenuation of O_2Hb and HHb, all other contributions to the attenuation including scattering are smooth wavelength functions and can be approximated by Taylor series expansion [35]. Linear least square was applied to fit the measured attenuation spectrum collected from human fingers to the Taylor expansion attenuation model. After fitting, the product of the optical pathlength and the O_2Hb and HHb concentration can be obtained, and then the StO_2 can be calculated [35]. In theory, this is a simple and robust method, but visible light cannot penetrate tissue as deep as NIR light. Based on their method, Yang et al. [6] used a bound-constrained non-linear least squares fitting of the measured attenuation spectrum in broadband NIRS (725 nm – 880 nm) to the modeled spectrum [6]. Two source-detector distances were utilized with an orthogonalization method to reduce the scattering effects of the fat and the influence of skin melanin [36]

.

When measuring tissue oxygenation by CW-NIRS, the wavelengths between 650 nm and 950 nm are commonly used. Choosing the most suitable wavelengths for measuring O_2Hb and HHb concentration is a mathematical optimization problem. Three main aspects need to be considered: (i) the number of wavelengths used; (ii) the biological model of the tissue; (iii) the mathematical approach to solve the optimization problem [33]. For two-wavelength measurement, many researchers figures that the best choice of wavelength is 830 nm combined with a wavelength in the range less than 780 nm [37]. For measurement using more than two wavelengths, different optimum wavelength combinations were proposed in many studies. From the study of Corlu et al. in [38, 39], in a three layered medium with O_2Hb and HHb as chromophores, the optimal choices for three wavelength are 680 $\pm$ 5 nm, 725 $\pm$ 10 nm and 877 $\pm$ 12 nm. And for four-wavelength measurement, the best choices are 685 $\pm$ 7 nm, 719 $\pm$ 9 nm, 731 $\pm$ 8 nm and 873 $\pm$ 9 nm. Later in the study of Zhu et al. [40], they represent that three wavelengths of 782 nm, 832 nm and 884 nm, and the four wavelengths of 786 nm, 807 nm, 850 nm and 889 nm are optimal.

PMS and TRS are also always used for measuring tissue oxygenation [41–44]. However, due to complicated components and high cost of PMS and TRS instruments, these technique are not suitable for measurements during training. Therefore, they will not be described in more details here.

2.5.3 Commercial Instruments

There are many instruments for *in vivo* measuring tissue oxygenation in the industry, some of which are listed in table 2.

In table 2, among these instruments, only Moxy Monitor [1] uses Monte Carlo simulation based on a tissue model. When the optical properties of the tissue are known, Monte Carlo method can accurately predict the propagation of light through turbid tissue. Monte Carlo simulation is performed on a tissue model to generate simulated path length data when light travels through this tissue, where the absorption rate is set to zero. This model can mimic the scattering properties and geometry of the *in vivo* tissue, including layer thickness and shape. It also uses broadband wavelength as source to improve the measurement accuracy. There are four steps for Moxy Monitor to

Instrument	Technique	Wearable	Source	Measurable Parameters	Company
PocketNIRS Duo	CWS	Yes	LED	ΔtHb,ΔO_2Hb, ΔHHb	DynaSense, Japan
NIRO-500 [45]	CWS	No	Laser	ΔtHb,ΔO_2Hb, ΔHHb	Hamamatsu, Japan
Humon Beta [46]	CWS	Yes	LED	SO_2	Dynometrics, USA
BSX Insight [47]	CWS	Yes	LED	ΔO_2Hb, ΔHHb	BSX Athletics, USA
OXYMON [48, 49]	SRS	No	Laser	SO_2, ΔtHb,ΔO_2Hb, ΔHHb	Artinis, Netherlands
Moxy Monitor [1]	SRS	Yes	LED	SO_2	Fortiori Design, USA
PortaMon [50]	SRS	Yes	LED	SO_2, c_{tHb},c_{O_2Hb}, c_{HHb}	Artinis, Netherlands
NIRO-200NX	SRS	No	LED	SO_2, ΔtHb,ΔO_2Hb, ΔHHb	Hamamatsu, Japan
PortaLite	SRS	Yes	LED	SO_2, c_{tHb},c_{O_2Hb}, c_{HHb}	Artinis, Netherlands
OxiplexTS [51]	PMS	No	Laser	SO_2, c_{tHb},c_{O_2Hb}, c_{HHb}	ISS, USA
TRS-10 [52]	TRS	No	Laser	SO_2, c_{tHb},c_{O_2Hb}, c_{HHb}	Hamamatsu, Japan

Table 2: Commercial instruments for measuring tissue oxygenation

generate SmO_2 value: (i) generating calculated pathlength from a Monte Carlo model; (ii) smoothing the pathlength data; (iii) generating a matrix of diffuse reflectance data at discrete values of tissue parameters and sensor optical properties; (iv) determining the tissue parameters based on diffuse reflectance data [1].

Chapter 3

Quantitative Measurement of Muscle Oxygen Saturation Using 5-Wavelength Near-Infrared Spectroscopy

As mentioned in the previous chapter, muscle oxygen saturation (SmO_2) has become an important reference indicator for athletes' training. SmO_2 is usually non-invasively and quantitatively measured by near-infrared spectroscopy (NIRS). Among the various measurement techniques of NIRS, continuous-wave NIRS (CW-NIRS) is the most economic and simplest method for monitoring SmO_2. Using multiple source-detector distances with CW-NIRS, also called spatially resolved NIRS (SR-NIRS), can reduce the absorption of shallow layer tissue and improve the accuracy of muscle oxygenation measurement.

In this chapter, a methodology of quantitatively measuring SmO_2 using SR-NIRS with two source-detector distances is introduced. First, the structure and principle of the measuring instrument is described. Then, an algorithm for calculating the absolute value of SmO_2 based on the measured data in the main measurement distance is explained in detail. In addition, to evaluate the accuracy of this algorithm, simulated attenuation spectra were calculated for three simulated tissues with different light scattering conditions, including non-scattering medium, forearm, and calf. Next, to reduce the absorption and scattering of superficial tissues, such as skin and fat, an orthogonalization technique is applied to the measured data from both main and auxiliary measurement distances. Besides, to collect the useful data from detectors, two training procedures are

introduced. And the data processing process is explained in a flowchart. Finally, the numerical results generated from the data measured *in vivo* are shown.

3.1 Principle of Measuring Instrument

The measuring instrument in this study is produced by Getwell Health Technology Co., Ltd. [2], which includes LED sources with 5 wavelengths and two photodiode detectors. The structure of this device [2] is shown in Fig. 9.

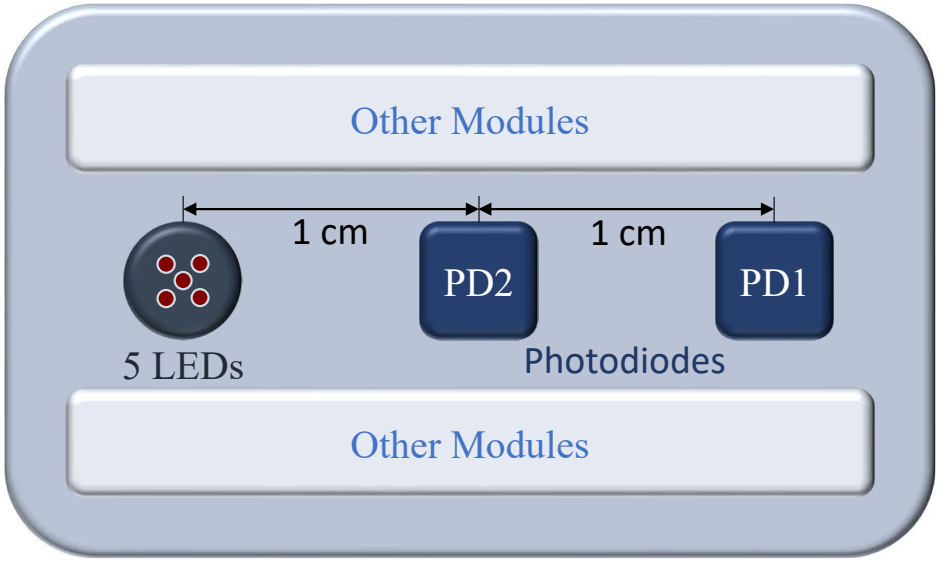

Figure 9: Structure of the Measuring Instrument

In the light source module, one AlGaInP high-brightness LED chip and four AlGaAs high power infrared LED chips are used. The wavelengths of 5 LEDs are 660 nm, 730 nm, 810 nm, 850 nm and 940 nm. The choices of wavelengths are very reasonable, because there are two wavelengths on both sides of the isosbestic point, and another wavelength is close to the isosbestic point. Since the absorption spectra of O_2Hb and HHb are different on both sides of the isosbestic point, the absorption of O_2 Hb and HHb at various wavelengths can be detected sensitively, and the concentration of O_2Hb and HHB can be calculated.

A silicon photodiode is a semiconductor device that converts light into electric current and is

used to detect the intensity of reflected light. This device includes two photodiodes. The photodiode far away from the light source (PD1) is the main detector that measures the reflected light intensity at the main measurement distance. And the detector near the light source (PD2) is used as an auxiliary detector to reduce the absorption and scattering of superficial tissues.

In order to generate the muscle attenuation spectrum, both the incident and reflected light intensities should be known. The LEDs are powered by an adjustable electrical current and different current will produce different incident light intensity. However, the light intensity is difficult to measure both in light source and detector. Therefore, there are some other modules in this measuring device, such as amplification circuit, analog-to-digital converter, etc., to convert the immeasurable light intensity into measurable voltage and current. In this device, the photodiodes are used to convert received light into an electrical current, and then an amplification circuit is used to amplify the small current to a large voltage. The reflected light density can be represent by detecting this voltage and current combining the characteristics of the amplifier circuit and the photodiode.

In order to represent the incident light intensity, additional measurements with another separate photodiode circuit are performed. The LEDs are powered separately by different current to produce different light intensity, which is measured by a independent photodiode circuit. The value of current in this photodiode circuit will be used to represent the incident light intensity. For every wavelength, the relationship of the current that powers the LEDs (I_{LED}) and the current that is detected in the photodiode circuit (I_{in}) are shown in Fig. 10.

3.2 Quantitative Measurement Algorithm

In human muscles, the light attenuation spectrum can be defined in equation (5). Due to the strong tissue scattering, the region of photon trajectory between the light source and the detector passing through the tissue looks like a banana shape, as shown in Fig. 11. The photon pathlengths throught the tissue can be represent by a probability function P. Therefore, the intensity of detected light is determined by absorbing and scattering properties of the tissue by following equation:

$$\frac{I_1}{I_0} = \int_0^\infty P\left(\mu_s, g, l\right) \cdot \exp\left(-\mu_a l\right) dl \tag{22}$$

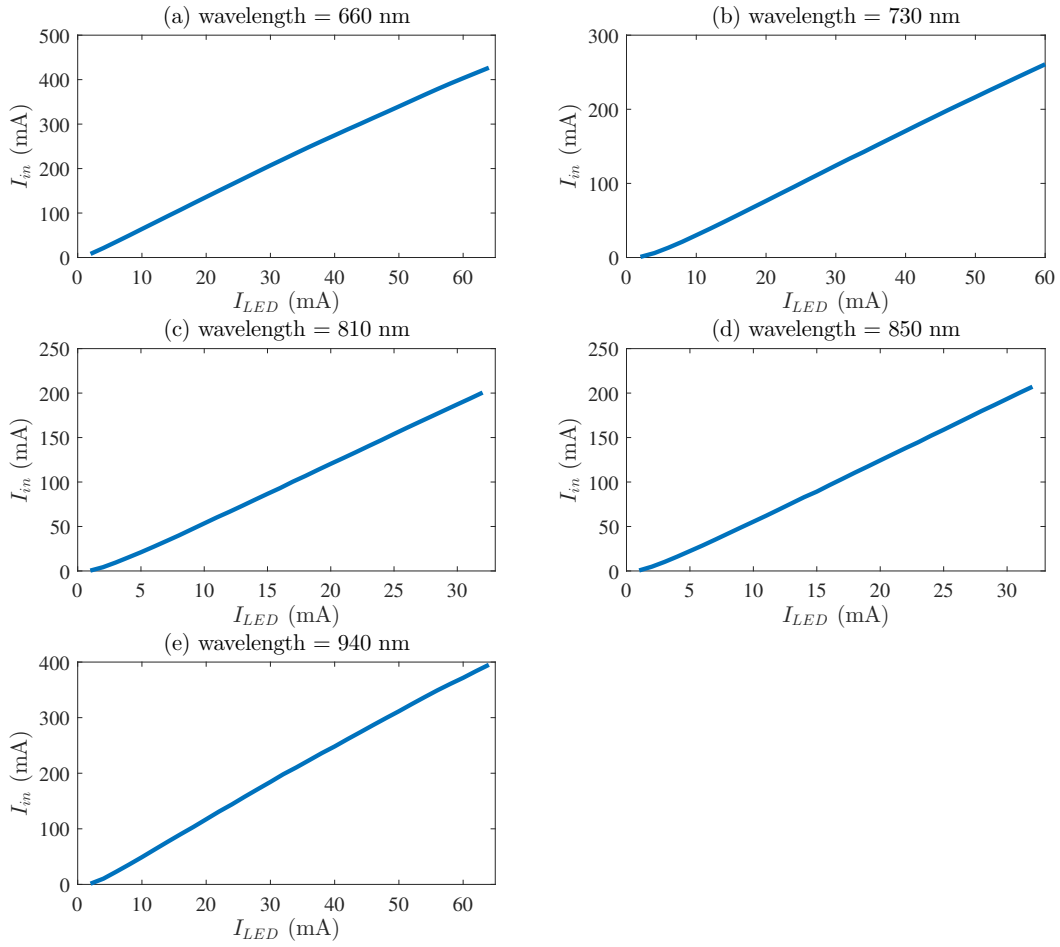

Figure 10: Relationship of the current that power the LEDs (I_{LED}) and the current that detected in the photodiode circuit (I_{in})

where $P(\mu_s, g, l)\, dl$ is a dimensionless value, which represents the probability of photon pathlengths in the small interval dl when the absorption pathlength distribution function is unknown [35].

As mentioned in the previous chapter, muscle oxygen saturation (SmO_2) can be defined as the ratio of oxygenated heme (O_2Hb and O_2Mb) concentration to total heme concentration, as shown in equation (20). In order to calculate the absolute value of SmO_2, a muscle attenuation spectrum approximation model using Taylor series expansion was introduced by Stratonnikov et al. in [35].

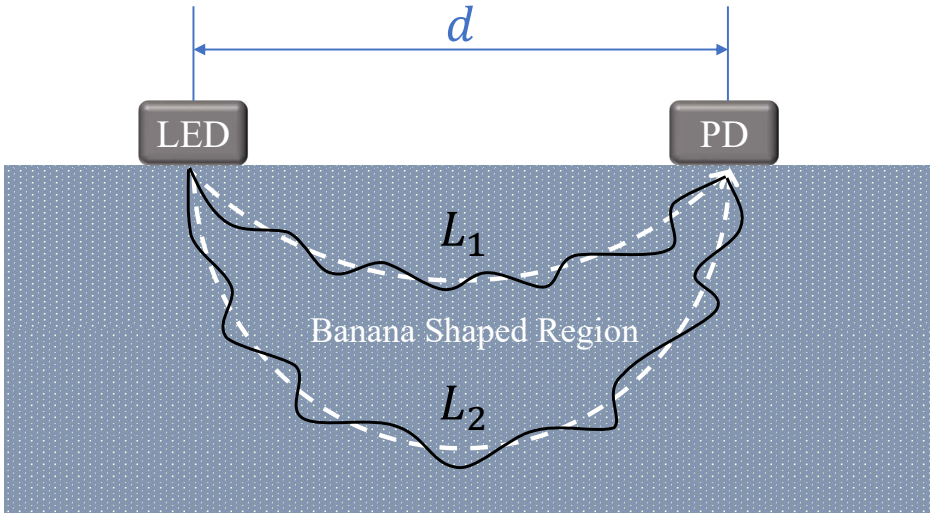

Figure 11: Banana shaped region of contributing photon trajectories

3.2.1 Taylor Series Expansion Model

Assuming that the attenuation spectrum A is a smooth function of μ_a, the Taylor series expansion described in Appendix A.1 can be applied to A in equation (5) at some value $\mu_a = \mu_a^0$ [35] as follow:

$$\begin{aligned} A(\mu_a) &= \sum_{n=0}^{\infty} \frac{A^{(n)}(\mu_a^0)}{n!} \cdot \left(\mu_a - \mu_a^0\right)^{(n)} \\ &\approx A\left(\mu_a^0\right) + A'\left(\mu_a^0\right) \cdot \left(\mu_a - \mu_a^0\right) + \cdots \end{aligned} \tag{23}$$

In equation (23), it can be observed that the expansion coefficient A' is equivalent to the average photon pathlength $\langle L \rangle$ through the tissue by calculation the first derivative to A over μ_a as follow:

$$\langle L \rangle = \frac{\partial A}{\partial \mu_a}|_{\mu_a=\mu_a^0} = \frac{\int_0^\infty l \cdot P(\mu_s, g, l) \cdot \exp(-\mu_a l) dl}{\int_0^\infty P(\mu_s, g, l) \cdot \exp(-\mu_a l) dl} \tag{24}$$

Applying $A' = \langle L \rangle$ in equation (23) can get the following formula:

$$A = A_0 + \langle L \rangle \mu_a \tag{25}$$

where A_0 represents unknown contribution of scattering.

Comparing equation (25) with modified Beer-Lambert's law in equation (8), the Taylor coefficient $\langle L \rangle$ in equation (25) is independent of μ_a while the differential pathlength factor (DPF) in equation (8) is depend on the tissue property of absorption coefficient μ_a.

In human muscle tissue, light attenuation is caused by light absorption from hemoglobin, myoglobin, water and other components, such as skin pigment, and light scattering in fat. Therefore, the absorption coefficient as a function of wavelength is described as follows:

$$\mu_a(\lambda) = \mu_a^b(\lambda) + [\varepsilon_{O_2Hb}(\lambda)\, c_{O_2Hb+O_2Mb} + \varepsilon_{HHb}(\lambda)\, c_{HHb+Mb} + \varepsilon_w(\lambda)\, c_w] \ln(10) \tag{26}$$

where ε_{O_2Hb}, ε_{HHb} and ε_w are the extinction coefficients of O_2Hb, HHb and water, which are shown in Fig. 3 and Fig. 4. $c_{O_2Hb+O_2Mb}$, c_{HHb+Mb} and c_w are the concentration of oxygenated heme, deoxygenated heme and water. And $\mu_a^b(\lambda)$ represents the absorption coefficient of other components in the tissue.

Taking into account equation (23) and equation (26), an attenuation model can be described by

$$\begin{aligned} A_{model}(\lambda) &= a_0 + a_1\lambda + \langle L\rangle \mu_a(\lambda) \\ &= a_0 + a_1\lambda + \langle L\rangle \\ &\quad \cdot [\varepsilon_{O_2Hb}(\lambda)\, c_{O_2Hb+O_2Mb} + \varepsilon_{HHb}(\lambda)\, c_{HHb+Mb} + \varepsilon_w(\lambda)\, c_w] \ln(10) \end{aligned} \tag{27}$$

where a_0 represents the wavelength-independent absorption from chromophores other than heme and water in the tissue. $a_0 + a_1\lambda$ describes the attenuation caused by light scattering and also includes the background absorption $\mu_a^b(\lambda)$.

3.2.2 Non-Linear Least Squares Fitting

In the Taylor expansion model in equation (27), only the parameters ε and the wavelengths λ are known, and the parameters a_0, a_1, $\langle L\rangle$ and concentration c are unknown. In order to obtain the absolute value of SmO_2 from equation (20), $c_{O_2Hb+O_2Mb}$, c_{HHb+Mb} and c_w should be known. A bound-constrained non-linear least squares fitting can be implemented to fit the measured attenuation spectrum $A_{measure}$ to the modeled attenuation spectrum A_{model}. The values of unknown parameters can be obtained by minimizing the sum of square difference χ^2 between $A_{measure}$ and A_{model} with least squares method by

$$\min \chi^2 = \min \sum_{i=1}^{5} [A_{model}(\lambda_i) - A_{measure}(\lambda_i)]^2 \tag{28}$$

where λ_i represents the ith wavelength of the total five wavelengths, including 660 nm, 730 nm, 810 nm, 850 nm and 940 nm.

However, non-linear least squares fitting requires that the number of unknown parameters should less than or equal to the number of observations. In our case, there are only five wavelength that can be used to obtain five values of $A_{measure}$ but there are six unknown parameters (a_0, a_1, $\langle L \rangle$, $c_{O_2Hb+O_2Mb}$, c_{HHb+Mb} and c_w) waiting to be generated. Therefore, the concentration of water c_w in muscle tissue can be fixed at 62% by volume, which was evaluated by Matcher et al. in 1994 [53]. In this way, the non-linear least squares fitting problem can be solved with five observations and five unknown parameters.

3.2.3 Boundaries of Non-Linear Least Squares Fitting

Since the attenuation model in the equation (27) is related to an actual problem, each parameter should have a corresponding physical meaning. Therefore, each unknown parameter should have a reasonable boundary in the non-linear least squares fitting.

The parameters $c_{O_2Hb+O_2Mb}$ and c_{HHb+Mb} represent the concentration of oxygenated heme and deoxygenated heme. In human muscle, the concentration of total hemoglobin and myoglobin (tHb) in equation (21) usually does not exceed the molar concentration of 0.1 mM [54]. Therefore, the boundaries of $c_{O_2Hb+O_2Mb}$ and c_{HHb+Mb} can both be set to $(0, 0.1]$.

The term $\langle L \rangle$ represents the average photon pathlength. Due to the main source-detector distance d is 2 cm, the lower bound of $\langle L \rangle$ should be 2 cm. $\langle L \rangle$ is approximately equal to the actual pathlength $L = \mathrm{DPF} \cdot \mathrm{d}$. In human calf muscle, the value of DPF in NIR wavelength range is between 4.38 and 6.83 [19]. Therefore, when measuring calf muscle, the upper bound of $\langle L \rangle$ can be set as $7 \times 2\ cm = 14\ cm$. In human forearm muscle, the value of DPF in NIR wavelength region is between 3.16 and 5.29 [19]. Therefore, when measuring forearm muscle, the upper bound of $\langle L \rangle$ can be set as $5.5 \times 2\ cm = 11\ cm$. In conclusion, when measuring calf muscle, the boundaries of $\langle L \rangle$ can be set as $(2, 14]\ cm$, and when measuring forearm muscle, the boundaries of $\langle L \rangle$ can be set as $(2, 11]\ cm$.

a_0 and a_1 represent the attenuation caused by light scattering. The reduced scattering coefficient μ_s' can be described by a linear function of wavelength with negative slope [55], which is $a_0 + a_1\lambda$. The reduced scattering coefficients μ_s' of calf and forearm are shown in Fig. 12. a_1 means negative slope, so it should be negative. Therefore, the boundary of a_1 is $(-\infty, 0)$. And a_0 can be any real

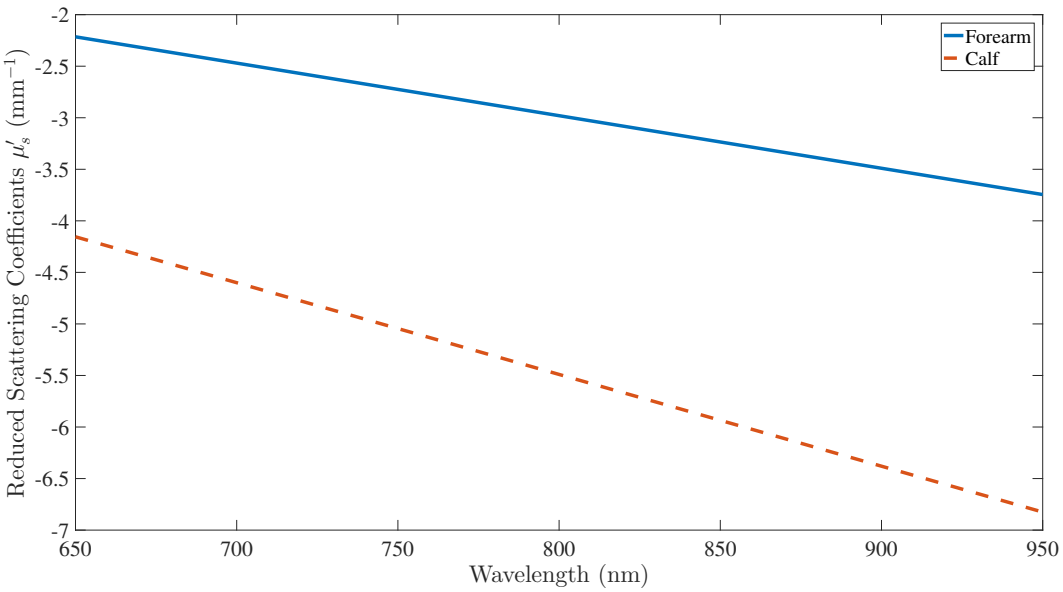

Figure 12: Reduced scattering coefficient in NIR region

number.

3.2.4 Trust-Region-Reflective Least Squares

To solve a non-linear least squares problem, the basic idea is to approximate the model by a linear one and to refine the parameters by successive iterations. There exist a lot of algorithms, such as Gauss–Newton method [56], Levenberg–Marquardt algorithm [57], singular value decomposition [58], direct search methods [59] and trust-region-reflective algorithm [60]. Many methods used in the Optimization Toolbox solvers are based on trust-region, which is a simple and powerful concept in optimization. Coleman et al. proposed the trust-region-reflective least squares algorithm, which is defined by minimizing a quadratic function subject only to an ellipsoidal constraint [60].

Consider a problem of calculating a local minimizer of a smooth nonlinear function with boundaries on the variables, as shown bellow:

$$\min f\left(x\right), lb \leq x \leq ub \tag{29}$$

Note that some components of the lower bound (lb) and upper bound (ub) can be infinite, which means there is no boundary in this direction.

The first derivative and second derivative can be represented as

$$g(x) = \nabla f(x) \tag{30}$$

$$H(x) = \nabla^2 f(x) \tag{31}$$

Assume that x^* is a local minimum, the first necessary condition that x^* should satisfy is:

$$g(x^*) \begin{cases} = 0, \ if \ lb_i < x_i < ub_i \\ \leq 0, \ if \ x_i = ub_i \\ \geq 0, \ if \ x_i = lb_i \end{cases} \tag{32}$$

Also assume a vector $v(x)$ is defined as follows:

$$v(x)_i = \begin{cases} ub_i - x_i, \ if \ g_i < 0 \text{ and } ub_i < \infty \\ x_i - lb_i, \ if \ g_i > 0 \text{ and } lb_i > -\infty \\ 1, \ \text{otherwise} \end{cases} \tag{33}$$

which represents the distance between the anti-gradient point and the bounds.

Based on $v(x)$, a diagonal matrix $D(x)$ can be defined as

$$D(x) = \text{diag}\left(v(x)^{\frac{1}{2}}\right) \tag{34}$$

The purpose of the matrix D is to prevent steps directly into bounds, so that other variables can also be explored during the step. So the optimization problem can be defined as a diagonal system of non-linear equations as follows:

$$D^2(x)\, g(x) = 0 \tag{35}$$

The Jacobian of the left hand side exist whenever $x(x)_i \neq 0$ for all i, which is true when x satisfies $lb \leq x \leq ub$. The Newton step of this system satisfies:

$$\left(D^2 H + \text{diag}(g)\, J_v\right) p = -D^2 g \tag{36}$$

where J_v is diagonal Jaconbian matrix of $v(x)$, which elements take values ± 1 or 0. And all elements of the matrix $C = \text{diag}(g)\, J_v$ are non-negative. Let $x = D\hat{x}$, then the corresponding trust-region problem can be formulated as

$$min_p \hat{m}(\hat{p}) = \frac{1}{2}\hat{p}^T B \hat{p} + \hat{g}^T \hat{p}, \ s.t. \|\hat{p}\| \leq \Delta \tag{37}$$

where Δ represents the trust region.

In the original space there is

$$B = H + D^{-1}CD^{-1} \tag{38}$$

and the equivalent trust-region problem is

$$min_p m\left(p\right) = \frac{1}{2}p^T Bp + g^T p,\ s.t. \|D^{-1}p\| \leq \Delta \tag{39}$$

A modified improvement ratio of out trust-region solution is computed as follows:

$$\rho = \frac{f\left(x+p\right) - f\left(x\right) + \frac{1}{2}\hat{p}^T C\hat{p}}{\hat{m}\left(\hat{p}\right)} \tag{40}$$

A sketch of constrained minimization using trust-region-reflective ideas is given as follows:

1. Consider the trust-region problem in "hat" space as described in 37;
2. Compute the corresponding solution in the original space $p = D\hat{p}$.
3. Restrict this trust-region step to lie within bounds. Step back from the bounds by $\theta = \min(0.05, \|D^2 g\|)$ times the step length.
4. Consider a single reflection of the trust-region step. Use 1-d minimization of the quadratic model to find the minimum along the reflected direction.
5. Find the minimum of the quadratic model along the $\hat{g}$. (Rarely it can be better than the trust-region step because of the bounds.)
6. Choose the best step among 3, 4, 5. Compute the corresponding step in the original space as in 2, update x.
7. Update the trust region radius by computing ρ by equation (40).
8. Check for convergence and go to 1 if the algorithm has not converged yet.

The trust-region-reflective was used in the SmO_2 measurement algorithm. It was implemented by "lsqcurvefit" function in Matlab® Optimization Toolbox of Matlab programming language (Mathworks, Inc., Natick, MA).

3.3 Evaluate the Accuracy in Simulated Tissues

Before applying the quantitative measurement SmO_2 algorithm to *in vivo* measurement, its accuracy should first be evaluated. In the simulation, three different tissue light scattering conditions

were used to simulate attenuation spectra, including non-scattering and scattering from the forearm and calf. It needs to be noted that the hemoglobin concentration includes both hemoglobin and myoglobin, and only the muscle layer was simulated in this case. Suppose there are $N = 9$ different theoretical SmO_2 values: 0%, 20%, 40%, 50%, 60%, 70%, 80%, 90% and 100%, which can be considered as real values of SmO_2, and the corresponding attenuation spectra can be considered as simulated attenuation $A_{simulate}$. The quantitative measurement algorithm was applied to the simulated attenuation spectra $A_{simulate}$ to calculate the estimated SmO_2 values. Three analysis methods were used to evaluate the correctness and accuracy of the algorithm.

3.3.1 Simulated Attenuation Spectra

In the simulation, the simulated attenuation spectra $A_{simulate}$ can be regarded as the measured attenuation spectra $A_{measure}$ in the *in vivo* measurement of the previously explained algorithm. For tissues with different type of scattering properties, $A_{simulate}$ can be expressed in different forms. And the wavelength range of this simulation is between 650 nm and 950 nm.

In non-scattering absorbing tissue, the attenuation $A_{simulate}$ at wavelength λ can be expressed by Beer-Lambert's law, similar to equation (6), which is

$$A_{simulate}(\lambda) = L \cdot \mu_a(\lambda) \tag{41}$$

where the differential pathlength L of pure absorption tissue equals the source-detector distance $d = 2\ cm$ in this case.

And the absorption coefficient μ_a as a function of wavelength λ is described by

$$\mu_a(\lambda) = [\varepsilon_{O_2Hb}(\lambda)\, c_{O_2Hb+O_2Mb} + \varepsilon_{HHb}(\lambda)\, c_{HHb+Mb} + \varepsilon_w(\lambda)\, c_w] \ln(10) \tag{42}$$

where the values of extinction coefficients ε_{O_2Hb}, ε_{HHb} and ε_w of each wavelength λ can be found in the studies of [12, 13], which are also shown in Fig. 3 and Fig. 4.

The concentration of water c_w can be fixed to a theoretical value 62% [53]. And the concentration of total hemoglobin and myoglobin (tHb) can be fixed to the molar concentration of 0.1 mM [54], which means

$$c_{O_2Hb+O_2Mb} + c_{HHb+Mb} = 0.1 \tag{43}$$

When the theoretical SmO_2 value is fixed to a specific percentage, the value of $c_{O_2Hb+O_2Mb}$ and c_{HHb+Mb} can be represented as

$$c_{O_2Hb+O_2Mb} = 0.1 \times SmO_2 \tag{44}$$

$$c_{HHb+Mb} = 0.1 \times (1 - SmO_2) \tag{45}$$

Therefore, under non-scattering condition, light attenuation values for each wavelength $A_{simulate}(\lambda)$ can be generated.

For the simulation of scattering in calf and forearm muscles, a single layer infinite slab diffusion model between light attenuation and the absorption coefficients $\mu_a(\lambda)$ and scattering coefficients $\mu_s'(\lambda)$ was used to generate light attenuation spectra [61], as shown below

$$A_{simulate}(\lambda) = -\ln\left[\frac{\sinh\left(\frac{\sigma(\lambda)}{\mu_s'(\lambda)}\right)}{\sqrt{2\pi}\sinh\left(\sigma(\lambda)\cdot d\right)}\right] \tag{46}$$

where the quantity $\sigma(\lambda)$ is calculated by

$$\sigma(\lambda) = \sqrt{3\mu_a(\lambda)\cdot[\mu_a(\lambda) + \mu_s'(\lambda)]} \tag{47}$$

where $\mu_a(\lambda)$ can be calculated by equation (42).

The values of scattering coefficients $\mu_s'(\lambda)$ of calf muscle can be calculated by equation (48), and $\mu_s'(\lambda)$ of forearm muscle can be calculated by equation (49) [55], as shown in follow

$$\mu_s'(\lambda) = -8.9\lambda \times 10^{-3} + 16.3 \tag{48}$$

$$\mu_s'(\lambda) = -5.1\lambda \times 10^{-3} + 11 \tag{49}$$

where λ is in units of nm and $\mu_s'(\lambda)$ is in units of cm^{-1}.

Therefore, under three scattering conditions, light attenuation spectra for all wavelengths with varying SmO_2 values were generated in Fig. 13.

Fig. 13(a) was calculated using equations (41) - (45), which shows the spectra from a non-scattering simulated tissue, where light attenuation only occurs by absorption. Fig. 13(b) and Fig. 13(c) were calculated using equations (46) - (49), which shows the spectra from simulated tissues with calf and forearm scattering properties. Comparing the calf and forearm muscles with non-scattering tissue, the attenuation was significantly increased due to scattering. For the same

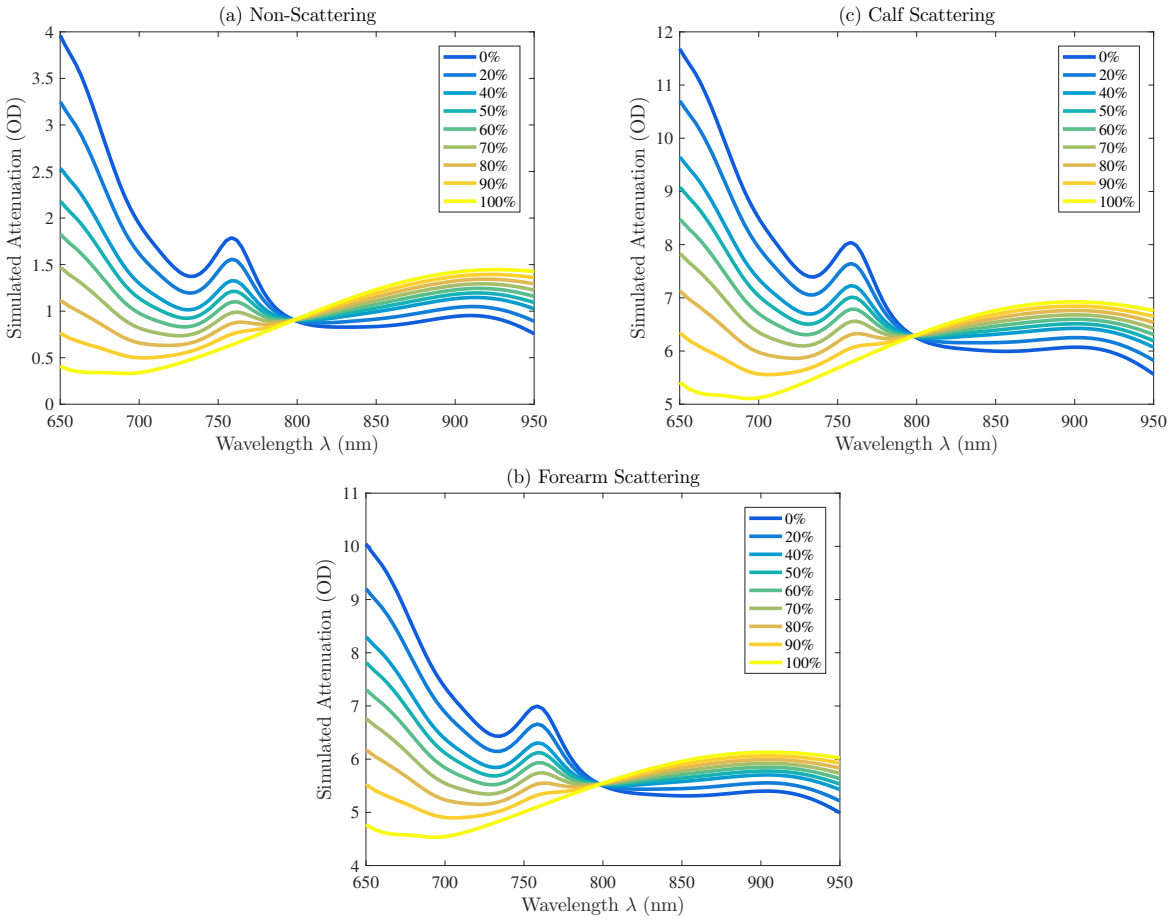

Figure 13: Simulated attenuation spectra with varying SmO_2 values in three different scattering conditions

theoretical SmO_2 values, the shapes of the spectra scattered by the calf and forearm muscles were similar to the shapes of the spectrum without scattering. In addition, with the increase of SmO_2 value, the attenuation spectra were non-linearly affected by the change of the scattering coefficient of different tissue types.

3.3.2 Real and Estimated SmO_2 Comparison

To calculate the value of SmO_2, the nonlinear least squares fitting was applied to the attenuation model in the equation (27), as shown below

$$\min \chi^2 = \min \sum_{i=1}^{n} \left[A_{model}\left(\lambda_i\right) - A_{simulate}\left(\lambda_i\right) \right]^2 \tag{50}$$

where n indicated the number of wavelength, which was five in this case, including 660 nm, 730 nm, 810 nm, 850 nm and 940 nm.

To solve the minimize problem in equation (50), the trust-region-reflective least squares method was applied, which was implemented with "lsqcurvefit" function in Matlab. After least squares fitting, the values of $c_{O_2Hb+O_2Mb}$ and c_{HHb+Mb} were generated and then equation (20) was used to calculate the estimated SmO_2 value for each corresponding theoretical SmO_2 value. The plots of theoretical versus estimated SmO_2 in three scattering conditions are shown in Fig. 14. The diagonal line in these figures represents a perfect match between the theoretical and estimated SmO_2 values.

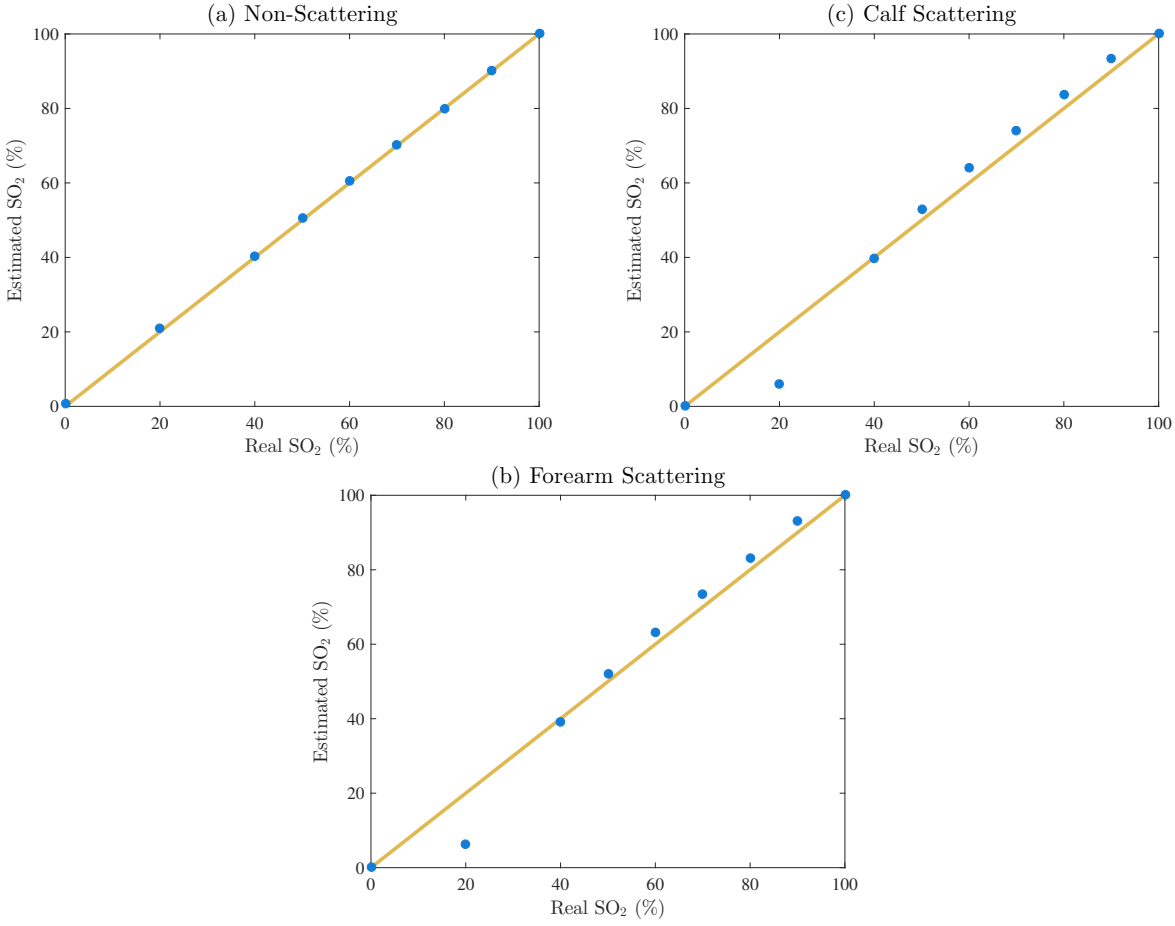

Figure 14: Real versus estimated SO_2 results from simulated spectra in 3 different scattering properties

In Fig. 14(a), it was clear that the estimated SmO_2 values almost equal to the theoretical values in the condition of pure absorption. In Fig. 14(b) and Fig. 14(c), when SmO_2 values were

between 40% and 100%, the estimated results were clustered along the line of perfect prediction with excellent correlation, which represented the estimation was accurate. Therefore, this SmO_2 algorithm can be considered accurate and correct.

3.3.3 Statistical Analysis

There are two metrics to evaluate the accuracy of estimated results of SmO_2, the coefficient of determination (R^2) and the root-mean-square error (RMSE).

In general, the coefficient of determination is explained in A.2. In the case of estimating SmO_2, the mean of the observed data, which is theoretical SmO_2 value, can be defined by

$$\bar{y} = \frac{1}{N} \sum_{i=1}^{N} SmO2_i^{real} \tag{51}$$

where N is the total number of SmO_2 values used in the simulation, which equals nine.

The total sum of squares can be represented by

$$SS_{tot} = \sum_i \left(SmO2_i^{real} - \bar{y} \right)^2 \tag{52}$$

The residual sum of squares can be defined by

$$SS_{res} = \sum_i \left(SmO2_i^{real} - SmO2_i^{est} \right)^2 - \sum_i e_i^2 \tag{53}$$

Therefore, the coefficient of determination (R^2) can be calculated by equation (54) with equations (51) - (53).

$$R^2 = 1 - \frac{SS_{res}}{SS_{tot}} \tag{54}$$

According to the explanation in A.1, the closer the value of R^2 is to 1, the better the estimation result.

In addition, the root-mean-square error (RMSE) describes the estimated measurement error, which can be calculated by

$$\mathrm{RMSE} = \sqrt{\frac{\sum_{i=1}^{N} \left(SmO2_i^{est} - SmO2_i^{real} \right)^2}{N}} \tag{55}$$

The value of RMSE is non-negative. If the RMSE value is relatively small, it indicates that the estimated SmO_2 values are accurate.

Scattering property	$\mathbf{R}^2$	**RMSE(% $\mathbf{SmO_2}$)**
Non-scattering	0.9997	0.6685
Calf scattering	0.9700	7.1877
Forearm scattering	0.9728	6.8351

Table 3: Evaluation metrics of simulated spectra with different scattering properties

Using the estimated and theoretical SmO_2 values in Fig. 14, the values of R^2 and RMSE for three scattering conditions can be calculated, which are shown in table 3.

Obviously, it can be found that the values of R^2 under three scattering conditions were all very close to one. And the value of RMSE under non-scattering condition was very small. Under the conditions of calf and forearm scattering properties, the values of RMSE were also relatively small. In summary, the value of SmO_2 generated by non-linear squares fitting descried above was accurate and reliable.

3.4 Orthogonalization Technique

It is known that the overlying tissues, such as skin and fat, have a great influence on the quantitative near-infrared spectroscopy measurements of human muscles [36]. There is the fact that the penetration depth of light is dependent on the source-detector distance [62]. Based on this fact, a number of methods of correction for the optical effects of the overlying tissues were proposed by researchers [63–65].

An orthogonalization technique in measurement using two-distance fiber-optic probe was proposed by Yang et al. [36]. It was assumed that three layers of tissue are measured, including skin, fat, and muscle, and two source bundles and one detector bundle was used in measurement [36], as shown in Fig. 15. One source was placed close to the detector at a distance of 2.5 mm, which could detect the light that has penetrated only the skin and fat layer. Whereas the second source was placed far to the detector at a distance of 30 mm, which could capture light from the skin, fat and muscle layers. Two light sources were controlled by the controller and only one of them was allowed to emit light at a time [36]. The reflectance light spectra collected from short-distance pair was orthogonalized to light spectra collected from long-distance pair to generate the spectra

describing the attenuation only caused by the muscle layer.

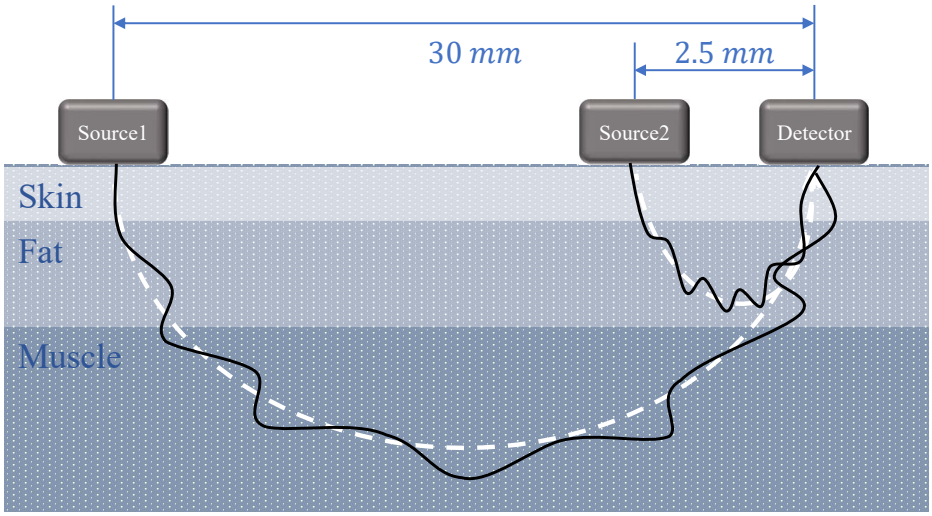

Figure 15: Measurement with two source and one detector

Assuming that the reflectance light spectra of two distances can be represented as R_{sf} and R_{sfm}, where s, f and m represent skin, fat and muscle, respectively. First, the short distance reflectance spectra R_{sf} was mapped to long distance reflectance spectra R_{sfm} by fitting a second-order polynomial at each wavelength, which is

$$R_{sfm}(\lambda) = a_\lambda R_{sf}(\lambda)^2 + b_\lambda R_{sf}(\lambda) + c_\lambda \tag{56}$$

where a_λ, b_λ and c_λ are unitless constants, which can be generated by regression. Once the values a_λ, b_λ and c_λ are obtained, the mapped reflectance spectra $\tilde{R}_{sf}$ can be generated at each wavelength.

Then, a weight matrix can be defined as

$$w = R_{sfm}^T \tilde{R}_{sf} \left(\tilde{R}_{sf}^T \tilde{R}_{sf} \right)^{-1} \tag{57}$$

Finally, orthogonalization can be done between $\tilde{R}_{sf}$ and R_{sfm} [64], described as follow

$$\hat{R}_{ort} = R_{sfm} - \tilde{R}_{sf} w^T \tag{58}$$

where $\hat{R}_{ort}$ represents the spectra which describes the attenuation only caused by the muscle layer.

In the measurement using our device, as shown in Fig. 9, it was also assumed that three layers of tissue was measured, including skin, fat, and muscle, and two photodiode detectors at different

distances were used to receive the reflected light. However, in this device, the distance measured at short-distance (PD2) is not short enough to penetrate only the skin and fat without reaching the muscle layer. In the *in vivo* measurement, the photodiode detector at short distance (PD2) detected the lights that has penetrated mainly the skin and fat layer and a little of the muscle layer. Whereas the detector at long distance (PD1) detected the lights that has penetrated the skin and fat layer and most of the muscle layer. The measurement structure and optical paths of two distances are shown in Fig. 16.

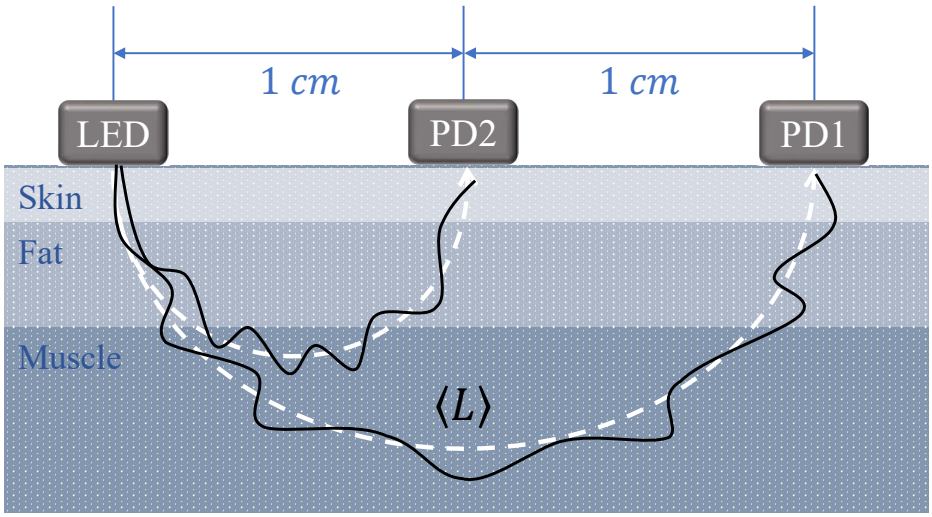

Figure 16: Two-distance measurement structure and optical paths of two distances

Supposed that the attenuation spectra of two distances can be expressed as A_{main} at PD1 and $A_{auxiliary}$ at PD2. And the short distance attenuation spectra $A_{auxiliary}$ was mapped to long distance attenuation spectra A_{main} by fitting a second-order polynomial at each wavelength, as in equation (56), as shown below

$$A_{main}(\lambda) = a_\lambda A_{auxiliary}(\lambda)^2 + b_\lambda A_{auxiliary}(\lambda) + c_\lambda \tag{59}$$

Then, a weight matrix was defined similar to equation (57) as

$$w = A_{main}^T \tilde{A}_{auxiliary} \left(\tilde{A}_{auxiliary}^T \tilde{A}_{auxiliary} \right)^{-1} \tag{60}$$

Finally, orthogonalization was done between $\tilde{A}_{auxiliary}$ and A_{main}, which was similar to equation (58) but with one more parameter α, described as follow

$$\hat{A}_{ort} = A_{main} - \tilde{A}_{auxiliary} \alpha w^T \tag{61}$$

where the parameter α was a unitless constant between 0 and 1 to eliminate the influence of the attenuation of muscle absorption measured by short distance detector (PD1).

The obtained orthogonal attenuation spectra $\hat{A}_{ort}$ can be used as $A_{measure}$ for non-linear least squares fitting in equation (28) to generate the values of SmO_2.

3.5 *In Vivo* Measurement Procedures

For *in vivo* measurement of SmO_2, our device described in Fig. 9 was used. The device was stabilize on the calf to measure the oxygen saturation of the calf muscle. Two processes are required to obtain the values of SmO_2: data collection process and data processing process.

3.5.1 *In Vivo* Data Collection Process

The person wearing the device had to run at different intensities on the treadmill. Each measurement procedure included several different combinations of exercise intensities. There are two types of exercise processes, progression running and interval running. All testing and data collection was done by Getwell Health Technology Co., Ltd. (China). Because the physical conditions of each test subject were different, the actual testing process and speed might vary from the test plan.

Progression Running

Progression runs are designed to begin at trainer's natural pace and end at a faster pace. They are moderately challenging workouts and require more recovery time than base runs but less than tempo or interval runs. The test procedure of progression running was designed as follows:

- Warm up: walk 180 seconds
- Low speed running: 180 seconds
- Moderate speed running: 180 seconds
- High speed running: 180 seconds
- Resting and recovery: walk 240 second

Interval Running

High intensity interval training (HIIT) can be highly effective training, which has been shown to improve aerobic capacity in untrained and moderately active individuals more quickly than continuous moderate run, as well as having potential benefits for highly trained athletes. Interval Runs are workouts that contain short or long bursts of intense effort separated by equal or slightly longer segments of slower running, jogging or walking. The test procedure of interval running was designed as follows:

- Warm up: walk 180 second
- High speed running: 60 seconds
- Resting and recovery: walk 120 seconds
- High speed running: 60 seconds
- Resting and recovery: walk 120 seconds
- High speed running: 60 seconds
- Resting and recovery: walk 120 seconds
- High speed running: 60 seconds
- Resting and recovery: walk 180 seconds

3.5.2 Data Processing Process for *In Vivo* Measurement

For *in vivo* measurement, the data collected from the detectors was the voltage of two circuits of photodiodes. Combined with the resistance information in the circuits, the current in two photodiodes was calculated , which can be represented as $I_{ref}\left(\lambda, main\right)$ and $I_{ref}\left(\lambda, auxiliary\right)$. The reflected light intensity can be represented by these two currents, and the incident light intensity can also be represented by the current measured by a standalone photodiode circuit, denoted as I_{in}.

Therefore, the measured attenuation spectra of two distances were calculated by

$$A_{measure}\left(\lambda, main\right) = -ln\left(\frac{I_{ref}\left(\lambda, main\right)}{I_{in}}\right) \tag{62}$$

$$A_{measure}\left(\lambda, auxiliary\right) = -ln\left(\frac{I_{ref}\left(\lambda, auxiliary\right)}{I_{in}}\right) \tag{63}$$

The measurement frequency was 1hz so that the value of SmO_2 was calculated for each second.

The flowchart for data processing procedure is shown in Fig. 17.

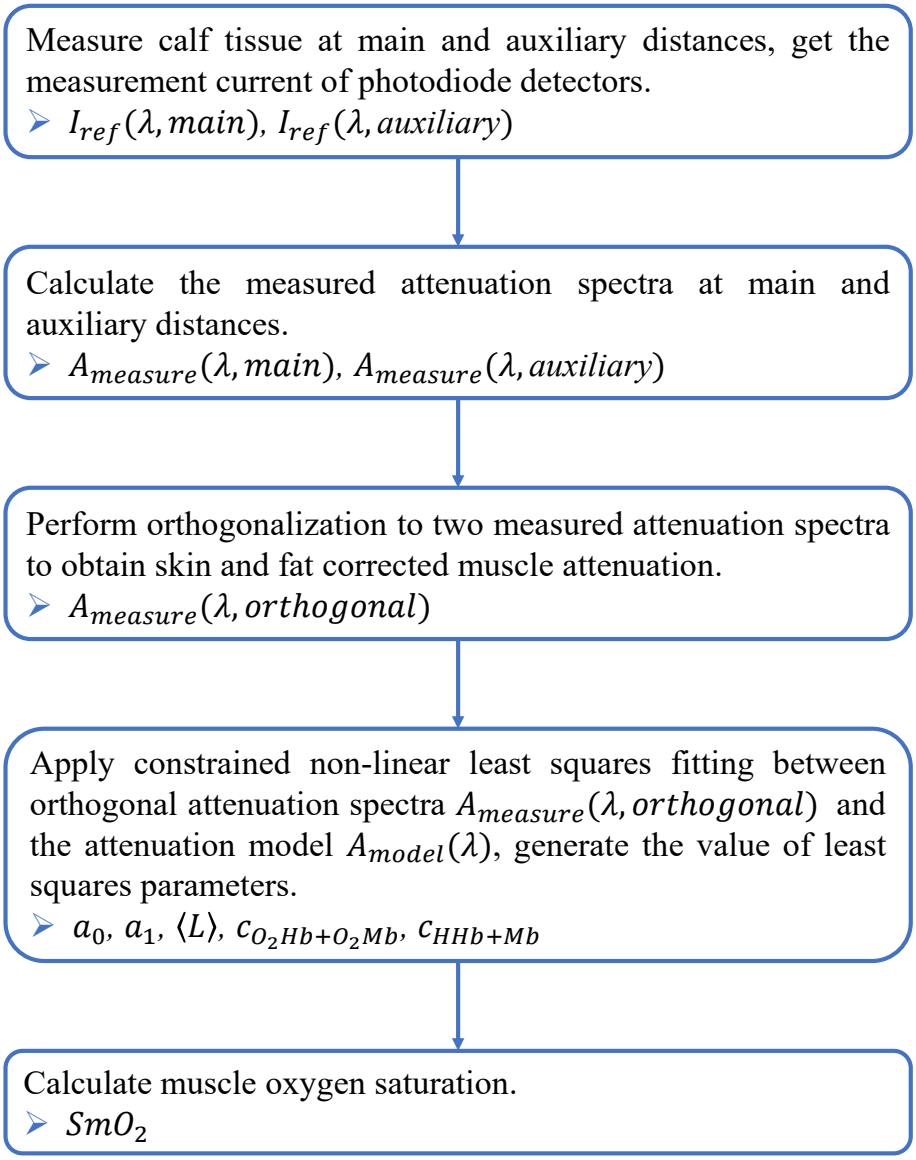

Figure 17: Data processing procedure for *in vivo* measurement

3.6 *In Vivo* Measurement Results

Using *in vivo* measured data, the value of SmO_2 can be calculated. For comparison, some trainers also wear a Moxy monitor [1]. The results from our device were compared with the results of Moxy monitor. Note that the results of Moxy monitor were for reference only, and did not represent

the medically true value of oxygen saturation in muscles. In total, 33 *in vivo* tests were done independently and their SmO_2 results were calculated and analyzed, of which 21 were done by progression running and 12 were done by interval running.

3.6.1 Analysis of Attenuation

It has been explained above that different wavelengths have different absorption coefficients for HHb and O_2Hb, that is to say, when the HHb and O_2Hb in the muscles change, the changes of different wavelengths are different. The wavelengths located to the left of the isosbestic point, in this case 660 nm and 730 nm, are mainly affected by HHb. On the contrary, the wavelengths located to the right of the isosbestic point, in this case 810 nm, 850 nm, and 940 nm, are mainly affected by O_2Hb.

The exercise process was the progression running described previously. During the whole process of measurement, the attenuation of each wavelength measured by main photodiode detector at long source-detector distance is shown in Fig. 18. And the attenuation of each wavelength

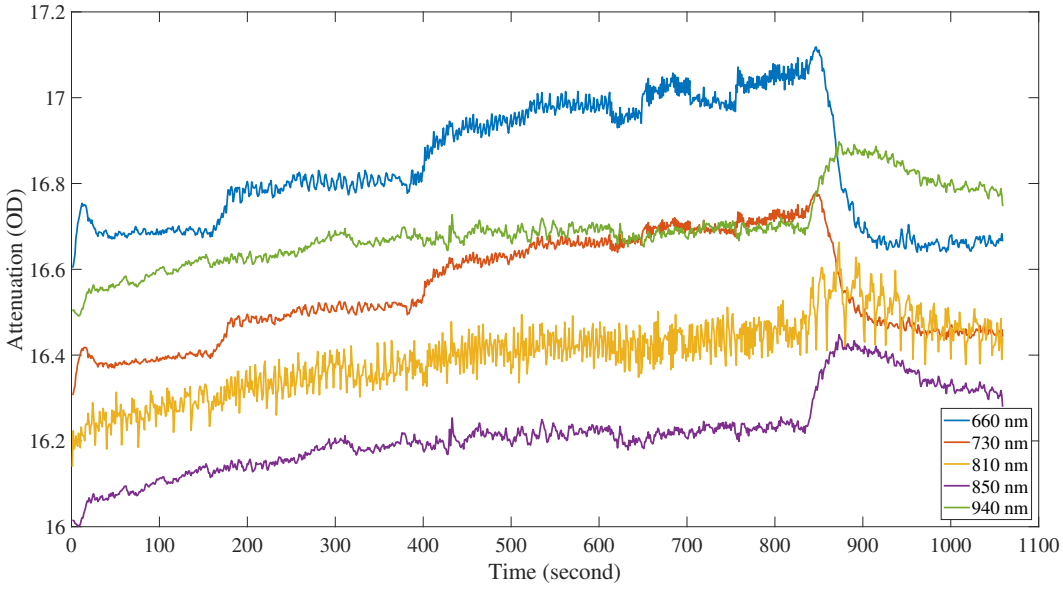

Figure 18: The attenuation of each wavelength measured at long source-detector distance

measured by auxiliary photodiode detector at short source-detector distance is shown in Fig. 19.

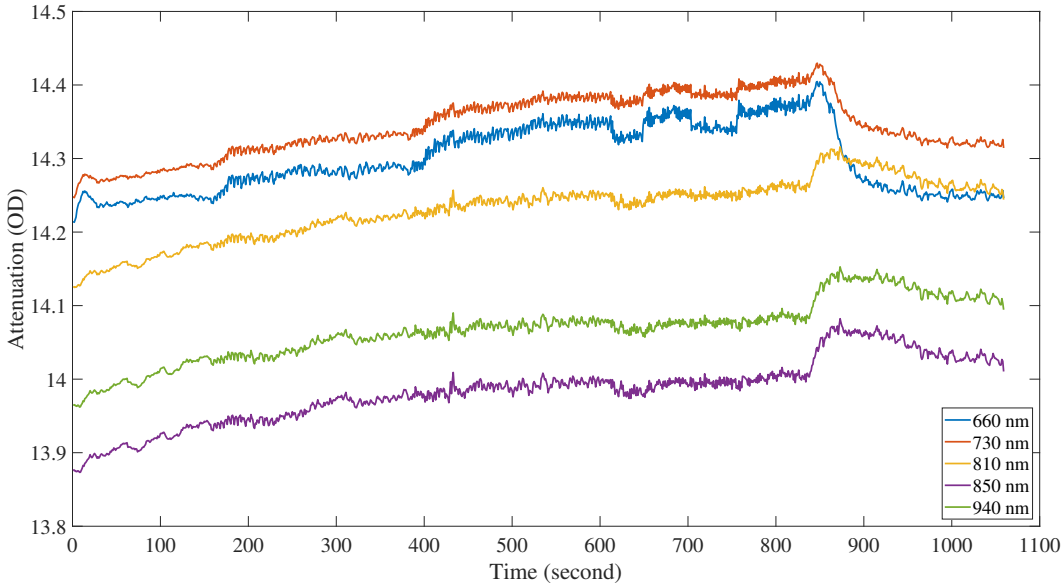

Figure 19: The attenuation of each wavelength measured at short source-detector distance

In these two figures, with the changes of the state of training, the attenuation changes of each wavelength are clearly shown. When running speed increased, muscle oxygen consumption increased, the corresponding O_2Hb in muscles decreased, and HHb increased. At the time around 150s, 400s and 650s, for wavelengths at 660 nm and 730 nm, because HHb increased with the increasing of running speed, the attenuation also increased significantly. At the time of 850s, the state of exercise changed from fast running to walking. Since the muscles suddenly rested, O_2Hb increased and HHb decreased. With the increasing of O_2Hb, the values of attenuation of wavelength at 810 nm, 850 nm, and 940 nm increased rapidly. In contrast, as the decreasing of HHb, the values of attenuation of wavelength at 660 nm and 730 nm decreased rapidly.

3.6.2 Validity of Orthogonalization

As mentioned before, the overlying tissues have a great influence on the quantitative measurement of SmO_2, and the orthogonalization technique with measurement at two source-detector distances can reduce these effects. To demonstrate the applicability of the orthogonal algorithm, a comparison was done between using the data collected at the two detectors with applying orthogonalization technique and only using the data collected at the main detector. The exercise procedure used for

the measurement was the progression running described previously.

The SmO_2 results generated without the orthogonalization technique and the results of Moxy monitor are shown in Fig. 20. The light attenuation spectra of the long-distance detector $A_{measure}\,(\lambda, main)$ was directly used as the measured attenuation in the non-linear least squares fitting. It can be found from this figure that the trend of SmO_2 measured by our device was similar to that measured by Moxy monitor. However, during the time of running with fast speed, which was 500 second to 850 second, it was not normal for some SmO_2 values to be calculated as 0. The value of SmO_2 was not possible to be zero because some blood vessels in the muscle do not exchange oxygen with the tissues so that O_2Hb do not transfer to HHb in these vessels. Because these results were generated from the long source-detector distance data without removing the influence of overlying tissues, the skin and fat might absorb some light so that the attenuation was greater than the actual absorption of muscle. Therefore, the estimated SmO_2 values obtained only from the long source-detector distance data were too small.

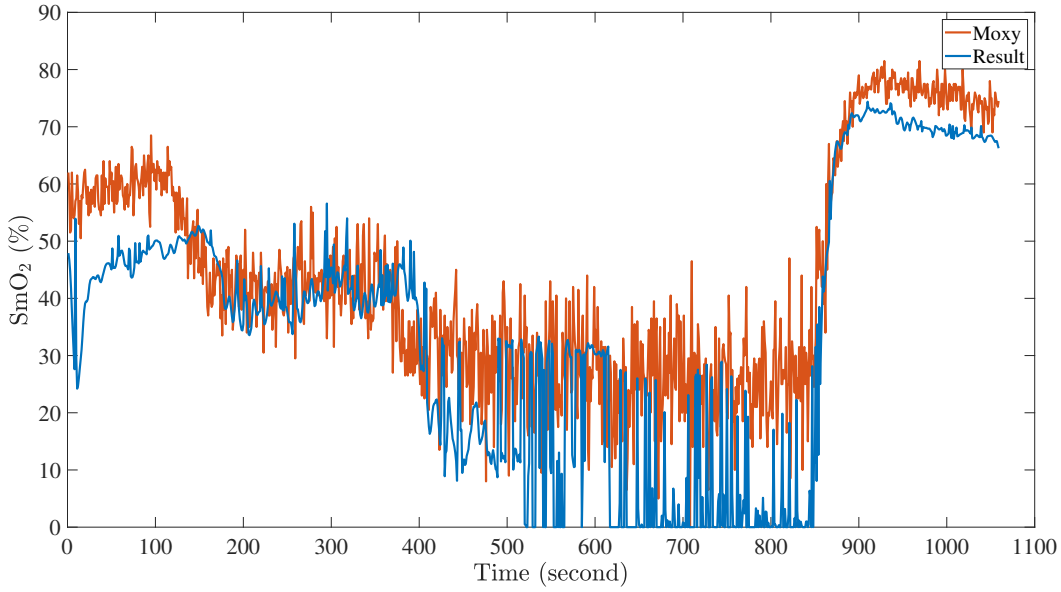

Figure 20: The SmO_2 results generated only from the data of the main detector and the results of Moxy monitor

The SmO_2 results generated with the orthogonalization technique and the results of Moxy monitor are shown in Fig. 21. After using the orthogonal method, the influence of the overlying

tissues was reduced and the values that were previously too low were calculated correctly. This has shown that the orthogonalization technique was effective.

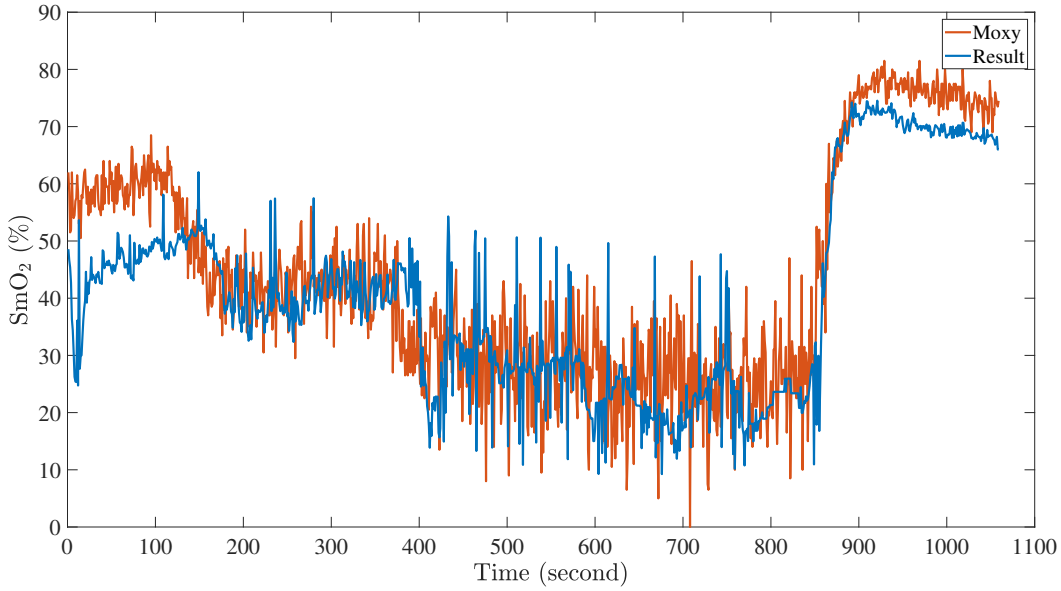

Figure 21: The SmO_2 results generated with the orthogonalization technique, and compared with the results of Moxy monitor

3.6.3 SmO_2 Measurement Results

The SmO_2 results of three complete independent training of the progression running are shown in Fig. 21, 22, and 23.

Use the results in Fig. 22 as an example to explain the changes of oxygen saturation in calf muscle during progression running. It is clear that the value of SmO_2 has four obvious changes. At around 200 seconds, the trainer changed from walking to running, so oxygen consumption increased, resulting in a decrease of SmO_2 value. Then at around 450 seconds, when the running speed increased, there was a rapid decrease of SmO_2 value due to higher oxygen demand. At around 750 seconds, the trainer started to run at the highest speed so that the SmO_2 value decrease again. After the trainer had a rest to recover, the SmO_2 value increased rapidly to the highest, even higher than the value before exercise. This is because when high-intensity training was suddenly stopped, the oxygen consumption immediately decreased but the volume of oxygen delivery was

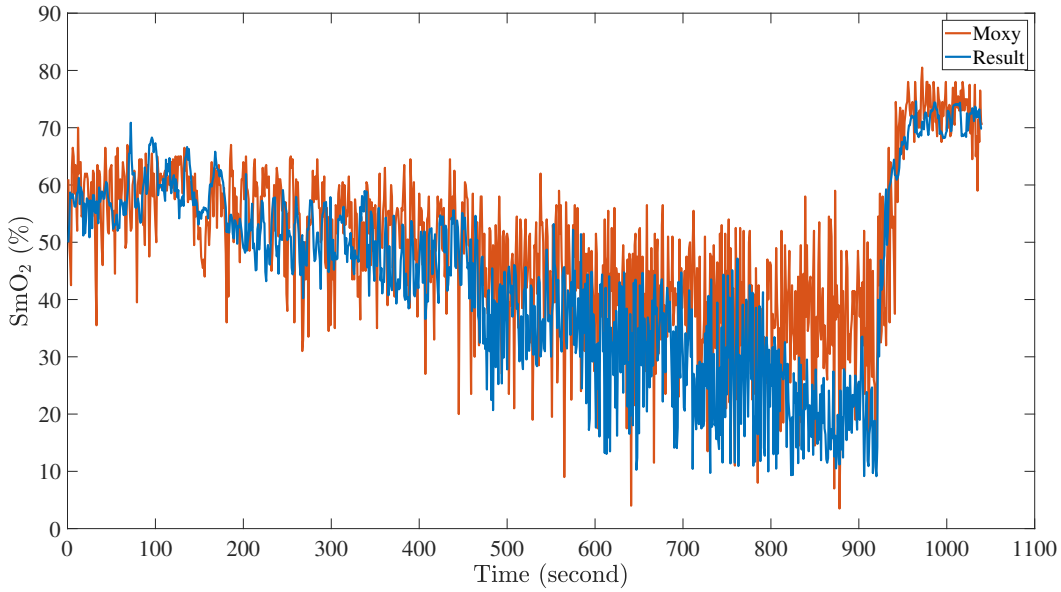

Figure 22: The SmO_2 results of a trainer under progression running procedure, compared with the results of Moxy monitor

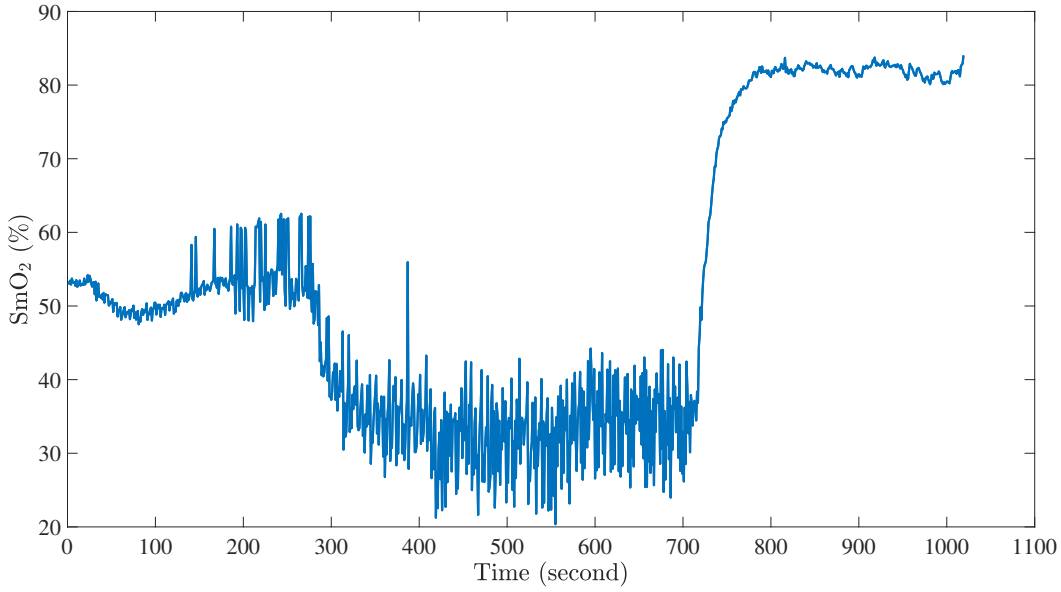

Figure 23: The SmO_2 results of a trainer who did not strictly follow the progression running procedure

still high. The same trend can be found in Fig. 21 and Fig. 23, except that the time interval of the running process of different testers was slightly different.

In addition to trends, absolute values of SmO_2 must also be analyzed. In Fig. 22, the value was around 60% when the trainer walked at the beginning, which was called the baseline value. The baseline value of different instruments could be various. From the summary of Yang et al. in [6], the possible baseline values of several instruments were between 50% and 80%. And for different individuals, the baseline values might be also different. The baseline value of the trainer of Fig. 21 was around 50%. And in Fig. 23, the baseline value was also around 50%. These values are within a reasonable range.

Before trainers had a rest, their calf muscles suffered several minutes ischemia. The SmO_2 value could as low as 20%, depends on the intensity of training. The results in Fig. 21 and Fig. 22 shows the SmO_2 values were around 20% during the ischemia. And the results in Fig. 23 shows the SmO_2 values were around 30% during the ischemia. In the study of Yang et al. in [6], the average SmO_2 at 5 minutes ischemia was $28.2\% \pm 14.0\%$. And in the study of DeBlasi et al. in [66], the average SmO_2 at 5 minutes ischemia was $33.8\% \pm 16.4\%$. Compared with these studies, our SmO_2 values are reasonable.

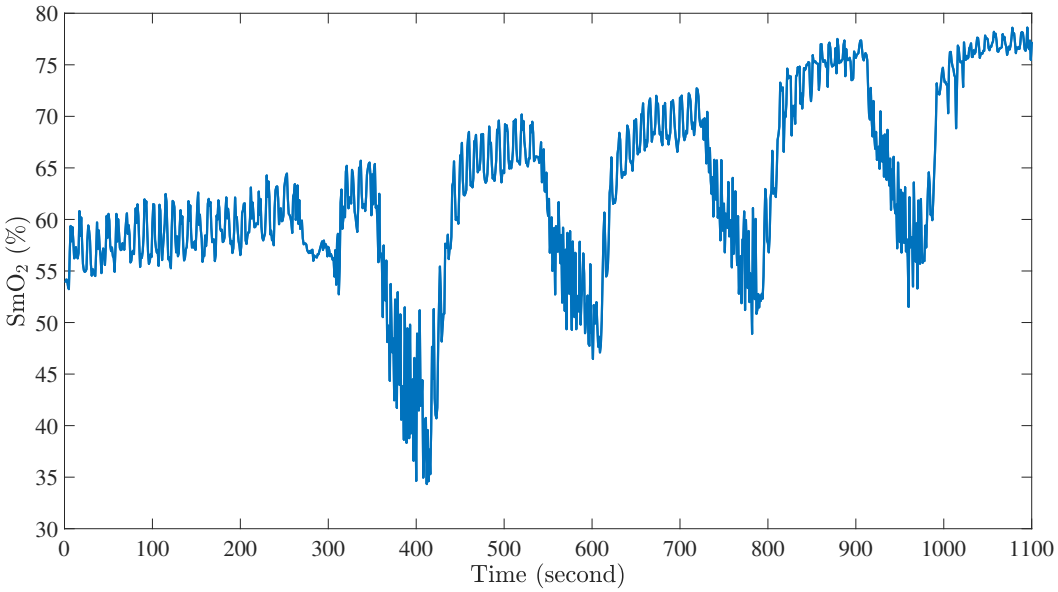

Figure 24: The SmO_2 results of a trainer under interval running procedure

In Fig. 21, 22, and 23, when the trainers changed from running to walking to have a rest, their SmO_2 values suddenly increased to around 80%, which was also consistent with the results in the study of Yang et al. in [6].

In summary, through the comparison with other researchers' results and analysis based on the training process, our results of SmO_2 values were reasonable.

The SmO_2 results of a complete measurement of the interval running described before is shown in Fig. 24. The baseline value was around 60%, which as a reasonable value. After several minutes warm up, the trainer started high speed running from 200 seconds so that the value of SmO_2 decreased. After running for 60 seconds, the trainer changed to walk for 120 second. During this recovery period, the SmO_2 first increased rapidly to a value that higher than before the start of this interval, then maintained this value until the running began in next interval. For each interval of running and recovery, the value of SmO_2 was possible to be higher than the previous interval due to the oxygen delivery was increasing with the training progressed. The curve of SmO_2 values and changes trend clearly showed that interval running could strengthen individual's aerobic capacity and cardiopulmonary function.

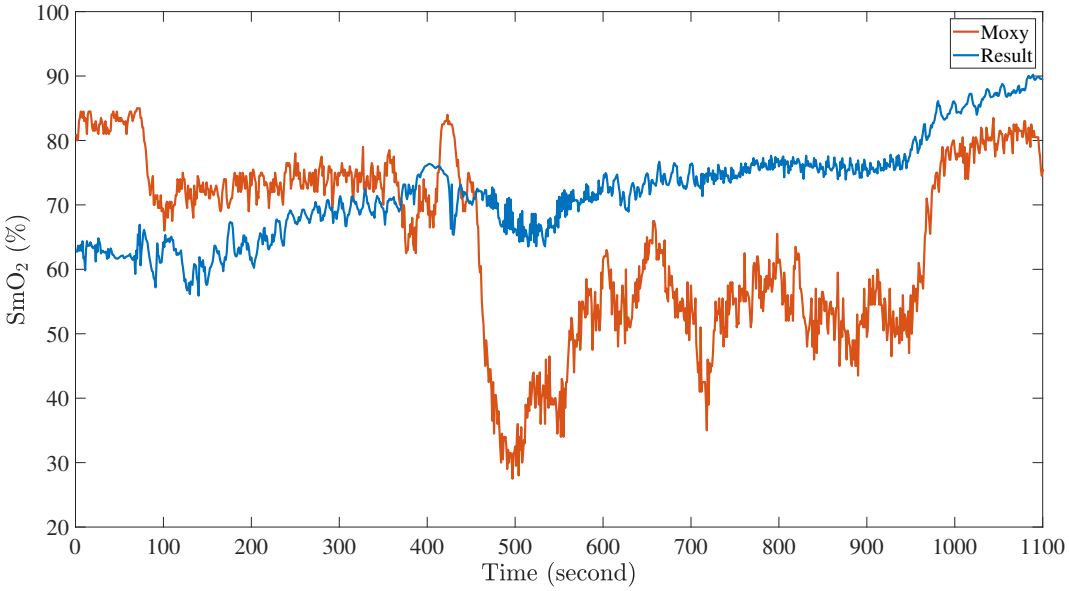

Figure 25: The unreliable SmO_2 results of a trainer who did not wear devices correctly and did not follow the interval running procedure

However, there also existed some unreliable results, as shown in Fig. 25. There are many reasons for unreliable results. First, due to the wearable device could easily move or fall off, the collected data would be unreliable if the trainer didn't wear it in the correct way. Then, the trainer may not wear the device in the proper place as instructed. For example, in running training, the device was wrongly worn on the front of the calf instead of the muscle in the back of the calf. Besides, for the prescribed training procedures, some individuals couldn't strictly follow or complete. In this case, the values of SmO_2 in each second should be correct but the curve of SmO_2 couldn't be interpreted by the specific prescribed training procedures.

The training procedure of the trainer in Fig. 23 should have been the progression running described before. However, this trainer didn't strictly follow the procedure and started to walk from 700 seconds. The value of each second in this result was correct. But it will be confused if explain this results with the specific procedure. It was recommended to follow the training process because experts can analyze the trainer's tolerant of exercise load with some specific training process.

The results in Fig. 25 was generated from the a training procedure which was not prescribed. The trainer should have been training the interval running procedure mentioned previously. It can be seen from the results of Moxy monitor and our device, he/she did not run according to the prescribed process. And the trainer did not wear two devices correctly, especially the Moxy monitor. Therefore, this data is useless for evaluating a training.

In addition, all measurements and calculations in this thesis were assumed to be at room temperature. However, the actual measurement temperature might be different. Besides, sweating during exercise will also affect the light absorption and scatting. These factors have affected the estimation accuracy.

To evaluate the training efficiency, it is important to get correct and precise results. Calculation results can only be useful if reliable data is measured. Therefore, a method is needed to judge whether the measurement data is reliable or not. One such method will be described in the next chapter.

Chapter 4

Fault Diagnostic and Integrated Application

During exercise, the wearable device could easily move or fall off. If the trainer does not wear the device correctly, the measured data will be unreliable. If athletes optimize their training based on incorrect SmO_2 results, it may lead to bad consequences, such as failure to achieve the training effect or injury due to over-training. Therefore, a method to judge whether the result is reliable is needed. In this chapter, machine learning classification methods were used to solve this problem. A fault diagnostic methodology is introduced based on data reliability classification and prediction by machine learning approach in the first part of this chapter.

In addition, since this is a set of algorithms made for wearable devices without a screen, the results generated after measurement and analysis need to be viewed on a computer or mobile phone. An integrated application can make it more convenient for users. Therefore, an application that integrated all these algorithms described previously was designed by Matlab App Designer. The second part of this chapter details the design and function of this application.

4.1 Fault Diagnostic by Machine Learning

As explained above, the reliability of SmO_2 results is important for users. To filter out the unreliable SmO_2 results, the best way is to find the key features that distinguish good quality from bad. By observing the figure of attenuation, under the same training process, it could be found that the attenuation of the reliable results has something in common and the attenuation of the unreliable results was usually different from reliable results. Therefore, a classification mechanism can be

established to classify data into reliable or unreliable categories.

There are two indicators to judge reliability of the measurement results. One is that the value of each second should be within a reasonable range. The other is that the trend of SmO_2 in a period of time is consistent with the current state of exercise.

To distinguish the results reliability, the most direct method was to observe the original data collected from the device. However, the original data included the measuring data of one source and two detectors, which was too complicated to find their features. The SmO_2 results were generated from the light attenuation by non-linear least squares fitting. So it was suitable to use the light attenuation of each test as the data for classification.

Because attenuation was high-dimensional data, it was difficult to observe its features with the naked eyes and to judge its reliability with a single judgement condition. It is well known that using machine learning can solve a classification problem well. Therefore, this data reliability classification problem can also be solved by machine learning.

4.1.1 Classification in Machine Learning

Machine learning is an application of artificial intelligence that enables the system to automatically learn and improve from experience without the need for explicit programming. Classification is a type of supervised learning. In statistics, classification is the problem of determining which group of categories a new observation belongs to. It is based on learning a training data set containing observation data whose category membership is known. There are two types of classification problem: binary and multiclass. Binary classification is the task of dividing the elements of a collection into two groups according to classification rules. And multiclass classification is a problem of dividing the elements of a collection into one of three or more classes.

There are several types of classification algorithms, depending on the data set used. The following are the four most common classification algorithms in machine learning.

Logistic Regression

Logistic regression is a calculation used to predict a binary outcome. It should only be used when the target variable belongs to a discrete category. Logistic regression is named for the function

used at the core of the method, the logistic function, also called the sigmoid function:

$$g\left(z\right)=\frac{1}{1+e^{-z}} \tag{64}$$

Suppose that $y\in\{0,1\}$, and the hypothesis of logistic regression tends it to limit the cost function between 0 and 1, which is represented as $h_{\Theta}\left(x\right)\in[0,1]$. The hypothesis can be written as

$$h_{\Theta}\left(x\right)=g\left(\Theta^{T}x\right)=\frac{1}{1+e^{-\Theta^{T}x}} \tag{65}$$

In a binary classification problem, the probability of two classes can be represented as

$$\begin{aligned} P\left(y=1|x;\Theta\right)&=h_{\Theta}\left(x\right)\\ P\left(y=0|x;\Theta\right)&=1-h_{\Theta}\left(x\right) \end{aligned} \tag{66}$$

which can also be written as

$$P\left(y|x;\Theta\right)=h_{\Theta}\left(x\right)^{y}\left(1-h_{\Theta}\left(x\right)\right)^{1-y} \tag{67}$$

A cost function of log likelihood was created as follows:

$$l\left(\Theta\right)=\log L\left(\Theta\right)=\sum_{i}^{m}y^{(i)}\log h_{\Theta}\left(x^{(i)}\right)+\left(1-y^{(i)}\right)\log\left(1-h_{\Theta}\left(x^{(i)}\right)\right) \tag{68}$$

which can be used in gradient ascent method to find the maximum likelihood:

$$\begin{aligned} \frac{\partial}{\partial\Theta_{j}}l\left(\Theta\right)&=\sum_{i=1}^{m}\left(y^{(i)}-h_{\Theta}\left(x^{(i)}\right)\right)x_{j}^{(i)}\\ \Theta_{j}&:=\Theta_{j}+\alpha\sum_{i=1}^{m}\left(y^{(i)}-h_{\Theta}\left(x^{(i)}\right)\right)x_{j}^{(i)} \end{aligned} \tag{69}$$

When the inputs are passed through a prediction function, it will return a probability score between 0 and 1, which can used to generate the class.

Logistic regression is a widely used technique because it is very efficient, without requiring too many computational resources. It works better when removing attributes that are not related to the output variables and attributes that are very similar to each other. A disadvantages is that logistic regression can not solve non-linear problems since it's decision surface is linear. Another disadvantages is the high reliance on a proper presentation of data.

Naive Bayes Classifier

Naive Bayes classifier was one of the first algorithms used for machine learning. It is suitable for binary and multiclass classification and allows for making predictions and forecast data based on historical results.

For both binary and multiclass classification, given the data $x_i \in \{1, 2, \cdots, k\}$, the probability can be represented as

$$P(x|y) = \prod_{i=1}^{n} P(x_i|y) \tag{70}$$

where n represents the number of features, which is large.

The classification is conducted by deriving the maximum posterior which is the maximal $P(y|x_i)$ with the above assumption applying to Bayes' theorem:

$$arg\max P(y|x) = arg\max_{y} \frac{P(x|y)\, P(y)}{P(x)} \tag{71}$$

Naive Bayes assumes that the attributes are conditionally independent. This assumption greatly reduces the computational cost by only counting the class distribution. However, Naive Bayes is not valid in most cases since the attributes are dependent.

K-Nearest Neighbors

K-nearest neighbors (k-NN) is an algorithm that uses training datasets to find the k closest relatives in future examples. The k-NN algorithm assumes that similar things exist very closely to each other. The procedure of k-NN algorithm can be described as follows:

1. Load the data with labels and initialize k to chose the number of neighbors.
2. For each example in the data, calculate the distance between the query example and the current example from the data, and add the distance and the index of the example to an ordered collection
3. Sort the ordered collection of distances and indices in ascending order.
4. Pick the first k entries from the sorted collection and get their labels.
5. Determine the number of occurrences of the classes of the first k entries.
6. Return the class with the highest occurrence of the first k entries as the predicted classification of the points to be classified.

It should be noted that the distance metric using in k-NN for continuous variables is usually Euclidean distance and for discrete variables is usually Hamming distance. Choosing a proper value for k is the most important decision in k-NN. The best choice of k depends upon the data. Small value of k can classify the data more distinct, but it may lead to over-fitting. Larger values of k reduces effect of the noise, but make boundaries between classes less distinct [67] .

K-nearest neighbors is a simple and non-parametric algorithm, so it does not make assumptions about the data distribution. It stores the training datasets and learns from them only at the time of making real time predictions. However, the k-NN algorithm is computationally expensive because it searches new points in the nearest neighbors during the prediction. It doesn't work well with high dimensional data because with large number of dimensions, it becomes difficult to calculate the distance in each dimension. Besides, the storage requirements are high since k-NN must store all data points, while its accuracy is sensitive to noisy data, missing values and outliers.

Support Vector Machine

A support vector machine (SVM) is a discriminative classifier defined by a separating hyperplane [68]. In other words, given the labeled training data, the algorithm will output the optimal hyperplane that classifies the new example. This optimal hyperplane is the decision boundary, which should maximize the margins from both classes. In the SVM algorithm, each data item is ploted as a point in a p-dimensional space, where p is number of features.

Supposed that the given a training dataset of n points is in the form of

$$(\mathbf{x}_1, y_1), \cdots, (\mathbf{x}_n, y_n) \tag{72}$$

where y_i indicates the class of the point $\mathbf{x}_i$, which is either 1 or -1. And each $\mathbf{x}_i$ is a p-dimensional real vector. There exists a hyperplane that divides the group of points $\mathbf{x}_i$ for which $y_i = 1$ from the group of which $y_i = -1$. The optimal hyperplane maximizes the distance between the hyperplane and the nearest point from two groups, as shwon in Fig. 26. Any hyperplane can be written as the set of points $\mathbf{x}_i$ satisfying

$$\mathbf{w} \cdot \mathbf{x} - b = 0 \tag{73}$$

where $\mathbf{w}$ is the normal vector to the hyperplane, and $\frac{b}{\|\mathbf{w}\|}$ determines the offset of the hyperplane from the origin along the normal vector $\mathbf{w}$.

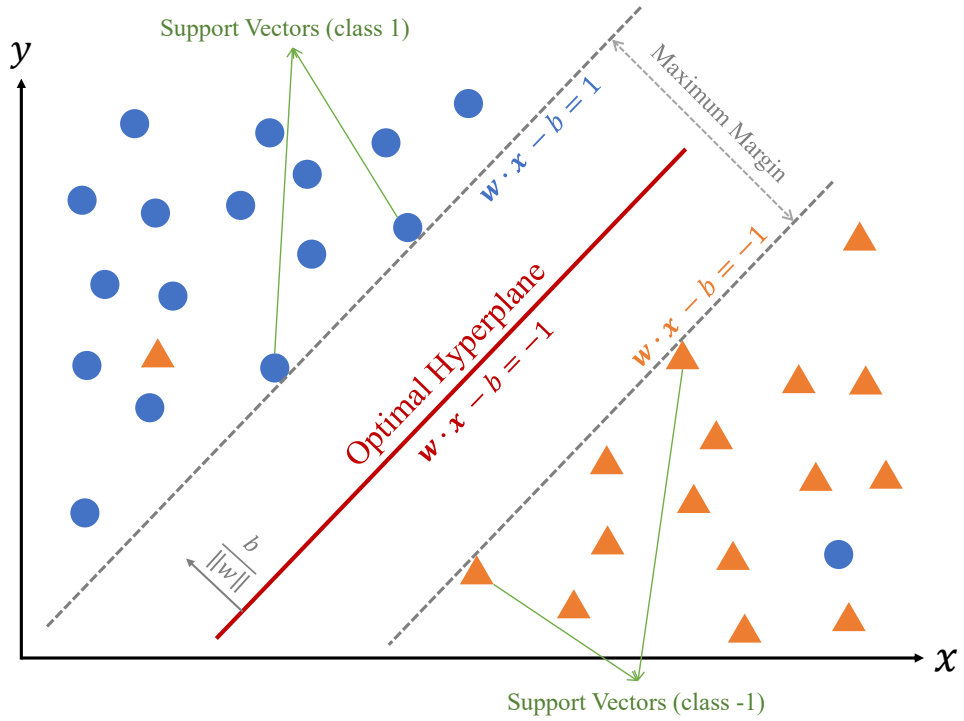

Figure 26: Maximum-margin hyperplane and margins for an SVM trained with samples from two classes.

If the training data is linearly separable, two parallel hyperplanes that separate the two classes of data can be found, so that the distance between them is as large as possible. As shown in Fig. 26, although there are some outliers in the data, it can still find the hyperplane that has the maximum margin by minimizing equation (77), which is called soft-margin SVM. The region bounded by these two hyperplanes is called the "margin", the hyperplane that lies halfway between them is the optimal hyperplane. These hyperplanes can be described as

$$\begin{aligned} \mathbf{w} \cdot \mathbf{x} - b &= 1 \\ \mathbf{w} \cdot \mathbf{x} - b &= -1 \end{aligned} \tag{74}$$

For each data point $\mathbf{x}_i$, it satisfies $\mathbf{w} \cdot \mathbf{x}_i - b \geq 1$ if $y_i = 1$, and $\mathbf{w} \cdot \mathbf{x}_i - b \leq -1$ if $y_i = -1$. These two inequalities can also be written as

$$y_i \left(\mathbf{w} \cdot \mathbf{x}_i - b \right) \geq 1, \text{ for all } 1 \leq i \leq n \tag{75}$$

It can be found from equation (74) that the distance between two hyperplanes is $\frac{2}{\|\mathbf{w}\|}$. Therefore, the problem of maximizing the distance between two hyperplanes can be replaced by the problem of minimizing $\|\mathbf{w}\|$ subject to equation (75).

To extend SVM to cases in which the data are not linearly separable, the hinge loss function in equation (76) is used.

$$\max\left(0, 1 - y_i\left(\mathbf{w} \cdot \mathbf{x}_i - b\right)\right) \tag{76}$$

The hinge loss function is 0 if the constraint in equation (75) is satisfied, which means $\mathbf{x}_i$ lies on the correct side of margin. For data on the wrong side of the margin, the function's value is proportional to the distance from the margin.

The goal of the optimization becomes to minimize the following equation:

$$C\sum_{i=1}^{n}\max\left(0, 1 - y_i\left(\mathbf{w} \cdot \mathbf{x}_i - b\right)\right) + \|\mathbf{w}\| \tag{77}$$

where C is a regularization parameter that controls the trade-off between maximizing the margin and minimizing the training error. A large value of C will lead to low bias but high variance. On the contrary, a small value of C will cause high bias but low variance. Too large value of C may cause over-fitting, while too small value of C may cause under-fitting.

SVM can also be extended into nonlinear classification problems by applying the kernel trick [69]. The resulting algorithm is similar in form to the linear algorithm. The difference is that each dot product is replaced by a nonlinear kernel function. Some common used kernels are listed as follows:

- Polynomial:

$$k\left(\mathbf{x}_i, \mathbf{x}_j\right) = \left(\mathbf{x}_i \cdot \mathbf{x}_j + r\right)^d \tag{78}$$

  where where d is specified by parameter degree.

- Gaussian radial basis function (RBF):

$$k\left(\mathbf{x}_i, \mathbf{x}_j\right) = \exp\left(-\gamma\|\mathbf{x}_i - \mathbf{x}_j\|^2\right) \tag{79}$$

  where $\gamma > 0$, which is sometimes parametrized using $\gamma = \frac{1}{2\sigma^2}$. γ defines how much influence a single training example has. The larger γ is, the closer other examples must be to be affected.

- Hyperbolic tangent:

$$k\left(\mathbf{x}_i, \mathbf{x}_j\right) = \tanh\left(\kappa\mathbf{x}_i \cdot \mathbf{x}_j + r\right) \tag{80}$$

  where $\kappa > 0$ and $r > 0$.

In general, SVM works relatively well when there is a clear margin of separation between classes. The kernel trick is real strength of SVM. With the introduction of kernel, input data can be converted into high dimensional data to avoid the assumption of linearly separability. SVM is very good when people has no idea on the data because it can be used for the data that is not regularly distributed and has unknown distribution. It works well with even unstructured and semi structured data like text, images and trees. Besides, SVM models have generalization in practice. Generally it does not suffer from over-fitting if the parameters C and γ (in the case of a RBF kernel) are appropriately chosen.

However, there are also some disadvantage of SVM. The biggest limitation of the support vector approach lies in choice of the kernel. Besides, algorithmic complexity and memory requirements of SVM are very high. So it takes a long training time on large datasets.

4.1.2 Classification of Light Attenuation

There are three main steps for solving a classification problem. First, in supervised learning, the data should be labelled properly. And for some of the learning algorithms, preprocessing the data can lead to a more accurate result. Then, determining the parameters of the selected model is the most important step because the parameters determine the degree of fit of the model. Failure to choose appropriate parameters will lead to over-fitting or under-fitting. Finally, train the model using the training datasets and evaluate it by several aspects using both training and testing datasets.

Preprocessing and Labelling Data

For classification in machine learning, sending raw data through a model would cause certain errors. Preprocessing techniques are always applied to rea-world data before training the model. Two methods are usually well known for rescaling data, normalization and standardization. Normalization scales all numeric variables in the range [0,1] and two possible formula are given by

$$x_{scale} = \frac{x - x_{min}}{x_{max} - x_{min}} \tag{81}$$

and

$$x_{scale} = \frac{x - x_{mean}}{x_{max} - x_{min}} \tag{82}$$

And standardization will transform the data to have zero mean and unit variance, for example using the equation below:

$$x_{standard} = \frac{x - \mu}{\sigma} \tag{83}$$

where μ is the mean of data and σ is the variance.

Both of these techniques have their drawbacks and limitations. Generally, most of data sets have outliers. With normalization, the normal data will certainly be scaled to a very small value because of these outliers. And standardization might behave badly if the individual features do not look like standard normally distributed data, which is Gaussian with zero mean and unit variance.

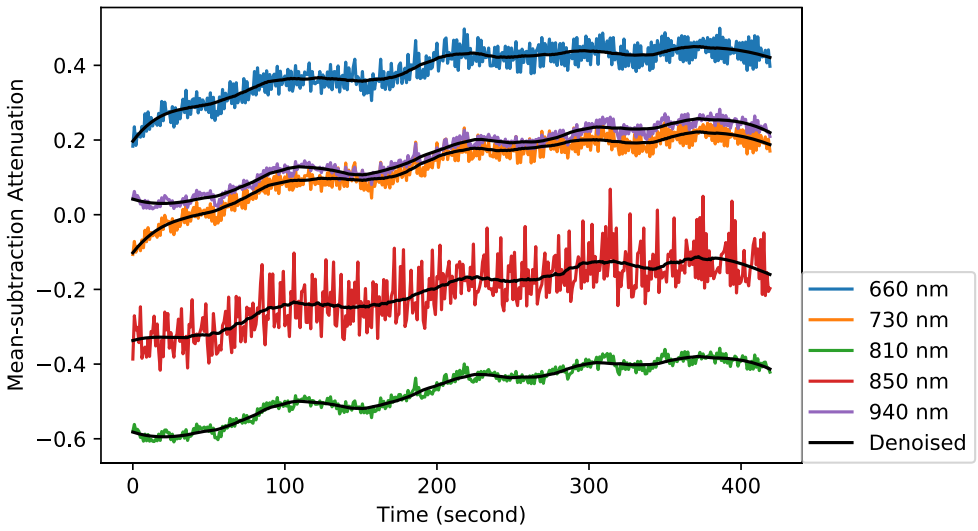

Figure 27: Mean-subtraction and denoised attenuation of five wavelengths in running status

For the classification of light attenuation, it is important to preserve not only the relative relationships of the five wavelengths, but also the trend information over a period of time. So none of the methods mentioned above can be used. Therefore, a simple mean-subtraction, which described in equation (84) was applied to the orthogonal attenuation.

$$x_{new} = x - x_{mean} \tag{84}$$

Due to the variance of attenuation at each wavelength was large, it was also necessary to apply a denoise to the mean-subtraction data. An example of preprocessed data is shown in Fig. 27.

In total, 33 independent tests of different individuals were done in two training procedures, of which 21 were done by progression running and 12 were done by interval running. The measuring

data collected from the progression running was used to train and test the classification model. For classification problem, the data should be labeled first. There are two principles to label the data. The first principle is to compare the results with Moxy monitor, if it is similar, the results can be labeled as reliable. For the data that didn't have a comparison with Moxy monitor, the reliability can be labeled by the reasonable value and trend of the corresponding movement status. Due to improper wearing of the device or other reasons, there are 11 tests results which were determined as unreliable and the other 10 tests were reliable. For implementing classification in Python, the class of reliable data was labelled as 1 and the class of unreliable data was labelled as -1.

To evaluate the results both in each second and in a short period, the data should be divided by training status, because in different training status, the value and the trend are different. For example, in the warm up status, the values of SmO_2 should be in the range from 50% to 80% and should stay relatively stable. While in the running status, the values of SmO_2 may be lower than 50% and may have a trend of decrease. Therefore, the classification should be done in each status. In this thesis, two training status was divided, warm up and running.

We divided 10 seconds as a period to evaluate the results. For warm up status in progression running procedure, there were about 180 seconds for each individual, and some individuals had more. Each dataset was divided into several pieces of 10 seconds. After splitting and labelling, there were 140 samples of class 1 (reliable) and 135 samples of class -1 (unreliable). These samples were shuffled and randomly composed the training set and testing set for classification of warm up status. And for running status, there were about 400 seconds for each test and they were also split into pieces of 10 seconds. Among them, 507 samples were class 1 and 448 samples were class -1. Therefore, each sample is the preprocessed attenuation of 5 wavelengths in 10 seconds, which is 50 dimensions. These samples were also shuffled and randomly composed the training set and testing set for classification of running status.

Model and Parameters

Four classification methods and their advantages and disadvantages were described previously. For classifying light attenuation, each sample is 50 dimensions and there were only 275 samples in warm up status. Therefore, it is a high-dimension problem with a small number of datasets. In this case, support vector machine (SVM) with Gaussian radial basis function (RBF) kernel would

be the best choice.

As mentioned before, the parameters in SVM, C and γ, are highly influence the performance of classifier. C behaves as a regularization parameter in the SVM, which defines how far the influence of a single training example reaches. If C is a large value, training accuracy will be high but the margin will be small. γ can be regarded as the inverse of the radius of influence of samples selected by the model as support vectors. If γ is too large, the radius of the area of influence of the support vectors only includes the support vector itself. This will lead to overfitting that even a small regular term C cannot prevent.

To find the relatively best parameters, the grid search method is applied. As its name suggests, it is an algorithm that applies two parameters within a given range and searches for the best result, which can be visualized as a heatmap as shown in Fig. 28. The lighter the color in the grid, the higher the accuracy of the prediction using the parameters in the current grid. It was implemented by the sklearn.model_selection.GridSearchCV function of scikit-learn [70] in Python. With this function, we can get the best set of parameters in the given range without visualization.

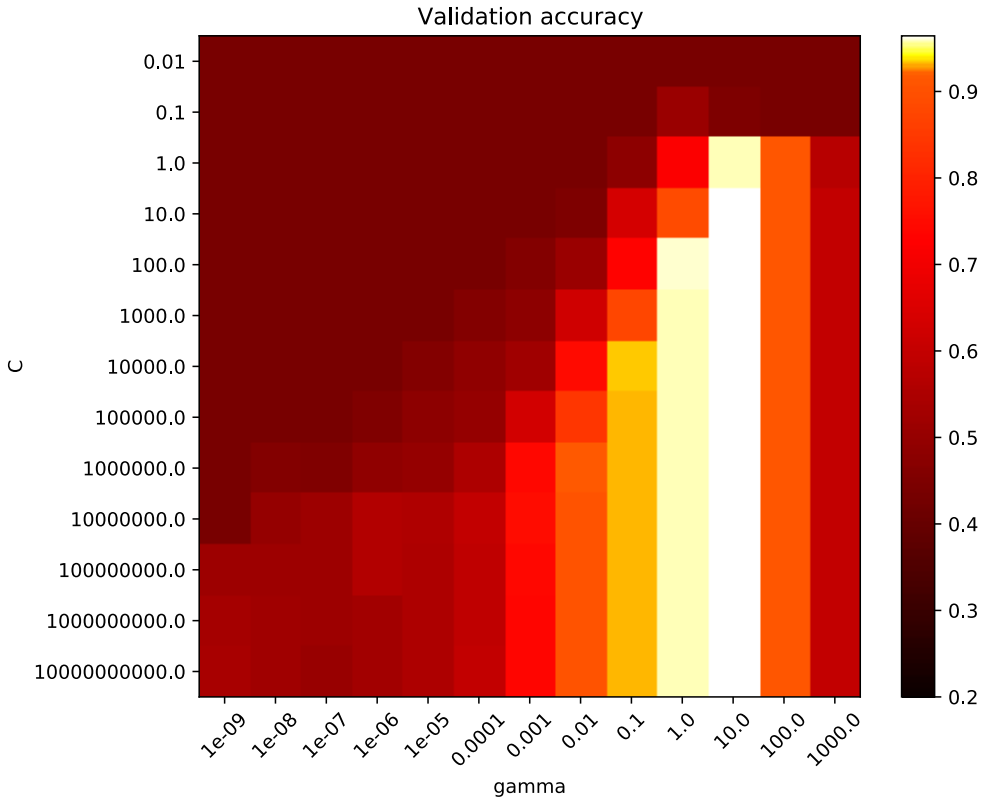

Figure 28: A heatmap of the classifier's cross-validation accuracy as a function of C and γ

Evaluation

An important metric to evaluate a classifier is the accuracy, which is defined as

$$\text{accuracy}\,(y, \hat{y}) = \frac{1}{n}\sum_{i=0}^{n-1} 1\,(\hat{y}_i = y_i) \tag{85}$$

where $1\,(x)$ is the indicator function, n is the number of samples, $\hat{y}_i$ is the predicted value of i-th sample, and y_i is the corresponding true value.

To evaluate a model, two curves were used in this study, cross-validation learning curve and receiver operating characteristic (ROC) curve.

Learning the parameters of a classifier and testing it on the same data is a methodological mistake. A model would have a perfect score with training data but would fail to predict anything useful on unseen data. To avoid this situation, it is necessary to hold out part of the available data as a testing set. Using different training and testing sets allocations will cause instability in accuracy values. Therefore, it is better to use the average accuracy of different allocations of training and testing sets to evaluate classifier performance. Cross-validation is an approach that measures the average of accuracy based on several groups of training and testing sets. It is often used to assess whether the choice of parameters in the model is appropriate. K-fold cross-validation splits the training sets into k smaller sets. The model is trained using $k - 1$ of the folds as training sets and the resulting model is validated on the remaining part of the data. This procedure would loop k times until each group of data has been used for validation. Another approach of cross-validation is to randomly generate a certain percentage of training samples to train the model and use other samples as testing data to evaluate it. This procedure should loop several times to calculate the average accuracy. Cross-validation is computationally expensive, but it does not waste too much data, which is a major advantage in the problem with small sample sizes.

The cross-validation learning curve uses the number of data sets from small to large to train and evaluate the model. That curve shows the effect of the number of training examples used in cross-validation on accuracy.

An ROC curve is a graph showing the performance of a classification model at all classification thresholds. This curve plots two parameters, true positive rate and false positive rate. True positive rate (TPR) represents a proportion of those samples truly belong to class 1 that are correctly

identified as class 1, and is defined as

$$TPR = \frac{TP}{TP + FN} \tag{86}$$

False positive rate (FPR) is calculated as the ratio between the number of samples in class -1 wrongly categorized as class 1 and the total number of actual samples of -1, which is defined as

$$FPR = \frac{FP}{FP + TN} \tag{87}$$

AUC measures the entire two-dimensional area underneath the entire ROC curve. The value of AUC represents the probability that the model can distinguish between class 1 and class -1. The AUC of a good model is close to 1, which means it has a good measure of separability. A poor model with AUC near 0 means it has the worst measure of separability, which means all predictions are opposite. When AUC is 0.5, it means that the model does not have any classification ability and just randomly guess.

4.1.3 Results

The classification was done separately in warm up and running status.

Warm up

To find the proper value of C and γ for SVM classifier, a heatmap of the classifier's cross-validation accuracy as a function of C and γ was plot, as shown in Fig. 29. From the heatmap, it is clear that when γ and C both larger than 2.15, the accuracy of the classifier was higher than 90%. As mentioned before, the best values can be found by GridSearchCV function. When $\gamma = 4.6$ and $C = 6$, the performance of the classifier was the best.

The learning curve is shown in Fig. 30. With the increasing number of training samples, the cross-validation accuracy also increased. For each validation step, 80% of samples were randomly picked to train the model and others were used for testing. Even the total number of training samples were not large, the accuracy was still higher than 95%. This indicated that the selection of parameters was successful.

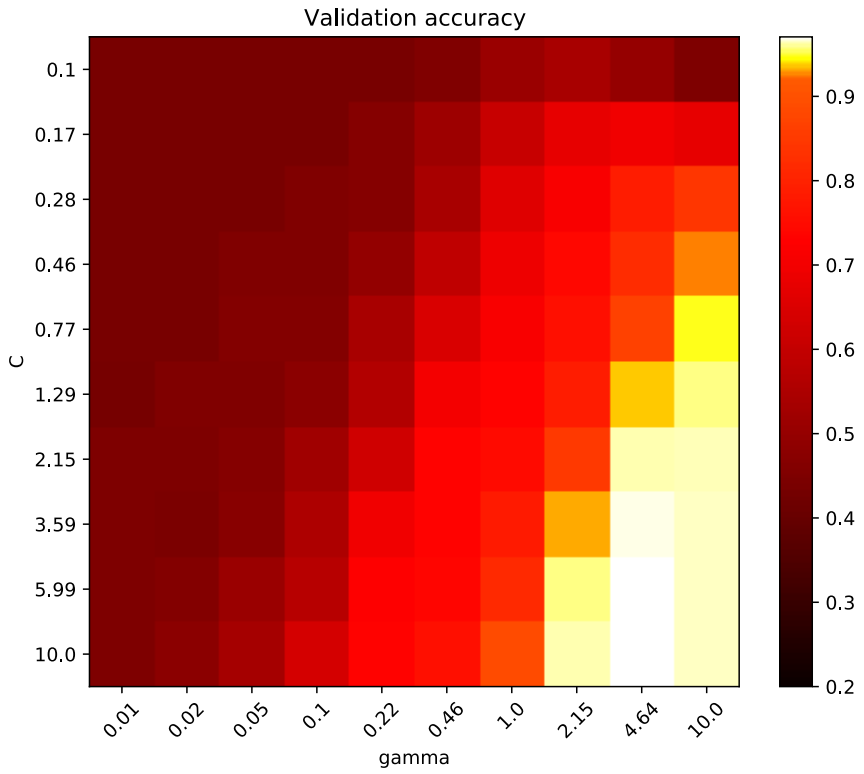

Figure 29: A heatmap of the classifier's cross-validation accuracy as a function of C and γ for the classification in warm up status

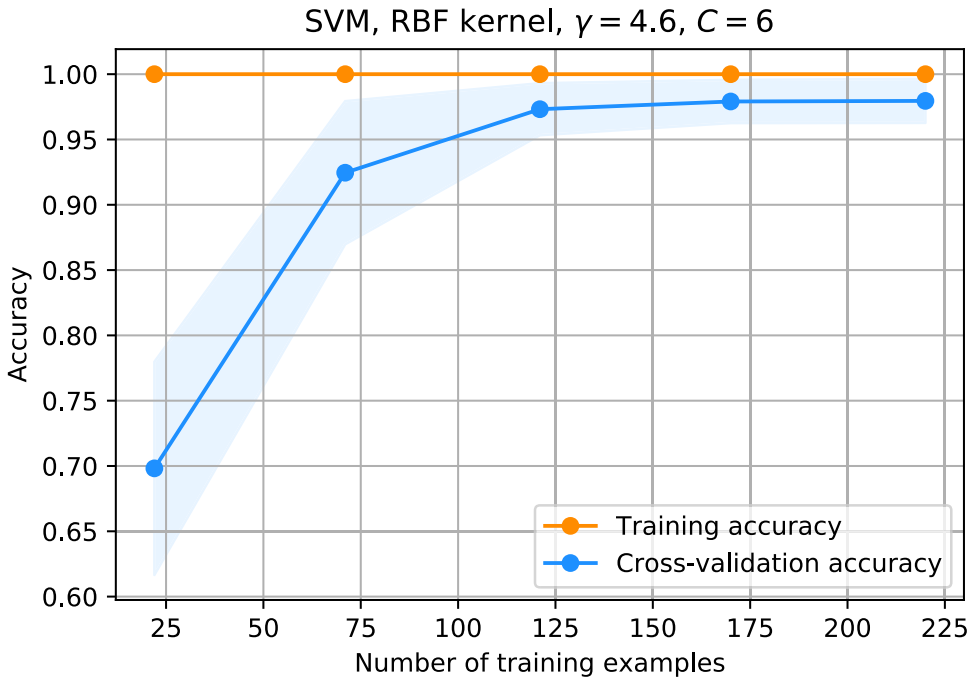

Figure 30: Learning curve of cross-validation accuracy in warm up status

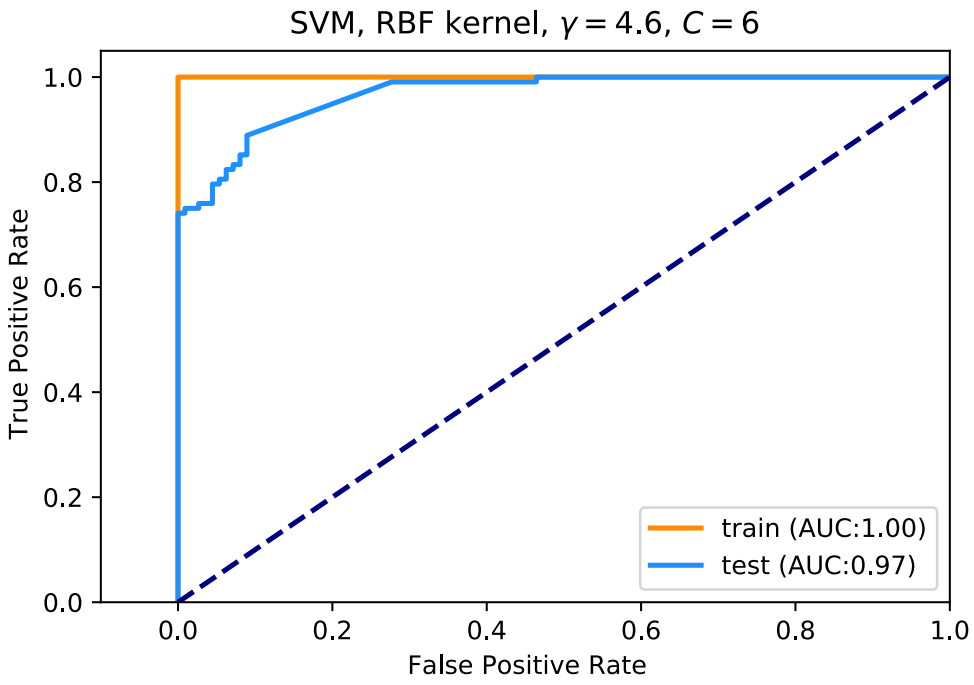

Figure 31: ROC curve of the model with the best parameters in warm up status

Fig. 31 shows the ROC curve and corresponding AUC both in training and testing with the best γ and C values. The performance of this classifier was great because testing AUC was 0.97, which means that the probability of making the correct decision was 97%.

Running

For running status, a heatmap of the classifier's cross-validation accuracy as a function of C and γ is shown in Fig. 32. The values of C and γ can choose from the corresponding values of the high accuracy grids in light color. And the calculated best value was $\gamma = 2.15$ and $C = 0.78$.

Fig. 33 shows the learning curve of cross-validation accuracy in the best values of γ and C. Both training and the cross-validation accuracy increased with the increasing number of training samples. For each validation step, 50% of samples were randomly picked to train the model and others were used for testing. The cross-validation accuracy was near 100%, which indicated that the parameter selection was successful.

With the best γ and C, it can be found from the ROC curve in Fig. 34 that both training and testing cuerves are far away from the diagonal. And 0.97 of testing AUC represents that this

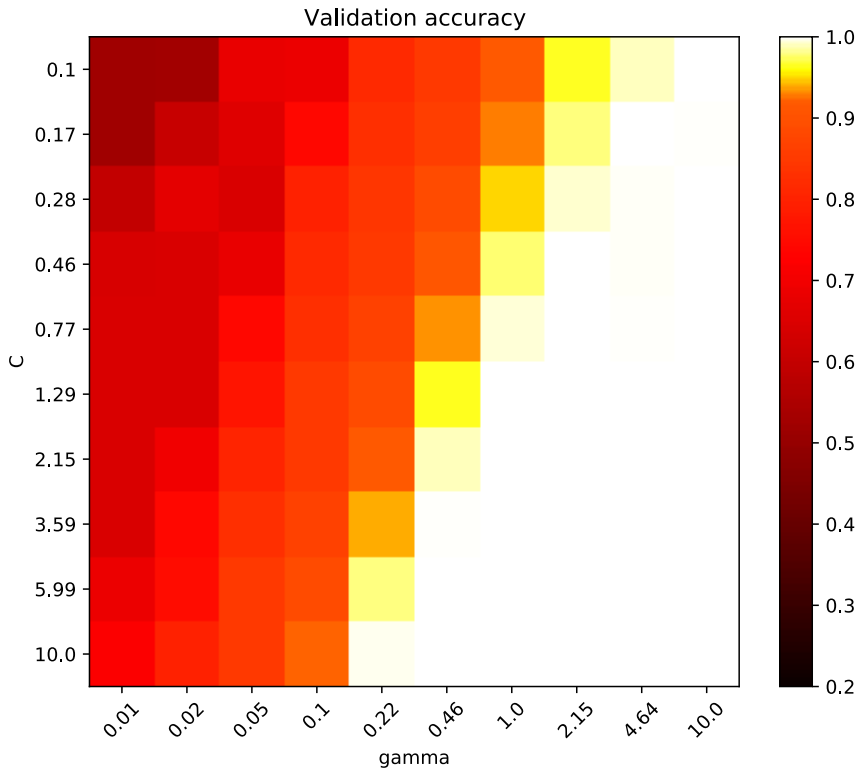

Figure 32: A heatmap of the classifier's cross-validation accuracy as a function of C and γ for the classification in running status

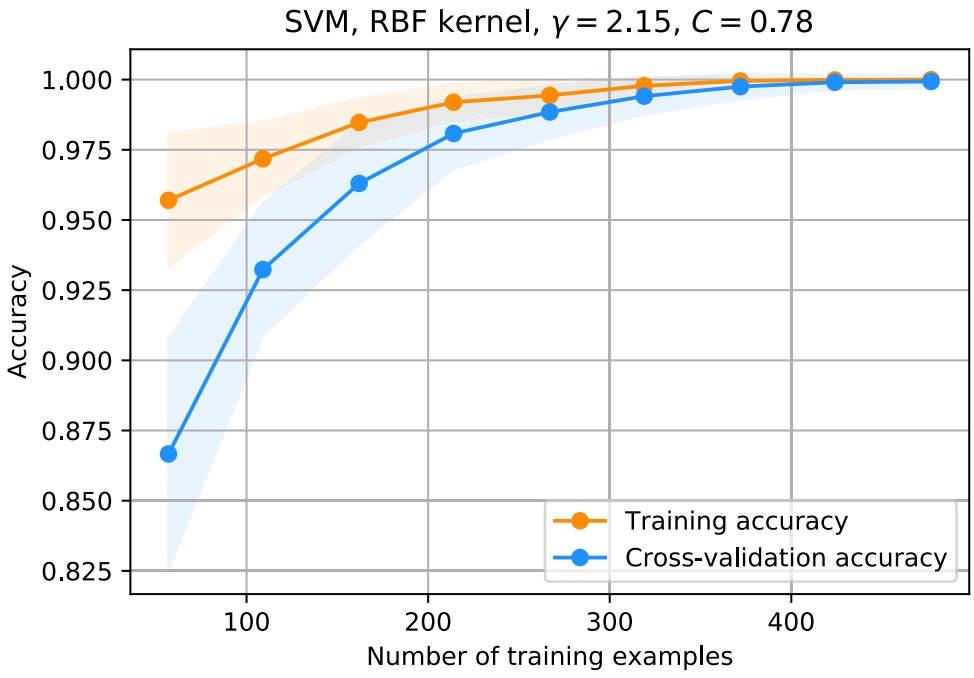

Figure 33: Learning curve of cross-validation accuracy in running status

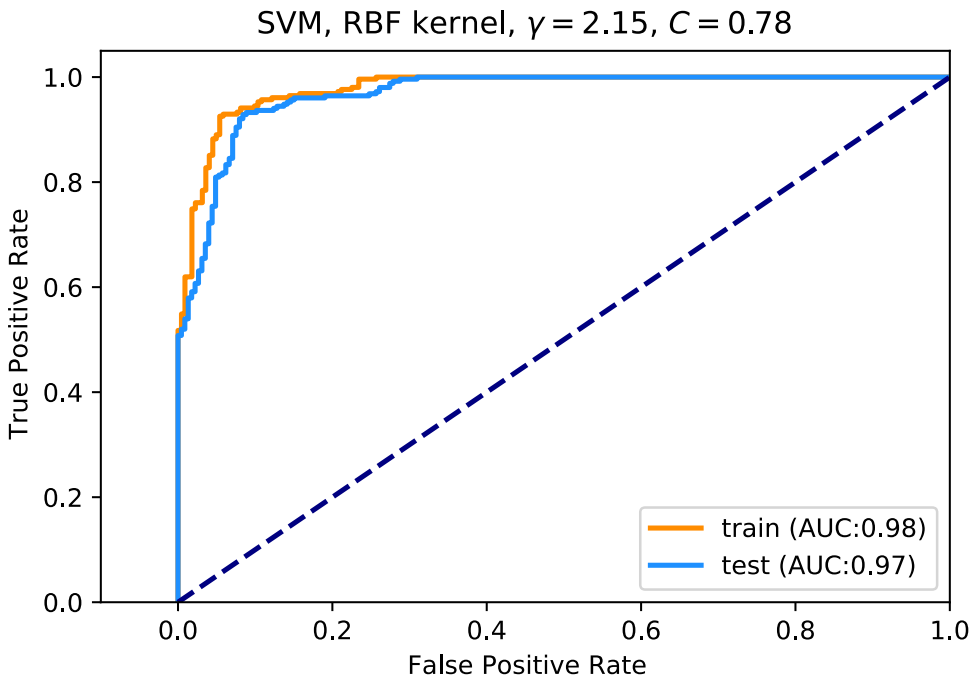

Figure 34: ROC curve of the model with the best parameters in running status

classifier works very well.

Conclusion

With the classification of light attenuation, the reliability of corresponding SmO_2 results can be predicted. These good evaluation results indicate the possibility of fault diagnostic in SmO_2 measurement. However, more *in vivo* have to be collected to make the classifiers more robust. With the increasing of datasets, the values of C and γ will be relatively small, so that overfitting can be avoided with high accuracy.

4.2 SmO_2 Calculation Application

As mentioned before, since the wearable devices does not have screen, the measurement results should be viewed on computer. For a better user experience, an application that integrated all these algorithms described previously was designed by Matlab App Designer.

4.2.1 Matlab App Designer

Matlab App Designer integrates two primary tasks of app building: laying out the visual components of a graphical user interface (GUI) and programming app behavior. It is the recommended environment for building apps in Matlab. It allows developers to distribute the application by packaging the application into the installer file directly from the App Designer toolbar, or by creating a standalone desktop or web application. There are two steps to develop an application in Matlab App Designer: designing a user interface and defining app behavior.

Matlab App Designer provides a grid layout manager to organize the user interface, and provides automatic reflow options to make the application detect and respond to changes in screen size. The Component Library allows developers to easily drag and drop components into the user interface, as shown in Fig. 35. It automatically generates the object-oriented code that specifies

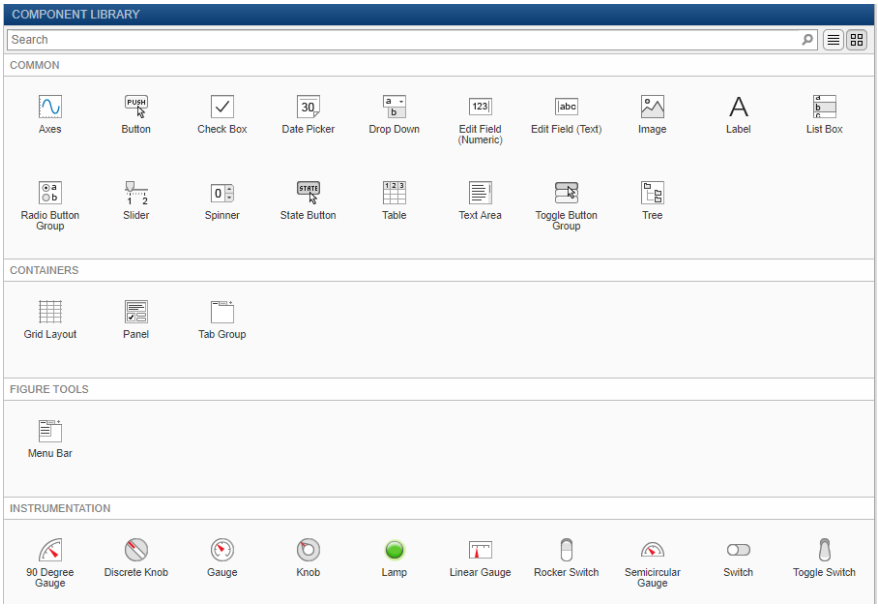

Figure 35: App Designer's component library

the app's layout and design.

To define the functionality of application, we use the integrated version of the Matlab Editor, and Code Analyzer can automatically check for coding problems. After dropping components into the user interface, component callbacks and custom mouse and keyboard interactions, which execute when a user interacts with the application, can be added by writing object-oriented code based on Matlab functions.

4.2.2 Application Interface and Functionality

An application of SmO_2 calculation and data quality classification was designed using Matlab App Designer. It included both results display and a simulation of real-time measurement. There are several user interacts functions.

The main interface of this application is shown in Fig. 36. User clicked the file selection

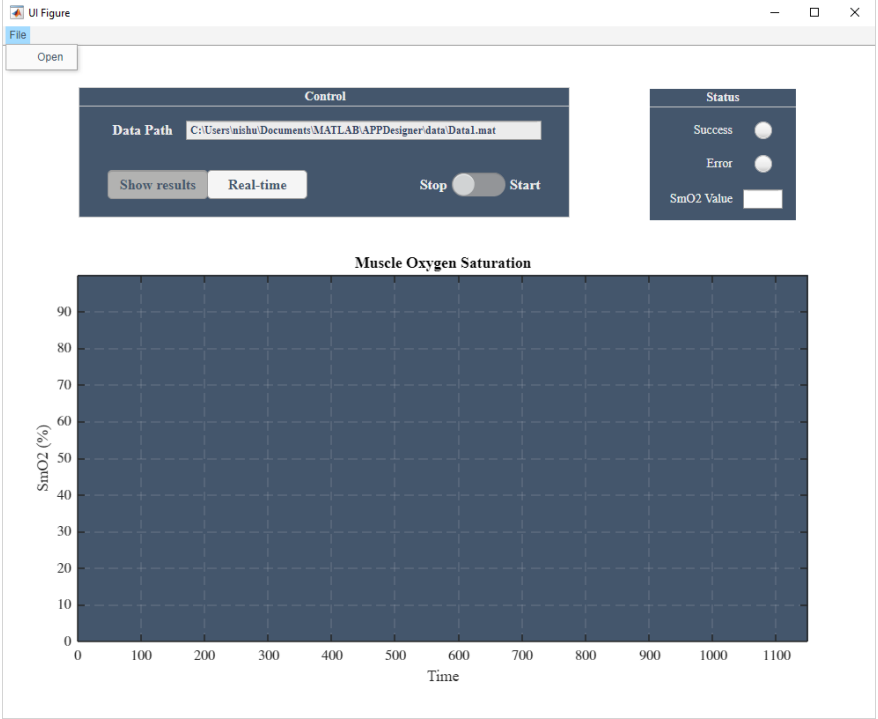

Figure 36: Main interface of SmO_2 calculation application

menu in the upper left corner, and a system file selection dialog box appeared, where the user was required to select a data file. After selection, the chosen file path would show in the text box at the top. The button of real-time and show results modes represented whether the measurement results were shown in real-time or not. When one button was selected, the other was automatically unavailable. The switch on the right was where the user controlled the start and stop. If user didn't choose file before switched to start, a suggestion of choosing file would show in the text box of file path, as shown in Fig. 37. After choosing file and selecting mode, the switch can be switched to start to process the data.

In the show results mode, a message was showed up to indicate the progress of data processing, as shown in Fig. 38.

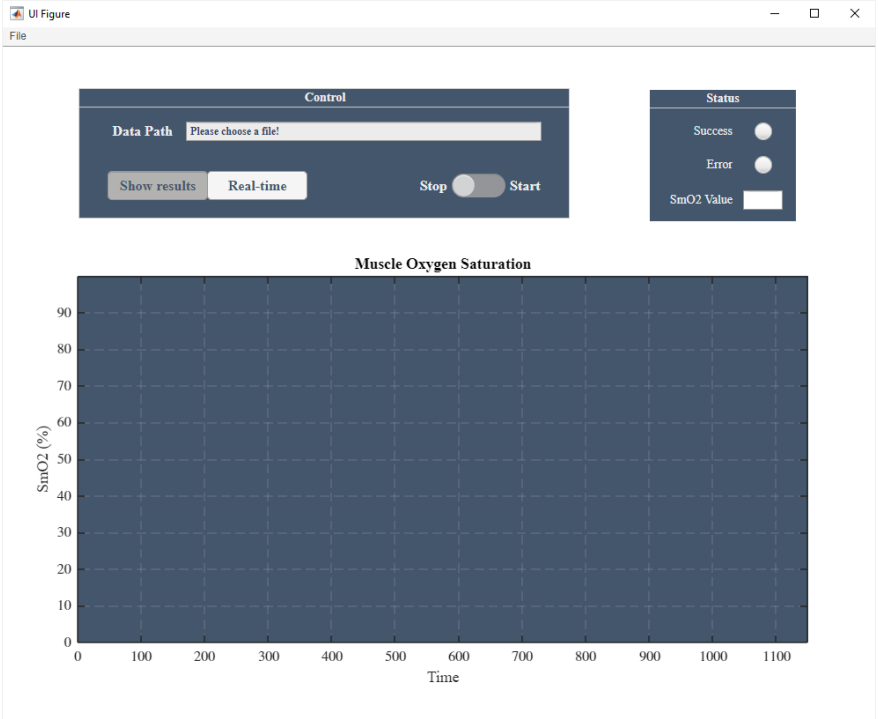

Figure 37: Display suggestion for selecting file

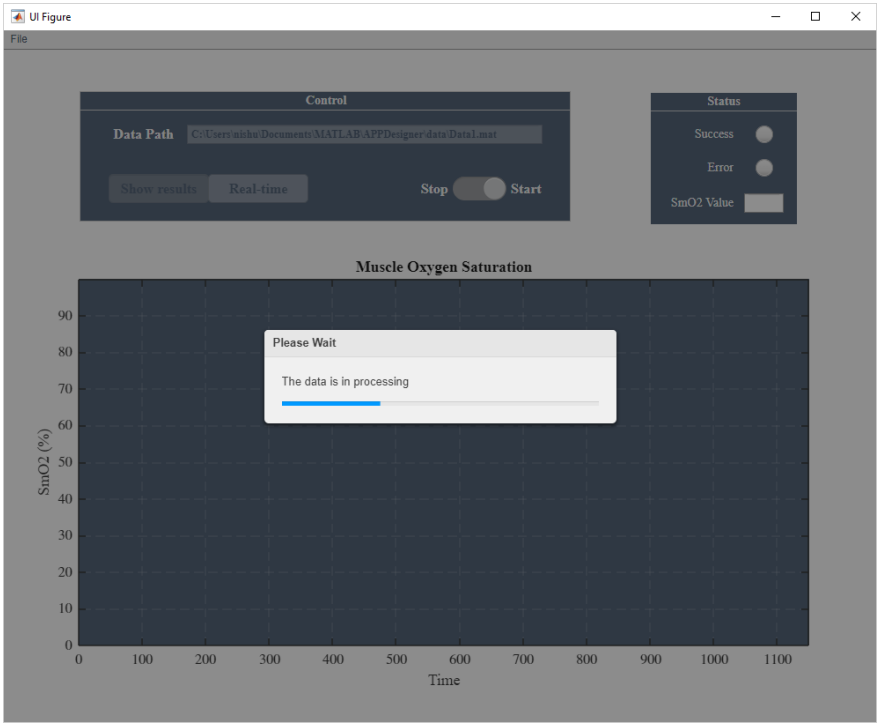

Figure 38: Calculation progress reminder

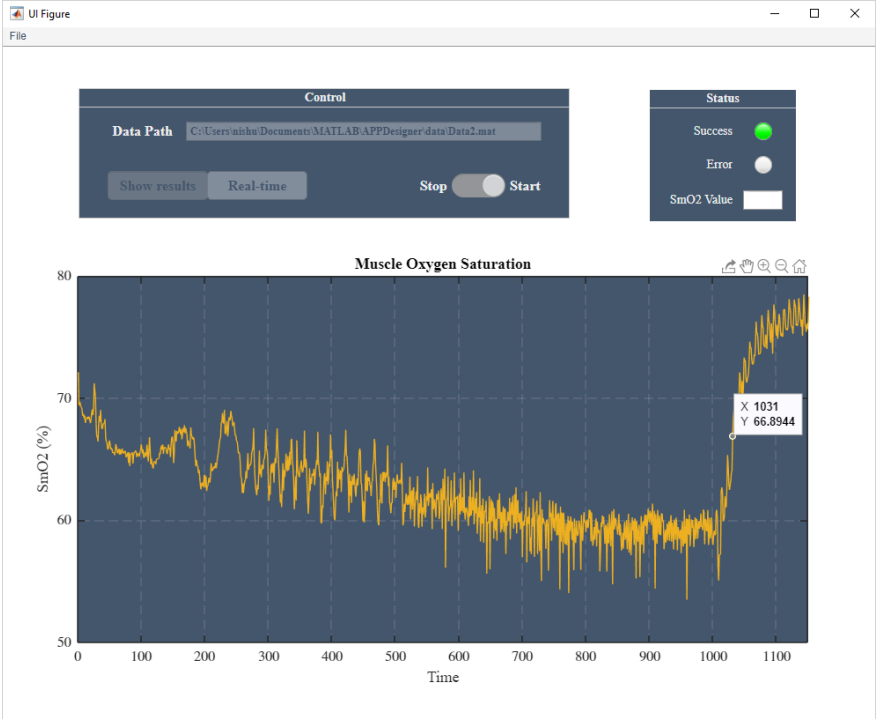

Figure 39: Display calculation and classification results with reliable data

Figure 40: Display calculation and classification results with unreliable data

After the data processing was complete, the results of SmO_2 values of each second was displayed in the figure, as shown in Fig. 39. If the user moves the mouse to a certain position of the curve, the specific value will be displayed in the box, where X represents the time in second, Y represents the SmO_2 value at that specific time. The success light changed to green represented that this data was classified as reliable so that the results shown were informative.

If the input data was classified as unreliable, the error light would change to red to indicate that the results shown were useless, as shown in Fig. 40.

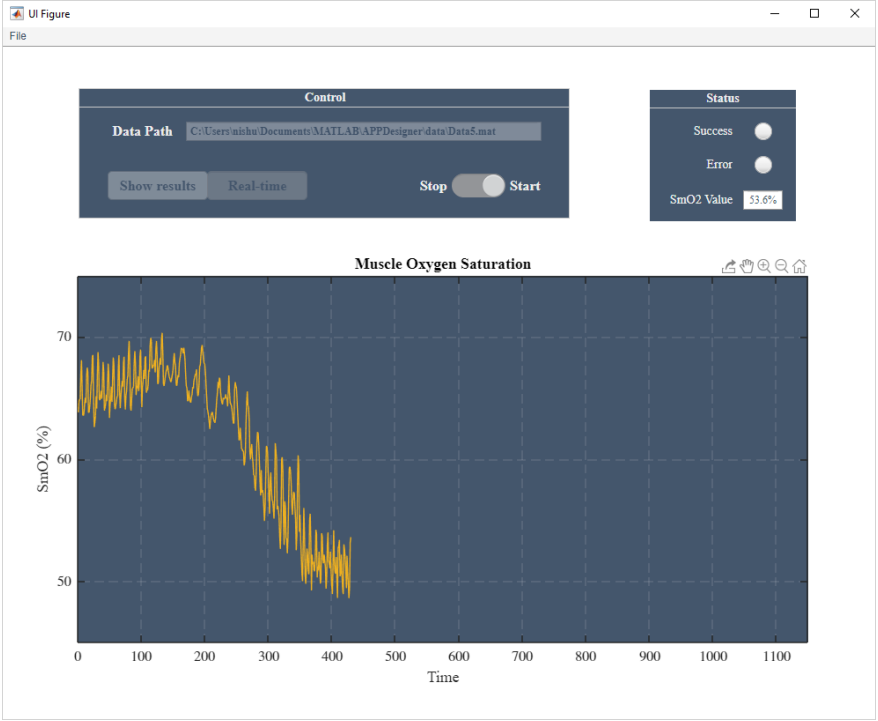

Figure 41: Real-time calculation with display SmO_2 value and curve

Besides the functionality of showing SmO_2 results, this application also provide a simulation to real-time testing. All of the user interaction procedures were same except for clicking the teal-time button before clicking start. Fig. 41 shows the simulation was in progress and the results were showed in ”real-time”. However, this was not a true real-time measurement, and this simulation just provided the possibility for real-time measurement. If the device can transmit data to the computer in real-time via some wireless method, such as Bluetooth and WiFi, the real-time measurement will be achieved.

Chapter 5

Conclusion and Future Work

5.1 Conclusion

Measuring muscle oxygen saturation quantitatively and accurately provides benefits for sports enthusiasts and athletes. They can monitor the training of a specific muscle in their body. In this thesis, an algorithm was introduced for a newly invented SmO_2 measurement device. The light attenuation of each wavelength at two source-detector distances was generated from the original measured hexadecimal data. To reduce the effect of the absorption and scattering of overlying tissues, such as skin and fat, an orthogonalization technique was introduced to generate the orthogonal attenuation from the light attenuation of two source-detector distances. The Taylor series expansion model of SmO_2 was fitted to the orthogonal attenuation using bound-constrained non-linear least squares fitting. The boundaries of parameters in bound-constrained non-linear least squares fitting was chosen with their physical meanings. Then, the SmO_2 values of each sampling were calculated by the ratio of the concentration of oxygenated hemoglobin to the concentration of total hemoglobin.

In our study, two training procedure was designed to *in vivo* measurement. In total, 33 independent tests of different subjects of two training procedures were done. The measuring results were plot in figure and compared with the results of Moxy monitor. We analyzed the absolute values of each training status and the trends of two training procedures, which were all within a reasonable range.

However, due to the instability of the wearable device, some of the measuring results were

unreliable. A fault diagnostic was needed to remind users to wear the device properly and training as the designer procedures. It was done by classifying the reliability of orthogonal attenuation in a period using machine learning approach. We labelled the data that collected from 21 tests with its reliability and split them into different training status. In each training status, support vector machines with Gaussian radial basis function kernel was trained. The parameters were determined by the method of grid search. Two evaluation curves, ROC curve and cross-validation learning curve, were used to evaluate the performance of classifiers. After evaluation, the SVM classifiers in both training states can achieve an accuracy of over 97%.

For the convenience of users, an application that integrated the SmO_2 calculation and fault diagnostic was developed in Matlap App Designer. With this application, users can generate the SmO_2 results with three clicks, including choosing the data file from file explore, choosing the resulting showing mode or real-time mode, and clicking start. The SmO_2 curve during training and the absolute values could be displayed in the interface. And two indication lights would show whether the data is reliable or not. However, the real-time mode in this application was just a simulation of real-time measurement. A wireless transmission module should be integrated in the device so that the data could be received and processed in computer in real-time.

5.2 Future Work

Although the quantitative measurement of SmO_2 and fault diagnostic were studied in this thesis, there are still some limitations that need to be addressed in future. In the following, some of the potential directions for future research work are provided.

5.2.1 Improve the Estimation Accuracy and Reliability in Practical

As mentioned in the previous chapters, the reliability was highly dependent on the correct wearing of our device. In addition, measurement temperature and humidity of human skin would also affect the accuracy. Fault diagnostic can only give the trainer a hint that the measurement results are unreliable, but it cannot give the reliable and accurate results. Therefore, how to estimate reliable results under improper wearing and under different temperature and humidity conditions is a question worth studying in the future.

Besides, the fault diagnostic in this thesis was based on the data labelled by comparing with Moxy monitor. In actual use, the real class of data is unknown. To make the fault diagnosis function to be available in practical, there are two possible solutions. The first method is to use unsupervised learning to predict the reliability of data. Another one is to establish a complete rule for judging the reliability of data, which can be combined with data from other hardware devices, such as thermometers, hygrometers, and gyroscopes.

5.2.2 Personalized Parameters and Fault Diagnostic

In this thesis, the *in vivo* measurements were done in 33 different individuals and their physical parameters, such as body fat percentage and skin color, were unknown. However, for individuals with different fat thickness and skin color, the best boundaries and initial values of least squares fitting and parameters of the classification model will be different. What we studied in this thesis was only the parameters and models for ordinary people. In other words, we design general algorithms for all users of this device. However, as a personal wearable measuring device, it should be adapted to each wearer's own physical parameters. In order to enable this device to customize personalized parameters and models for each user, differences in parameters for different individuals should be studied in the future.

In the case of knowing the individual's physical parameters, for example, the same person can use the device to measure multiple times to obtain data in the duture study. The data obtained in this way can be analyzed for intra-personal characteristics. Then, let multiple people participate in the experiment to analyze the inter-personal differences. By comparing the data of people with different body fat and skin color, it is possible to propose algorithms personalized to different individuals.

5.2.3 *In Vivo* Measurement and Fault Diagnostic for Other Exercises and Other Muscles

The *in vivo* measurement did in this thesis were based on running and walking, and the measuring muscle was calf muscles. A monitoring device should not only target one exercise. Other training

should also be considered, such as swimming, rope jumping, and weightlifting. And more corresponding muscles should be measure, such as forearm, thigh muscles, biceps brachii, and triceps brachii. Therefore, more *in vivo* measurements should be done in different muscles with different exercises in the future study.

Besides, the data classification of reliability did in this study just gave a possibility of fault diagnostic. To improve the accuracy and universality of fault diagnostic for any exercise and any muscle, more *in vivo* measurement and analysis should be done in the future work.

5.2.4 Real-Time Measurement and Fault Diagnostic of SmO_2

Although a simulation of real-time testing has been described in previous chapter, the true real-time measurement requires more improvement both in hardware and software. The device should be able to transmit data to the computer or phone in real-time via some wireless methods, such as Bluetooth and WiFi. And the receiving computer or phone needs to have an interface to receive and read the real-time transmitted data. The calculation algorithms will not change for real-time measurement but the fault diagnostic based on machine should be different.

In the real-time prediction, a time factor can be added as a feature in machine learning. A possible method is to use 5 attenuation and time in each second as the feature so that the training data is in 6-dimension, which is much lower than the current 50-dimensional. In this way, not only can the dimensionality be reduced, but also all the training status can be learned in one model. Besides, the newly predicted values and results can be added into the training dataset in real time to improve the accuracy of the classifier.

5.2.5 Mobile Application Combined with Professional Training Advice

The application designed in Matlab App Designer was aimed to the professional users. For fitness enthusiasts and athletes, an application on mobile phone will be more convenient to use. So a mobile application is necessary to be developed in the future.

Besides the value of SmO_2, measurement of other metrics, such as heart rate, can also be integrated in this application. It is not enough to only show the values of these metrics because non-professional athletes don't know what these metrics indicate. Professional training advice based

on their training behavior and performance should also be provided in this application. These are things that need to be studied in the future.

Appendix A

Appendix

A.1 Taylor Series Expansion

The Taylor series of a function is the infinite sum of terms expressed as the derivatives of the function at a specific point. The partial sum formed by the n first terms of the Taylor series is a degree n polynomial, which is called the nth Taylor polynomial of the function. Generally, when n increases, the Taylor polynomial approximation becomes better.

The Taylor series of a real or complex function $f(x)$ that is infinitely differentiable at a real or complex number x_0 is defined as

$$\begin{aligned} f(x) &= \sum_{n=0}^{\infty} \frac{f^{(n)}(x_0)}{n!} (x - x_0)^{(n)} \\ &\approx f(x_0) + \frac{f'(x_0)}{1!}(x - x_0) + \frac{f''(x_0)}{2!}(x - x_0)^2 \frac{f'''(x_0)}{3!}(x - x_0)^3 + \cdots \end{aligned} \tag{88}$$

where $f^{(n)}(x_0)$ denotes the nth derivative of $f(x)$ evaluated at the point x_0.

A.2 Coefficient of Determination

In statistics, the coefficient of determination, denoted R^2, is the proportion of variance in the dependent variable, and the variance can be predicted from the independent variable.

Assuming that a data set has n values marked $\mathbf{y} = [y_1, \cdots, y_n]^T$, each associated with a modeled value marked $\mathbf{f} = [f_1, \cdots, f_n]^T$. Define the residuals as $e_i = y_i - f_i$ or $\mathbf{e} = \mathbf{y} - \mathbf{f}$.

Define $\bar{y}$ as the mean of the observed data:

$$\bar{y} = \frac{1}{n}\sum_{i=1}^{n} y_i \tag{89}$$

There are two sums of squares can be calculated, including total sum of squares in equation (90) and residuals sum of squares in equation (91).

$$SS_{tot} = \sum_i (y_i - \bar{y})^2 \tag{90}$$

$$SS_{res} = \sum_i (y_i - f_i)^2 - \sum_i e_i^2 \tag{91}$$

Therefore, the coefficient of determination can be defined as

$$R^2 = 1 - \frac{SS_{res}}{SS_{tot}} \tag{92}$$

If the modeled value exactly matches the observed value, resulting in $SS_{res} = 0$ and $R^2 = 1$, the modeling or fitting is the most successful. If the predicted value is always equal to the average value $\bar{y}$, it will result in $R^2 = 0$. In the worst case, a model with a poor prediction will make R^2 become negative.

Bibliography

[1] R. Schmitz, "Systems and methods for measuring oxygenation," U.S. Patent 8 941 830B2, Jan. 27, 2015.

[2] B. Huang, G. Zhang, and Z. Yu, "Near infrared unit for muscle oxygen measurement," China Patent 109 222 989A, Jan. 17, 2019.

[3] P. Bouguer, *Essai d'optique sur la gradation de la lumière (in French)*. Paris, France: Claude Jombert, 1729.

[4] A. Beer, "Bestimmung der absorption des rothen lichts in farbigen flüssigkeiten," *Annalen der Physik und Chemie (in German)*, vol. 86, no. 5, pp. 78–88, 1852.

[5] J. H. Lambert, *Photometria sive de mensura et gradibus luminis, colorum et umbrae (in Latin)*. Augsburg, Germany: Eberhardt Klett, 1760.

[6] Y. Yang, O. Soyemi, P. J. Scott, M. R. Landry, S. M. Lee, L. Stroud, and B. R. Soller, "Quantitative measurement of muscle oxygen saturation without influence from skin and fat using continuous-wave near infrared spectroscopy," *Optics express*, vol. 15, no. 21, pp. 13 715–13 730, 2007.

[7] D. T. Delpy, M. Cope, P. van der Zee, S. Arridge, S. Wray, and J. Wyatt, "Estimation of optical pathlength through tissue from direct time of flight measurement," *Physics in Medicine and Biology*, vol. 33, no. 12, pp. 1433—-1442, 1988.

[8] T. Jue and K. Masuda, *Application of Near Infrared Spectroscopy in Biomedicine*. Springer US, 2013.

[9] M. Ferrari, L. Mottola, and V. Quaresima, "Principles, techniques, and limitations of near infrared spectroscopy," *Canadian Journal of Applied Physiology*, vol. 29, no. 4, pp. 463–487, 2004.

[10] F. Scholkmann, S. Kleiser, A. J. Metz, R. Zimmermann, J. M. Pavia, U. Wolf, and M. Wolf, "A review on continuous wave functional near-infrared spectroscopy and imaging instrumentation and methodology," *Neuroimage*, vol. 85, no. 1, pp. 6–27, 2014.

[11] M. Perutz, "Hoppe-seyler, stokes and haemoglobin," *Biological chemistry Hoppe-Seyler*, vol. 376, no. 8, pp. 449–450, 1995.

[12] S. J. Matcher, C. Elwell, C. Cooper, M. Cope, and D. Delpy, "Performance comparison of several published tissue near-infrared spectroscopy algorithms," *Analytical biochemistry*, vol. 227, no. 1, pp. 54–68, 1995.

[13] G. M. Hale and M. R. Querry, "Optical constants of water in the 200-nm to 200-μm wavelength region," *Applied Optics*, vol. 12, no. 3, pp. 555–563, 1973.

[14] M. Lipcsey, N. C. Woinarski, and R. Bellomo, "Near infrared spectroscopy (nirs) of the thenar eminence in anesthesia and intensive care," *Annals of intensive care*, vol. 2, no. 11, 2012.

[15] L. Nicolai, "Uber sichtbarmachung, verlauf und chemische kinetic der, oxyhemoglobinreduktion im lebendum gewebe, besonders in der menschlichen haut," *Archiv Geschichte Physiology*, vol. 229, pp. 372—-384, 1932.

[16] G. A. Millikan, "The oximeter, an instrument for measuring continuously the oxygen saturation of arterial blood in man," *Review of Scientific Instruments*, vol. 13, no. 10, pp. 434–444, 1942.

[17] E. H. Wood and J. E. Geraci, "Photoelectric determination of arterial oxygen saturation in man," *The Journal of laboratory and clinical medicine*, vol. 34, no. 3, pp. 387—-401, 1949.

[18] T. Aoyagi, M. Kishi, K. Yamaguchi, and S. Watanabe, "Improvement of an earpiece oximeter," *13th Annual Meeting of the Japan Society of Medical Electronics and*

Biological Engineering, Osaka, Japan, vol. 12, pp. 90–91, 1974. [Online]. Available: https://ci.nii.ac.jp/naid/10014590155/en/

[19] A. Duncan, J. H. Meek, M. Clemence, C. E. Elwell, L. Tyszczuk, M. Cope, and D. T. Delpy, "Optical pathlength measurements on adult head, calf and forearm and the head of the newborn infant using phase resolved optical spectroscopy," *Physics in medicine and biology*, vol. 40, no. 2, pp. 295–304, 1995.

[20] S. Suzuki, S. Takasaki, T. Ozaki, and Y. Kobayashi, "Tissue oxygenation monitor using NIR spatially resolved spectroscopy," in *Optical Tomography and Spectroscopy of Tissue III*, B. Chance, R. R. Alfano, and B. J. Tromberg, Eds., vol. 3597, International Society for Optics and Photonics. SPIE, 1999, pp. 582 – 592. [Online]. Available: https://doi.org/10.1117/12.356862

[21] A. Messere and S. Roatta, "Influence of cutaneous and muscular circulation on spatially resolved versus standard beer-lambert near-infrared spectroscopy," *Physiological Reports*, vol. 1, no. 7, 2013.

[22] A. Pellicer and M. del Carmen Bravo, "Near-infrared spectroscopy: A methodology-focused review," *Seminars in fetal and neonatal medicine*, vol. 16, no. 1, pp. 42–49, 2011.

[23] F. P. Bolin, L. E. Preuss, R. C. Taylor, , and R. J. Ference, "Refractive index of some mammalian tissues using a fiber optic cladding method," *Applied Optics*, vol. 28, no. 12, pp. 2297–2303, 1989.

[24] M. Wolf, M. Ferrari, and V. Quaresima, "Progress of near-infrared spectroscopy and topography for brain and muscle clinical applications," *Journal of Biomedical Optics*, vol. 12, no. 6, p. 062104, 2007.

[25] B. Chance, R. Hulsizer, E. J. MacNichol, and F. Williams, *Electronic Time Measurements*. MIT Radiation Laboratories Series, 1949.

[26] W. G. Hopkins, "Measurement of training in competitive sports," *Sportscience*, vol. 2, no. 4, 1998.

[27] K. D. McClatchey, *Clinical Laboratory Medicine*. Philadelphia: Lippincott Williams and Wilkins, 2002.

[28] R. Boushel, H. Langberg, J. Olesen, J. Gonzales-Alonzo, J. . Bülow, and M. Kjær, "Monitoring tissue oxygen availability with near infrared spectroscopy (nirs) in health and disease," *Scandinavian journal of medicine & science in sports*, vol. 11, no. 4, pp. 213–222, 2001.

[29] G. Hüfner, "Neue versuche zur bestimmung der sauerstoffcapacität des blutfarbstoffs," *Archiv für pathologische Anatomie und Physiologie und für klinische Medicin*, vol. 55, pp. 130–176, 1894.

[30] K. Matthes and F. Gross, "Fortlaufende registrierung der lichtabsorption des blutes in zwei verschiedenen spektralbezirken," *Naunyn-Schmiedebergs Archiv für experimentelle Pathologie und Pharmakologie*, vol. 191, pp. 381–390, 1938.

[31] ——, "Untersuchung über die absorption von rotem und ultrarotem licht durch kohlenoxygesättigstes, sauerstoffgesättigtes und reduziertes blut," *Naunyn-Schmiedebergs Archiv für experimentelle Pathologie und Pharmakologie*, vol. 191, pp. 369–380, 1938.

[32] ——, "Zur methode der fortlaufenden registrierung der farbe des menschlichen blutes," *Naunyn-Schmiedebergs Archiv für experimentelle Pathologie und Pharmakologie*, vol. 191, pp. 523–528, 1938.

[33] F. F. Jöbsis, "Noninvasive, infrared monitoring of cerebral and myocardial oxygen sufficiency and circulatory parameters," *Science*, vol. 198, pp. 1264—-1267, 1977.

[34] D. E. Myers, L. D. Anderson, R. P. Seifert, J. P. Ortner, C. E. Cooper, G. J. Beilman, and J. D. Mowlem, "Noninvasive method for measuring local hemoglobin oxygen saturation in tissue using wide gap second derivative near-infrared spectroscopy," *Journal of biomedical optics*, vol. 10, no. 3, p. 034017, 2005.

[35] A. A. Stratonnikov and V. B. Loschenov, "Evaluation of blood oxygen saturation in vivo from diffuse reflectance spectra," *Journal of biomedical optics*, vol. 6, no. 4, pp. 457–467, 2001.

[36] Y. Yang, M. R. Landry, O. O. Soyemi, M. A. Shear, D. S. Anunciacion, and B. R. Soller, "Simultaneous correction of the influence of skin color and fat on tissue spectroscopy by use of a two-distance fiber-optic probe and orthogonalization technique," *Optics Letters*, vol. 30, no. 17, pp. 2269–2271, 2005.

[37] Y. Yamashita, A. Maki, and H. Koizumi, "Wavelength dependence of the precision of noninvasive optical measurement of oxy-, deoxy-, and total-hemoglobin concentrations," *Medical physics*, vol. 28, no. 6, pp. 1108–1114, 2001.

[38] A. Corlu, T. Durduran, R. Choe, M. Schweiger, E. M. C. Hillman, S. R. Arridge, and A. G. Yodh, "Uniqueness and wavelength optimization in continuous-wave multispectral diffuse optical tomography," *Optics letters*, vol. 28, no. 23, pp. 2339–2341, 2003.

[39] A. Corlu, T. D. Regine Choe, K. Lee, M. Schweiger, S. R. Arridge, E. M. C. Hillman, and A. G. Yodh, "Diffuse optical tomography with spectral constraints and wavelength optimization," *Optics letters*, vol. 44, no. 11, pp. 2082–2093, 2005.

[40] T. Zhu, S. Faulkner, T. Madaan, A. Bainbridge, D. Price, D. Thomas, E. Cady, N. Robertson, X. Golay, and I. Tachtsidis, "Optimal wavelength combinations for resolving in-vivo changes of haemoglobin and cytochrome-c-oxidase concentrations with nirs," in *Biomedical Optics and 3-D Imaging*. Optical Society of America, 2012, p. JM3A.6.

[41] E. M. Sevick, B. Chance, J. Leigh, S. Nioka, and M. Maris, "Quantitation of time- and frequency-resolved optical spectra for the determination of tissue oxygenation," *Analytical biochemistry*, vol. 195, no. 2, pp. 330–351, 1991.

[42] A. Hielscher, F. Tittel, and S. Jacques, "Noninvasive monitoring of blood oxygenation by phase-resolved transmission spectroscopy," in *Proceedings of SPIE - The International Society for Optical Engineering*, B. Chance and R. Alfano, Eds. Society of Photo-Optical Instrumentation Engineers, 1993, pp. 275–288, copyright: Copyright 2003 Elsevier Science B.V., Amsterdam. All rights reserved.

[43] M. S. Patterson, B. Chance, , and B. C. Wilson, "Time resolved reflectance and transmittance for the noninvasive measurement of tissue optical properties," *Applied Optics*, vol. 28, no. 12, pp. 2331–2336, 1989.

[44] A. Kienle and M. S. Patterson, "Improved solutions of the steady-state and the time-resolved diffusion equations for reflectance from a semi-infinite turbid medium," *Journal of the Optical Society of America A*, vol. 14, no. 1, pp. 246–254, 1997.

[45] R. A. D. Blasi, M. Ferrari, A. Natali, G. Conti, A. Mega, and A. Gasparetto, "Noninvasive measurement of forearm blood flow and oxygen consumption by near-infrared spectroscopy," *Journal of applied physiology*, vol. 76, no. 3, pp. 1388—-1393, 1994.

[46] P. Farzam, Z. Starkweather, and M. A. Franceschini, "Validation of a novel wearable, wireless technology to estimate oxygen levels and lactate threshold power in the exercising muscle," *Physiological reports*, vol. 6, no. 7, p. e13664, 2018.

[47] N. R. Borges and M. W. Driller, "Wearable lactate threshold predicting device is valid and reliable in runners," *Journal of strength and conditioning research*, vol. 30, no. 8, p. 2212–2218, 2016.

[48] W. N. Colier, I. B. Meeuwsen, H. Degens, and B. Oeseburg, "Determination of oxygen consumption in muscle during exercise using near infrared spectroscopy," *Acta anaesthesiologica Scandinavica. Supplementum*, vol. 107, pp. 151—-155, 1995.

[49] M. C. P. van Beekvelt, B. G. M. van Engelen, R. A. Wevers, and W. N. J. M. Colier, "In vivo quantitative near-infrared spectroscopy in skeletal muscle during incremental isometric handgrip exercise," *Clinical physiology and functional imaging*, vol. 22, no. 3, pp. 210—-217, 2002.

[50] L. G. Gutwein, C. D. Bahler, and A. S. Kaleth, "Method and apparatus for assessing tissue oxygenation saturation," U.S. Patent 20 170 273 609A1, Sep. 28, 2017.

[51] M. A. Franceschini, D. A. Boas, A. Zourabian, S. N. Solomon G Diamond, D. W. Lin, J. B. Moore, and S. Fantini, "Near-infrared spiroximetry: noninvasive measurements of venous

saturation in piglets and human subjects," *Journal of applied physiology*, vol. 92, no. 1, pp. 372—-384, 2002.

[52] M. Oda, Y. Yamashita, T. Nakano, A. Suzuki, K. Shimizu, I. Hirano, F. Shimomura, E. Ohmae, T. Suzuki, and Y. Tsuchiya, "Near-infrared time-resolved spectroscopy system for tissue oxygenation monitor," in *Optical Tomography and Spectroscopy of Tissue III*, B. Chance, R. R. Alfano, and B. J. Tromberg, Eds., vol. 3597, International Society for Optics and Photonics. SPIE, 1999, pp. 611 – 617. [Online]. Available: https://doi.org/10.1117/12.356809

[53] S. J. Matcher, M. Cope, and D. T. Delpy, "Use of the water absorption spectrum to quantify tissue chromophore concentration changes in near-infrared spectroscopy," *Physics in Medicine & Biology*, vol. 39, no. 1, pp. 177–196, 1994.

[54] B. J. Lutjemeier, L. F. Ferreira, D. C. Poole, D. Townsend, and T. J. Barstow, "Muscle microvascular hemoglobin concentration and oxygenation within the contraction–relaxation cycle," *Respiratory Physiology & Neurobiology*, vol. 160, no. 2, pp. 131–138, 2008.

[55] S. J. Matcher, M. Cope, and D. T. Delpy, "In vivo measurements of the wavelength dependence of tissue-scattering coefficients between 760 and 900 nm measured with time-resolved spectroscopy," *Applied Optics*, vol. 36, no. 1, pp. 386–396, 1997.

[56] C. F. Gauss, *Theoria Motus Corporum Coelestium in Sectionibus Conicis Solem Ambientium*. Cambridge University Press, 1809.

[57] K. Levenberg, "A method for the solution of certain non-linear problems in least squares," *Quarterly of Applied Mathematics*, vol. 2, pp. 164–168, 1944.

[58] C. Lawson and R. Hanson, *Solving Least Squares Problems*. Prentice–Hall, 1974.

[59] M. Box, D. Davies, and W. Swann, *Non-linear Optimization Techniques*. Oliver and Boyd for Imperial Chemical Industries, 1969.

[60] T. F. Coleman and Y. Li, "An interior trust region approach for nonlinear minimization subject to bounds," *Society for Industrial and Applied Mathematics*, vol. 6, no. 2, pp. 418–445, 1996.

[61] S. R. Arridge, M. Cope, and D. T. Delpy, "The theoretical basis for the determination of optical pathlengths in tissue: temporal and frequency analysis," *Physics in Medicine & Biology*, vol. 37, no. 7, pp. 1531–1560, 1992.

[62] W. Cui, C. Kumar, and B. Chance, "Experimental study of migration depth for the photons measured at sample surface," in *Time-Resolved Spectroscopy and Imaging of Tissues*, B. Chance, Ed., vol. 1431, International Society for Optics and Photonics. SPIE, 1991, pp. 180 – 191. [Online]. Available: https://doi.org/10.1117/12.44189

[63] T. Fearn, "On orthogonal signal correction," *Chemometrics and Intelligent Laboratory Systems*, vol. 50, no. 1, pp. 47–52, 2000.

[64] C. A. Andersson, "Direct orthogonalization," *Chemometrics and Intelligent Laboratory Systems*, vol. 47, no. 1, pp. 51–63, 1999.

[65] S. Wolda, H. Anttia, F. Lindgrenb, and J. Ohmanc, "Orthogonal signal correction of near-infrared spectra," *Chemometrics and Intelligent Laboratory Systems*, vol. 44, no. 1, pp. 175–185, 1998.

[66] T. Hamaoka, T. Katsumura, N. Murase, S. Nishio, T. Osada, T. Sako, H. Higuchi, Y. Kurosawa, T. Shimomitsu, M. Miwa, and B. Chance, "Quantification of ischemic muscle deoxygenation by near infrared time-resolved spectroscopy," *Journal of biomedical optics*, vol. 5, no. 1, pp. 102–105, 2000.

[67] B. S. Everitt, S. Landau, M. Leese, and D. Stahl, *Miscellaneous Clustering Methods*. Chichester, UK: John Wiley & Sons, Ltd., 2001. [Online]. Available: https://doi.org/10.1002/9780470977811.ch8

[68] C. Cortes and V. Vapnik, "Support-vector networks," *Machine Learning*, vol. 20, pp. 273–297, 1995.

[69] B. E. Boser, I. M. Guyon, and V. N. Vapnik, "A training algorithm for optimal margin classifiers," in *Proceedings of the Fifth Annual Workshop on Computational Learning Theory*, ser. COLT '92. New York, NY, USA: Association for Computing Machinery, 1992, p. 144–152. [Online]. Available: https://doi.org/10.1145/130385.130401

[70] L. Buitinck, G. Louppe, M. Blondel, F. Pedregosa, A. Mueller, O. Grisel, V. Niculae, P. Prettenhofer, A. Gramfort, J. Grobler, R. Layton, J. VanderPlas, A. Joly, B. Holt, and G. Varoquaux, "API design for machine learning software: experiences from the scikit-learn project," in *ECML PKDD Workshop: Languages for Data Mining and Machine Learning*, 2013, pp. 108–122.